PHOTONIC CRYSTALS BASED ON SILICA MICROSPHERES

(Cristales fotónicos basados en microesferas de sílice)

Memoria presentada para optar al grado de Doctor en Ciencias por:

Florencio García Santamaría

Tesis dirigida por:

Dr. Ceferino López Fernández
Prof. Francisco Meseguer Rico

Tutor:
Prof. Luis Viña Liste

Departamento de Física de Materiales
Facultad de Ciencias
Universidad Autónoma de Madrid

Instituto de Ciencia de Materiales de Madrid
Consejo Superior de Investigaciones Científicas

Octubre de 2003

A mi familia:
por aguantarme...

Agradecimientos

Directa o indirectamente, son muchas las personas que me han ayudado a que la escritura de esta tesis fuese posible. De entre todas ellas, quienes sin duda merecen figurar en primer lugar son mis directores de tesis y sin embargo siempre buenos consejeros. Al Dr. Cefe López con quien he trabajado más estrechamente le agradezco toda la confianza depositada en mi, sus pacientes correcciones y por querer siempre algo más y mejor a lo anterior. Al Prof. Francisco Meseguer le agradezco su torbellino de sueños e ideas que contagia incluso a los más realistas. Gracias también al Prof. Luis Viña, mi tutor en la Universidad Autónoma de Madrid.

Agradezco a la Comunidad de Madrid la beca de Formación de Personal Investigador (FPI) de la que he disfrutado desde 2000 y al Instituto de Ciencia de Materiales de Madrid por haber permitido que me formase en este centro durante los primeros años de mi vida científica.

Agradecimientos específicos por capítulo:

- Capítulo II: Agradezco a Puerto Morales su ayuda en las medidas de movilidad. El estudio de porosimetría fue llevado a cabo en el Instituto de Catálisis del CSIC.
- Capítulo III: El experimento de cristalización de coloides en suspensión ha sido llevado a cabo con el apoyo de Beatriz Hernández. El trabajo de electroforesis fue desarrollado con la colaboración de Miguel Holgado.
- Capítulo IV: El autor agradece profundamente a la Dra. Verónica Salgueiriño y al Prof. Luis Liz-Marzán, la síntesis de esferas con núcleos metálicos y las muy enriquecedoras conversaciones mantenidas.
- Capítulo V: Este trabajo fue desarrollado parcialmente en el Centro Tecnológico de Ondas en la Universidad Politécnica de Valencia. La construcción y mantenimiento de la línea de CVD por Marta Ibisate y la síntesis de esferas de Isabelle Rodríguez fueron fundamentales.
- Capítulo VI: Los sustratos y plantillas fueron desarrollados en dos centros: Instituto de Microelectrónica de Madrid (CSIC) por J. Anguita y Agere Systems España por A. Urquía y M. Belmonte. La micromanipulación fue llevada a cabo en el National Institute of Materials Science en Japón en colaboración con el Dr. H. Miyazaki.

Salvo en los experimentos de cristalización de coloides en suspensión y en el capítulo V, las esferas de sílice fueron sintetizadas por Marta Ibisate.

Son mis compañeros de despacho los que han hecho que los momentos menos agradables lo fuesen más y que estos años de doctorado estén plagados de felices anécdotas. Alvaro Blanco, con quien he compartido despacho durante más tiempo y de quien he escuchado los mejores (y peores) chistes. Beatriz Hernández, mi amiga desde la primera a la última letra; no puedo imaginar mejor compañía.

Mercedes Vila, quien llena todo de alegría (y música), gracias por convertir el despacho en un lugar al que se desea ir. Elisa Palacios, una chica inteligente a la par que elegante, a ella le debemos el premio a la mejor portada de *Advanced Materials* 2002. Juan Galisteo, gracias al cual he aprendido que el mundo de los teóricos no es para tanto… Antonio Bernabé, cuyo final de tesis coincidió con el principio de la mía, un ejemplo de "hermano mayor". Toño, un gallego en el exilio. Y Elizabeth Castillo, breve pero intensa.

A Marta Ibisate, también compañera de despacho durante un tiempo, nuestra conexión Valenciana y un ejemplo de alegría en el trabajo y de paciencia, mucha paciencia… Ángel Muñoz, una persona a la que no puedo dejar de admirar, a pesar de haberlo visto a diario me cuesta entender que haya alguien con tantos conocimientos, curiosidad, amabilidad, modestia y alegría. Ricardo Arias, un manchego con multitud de interesantes citas de Herodoto, Cervantes… Nieves, a la que no se le escapa una. Joaquín Requena, siempre dispuesto a ayudar. Lola Golmayo, un fichaje lleno de sorpresas. José A. Gago, una nota de arte en la vida del científico. Al resto de compañeros del Instituto de Ciencia de Materiales: Mauricio, Sonsoles, Laura, Diana, Tere, Félix, Isabel…

Al grupo de Valencia, empezando por Hernán Míguez cuyos trabajos y conversaciones han sido inspiración y ejemplo para mí. A Roberto, Isabelle y Silvia que siempre han hecho de mis estancias en tierras valencianas un placer y mi trabajo infinitamente más cómodo. Y a la no-fotónica pero muy especial Laura Santos.

Gracias a nuestros queridos teóricos liderados por el Prof. J. Sánchez-Dehesa, siempre dispuesto a ayudar y a pasarlo bien donde haga falta y a F. López-Tejeira por su lucha contra los malvados parámetros cabalísticos que acechan tras oscuros programas.

Miguel Holgado, no sé en que grupo catalogarte, pero contigo compartí mi primer trabajo experimental y la primera publicación. Ojalá encuentre gente con la que me sea tan fácil trabajar como lo fue contigo. Adelaida Cintas, de la que siempre tendré el recuerdo que se merece. Con ella aprendí nuevos significados de la palabra compartir y de las cosas tan increíbles que se pueden hacer con un simple polímetro.

Dr. H. Miyazaki, thank you very much for hosting me, firstly in Tokio and then in Tsukuba. My stay in Japan is a period of time which is among my most exciting experiences. Thank you for your patience while teaching me how to use your nanorobot and answering my many questions about Japanese cooking. I will always be indebted to you. I am also thankful to Prof. N. Shinya. Gracias a Alberto Baruj quien hizo que mi estancia en Japón no fuese solitaria. Deseo que encuentres tu anhelado hueco para trabajar en y por tu querida Argentina.

Siempre estaré agradecido al Prof. L. Liz-Marzán de la universidade de Vigo por la oportunidad de colaborar con su grupo y publicar juntos algunos trabajos.

Además de la gente directamente relacionada con mi trabajo no puedo menos que expresar mi agradecimiento a aquellos que me han rodeado durante todos estos

años. Especialmente a mi familia, a quienes dedico esta tesis, que han sabido apoyarme en mis idas y venidas. A mi amiga Raquel le debo mucho más que esta tesis y no hay papel suficiente en el mundo para escribir y explicar todo lo que le habría de agradecer. Sinceramente, gracias por ser mi amiga. A Irma y Guillermo (cirujano y maestro Jedi), amigos incondicionales y seres humanos extraordinarios (por lo bueno y por lo inexplicable). Sara y Pablo (no menos maestro Jedi), vosotros ponéis la realidad en su sitio cuando nos juntamos los cinco.

Madrid, 29 de septiembre de 2003

Florencio García Santamaría

---GENERAL INDEX---

- ¿Lo hacemos ahora en inglés?
- Hmmm… ¡vale!
- Yo lo digo por el mercado internacional…

Anuncio televisivo de la ONCE.
Verano 2003

.

Chapter 1: Introduction to Photonic Crystals.

1.1 Photonic Crystals.

1.1.1 The concept.

A photonic crystal is a material in which the refractive index (RI) is periodically modulated on a length scale comparable to the desired operation wavelength. It is said to be a "crystal" because it is formed by a periodic arrangement of basic building blocks. The term "photonic" is added since photonic crystals are designed to affect the propagation properties of photons.

In general, the wave propagation is importantly affected when it enters into a material where some feature that concerns this wave is modulated. The wave scatters coherently at the interfaces between different featured regions. In the case of photons this feature is RI. For other systems propagating as waves, such as sound or electrons within a semiconductor, these features are the Young's module and the electric potential respectively.

The behavior of a photon with a certain frequency will depend on the propagation direction within the photonic crystals. The modulation of the RI will cause that certain energies and directions are forbidden for photons. A region of energies where the photonic crystal does not allow photons to propagate regardless of their direction and polarization is called a complete photonic band gap (cPBG).

1.1.2 Important crystal features and parameters.

In order to design a photonic crystal with a cPBG or a specific band behavior there are some crystal features and parameters that must be engineered.

- Dimensionality. The periodicity of the refractive index will determine the dimensionality of the photonic crystal. We may have one (1D), two (2D) or three (3D) dimensional lattices. Stacks of planes, sets of columns and any of the Bravais lattices are examples of each of those structures (see **Fig. 1.1 a-d**).
- Symmetry. The position of the building blocks of our photonic crystal will set the symmetry of our lattice. Examples of several three-dimensional symmetries can be found in Bravais lattices: simple cubic (sc), simple hexagonal (sh), body centered cubic (bcc) and face centered cubic (fcc). Other important lattices are formed from Bravais lattices with additional atoms within them. Typical examples are the hexagonal close-packed (hcp) and diamond structures (**Fig. 1.1** shows a graphical example of each of these lattices).
- Topology. A lattice with a given symmetry may present variations in its topology that will importantly affect the photonic band structure. The topology can be varied by interpenetrating the building blocks (network topology) or isolating them (Cermet topology). **Fig. 1.2** shows examples of different topologies for an fcc lattice.

- Lattice parameter. This is a fundamental distance which is used to characterize the separation between scattering building blocks. In the case of cubic lattices it is usually taken as the side of the cube. The range of wavelengths of the optical spectrum where our photonic crystal works will be proportional to the lattice parameter (*a*).

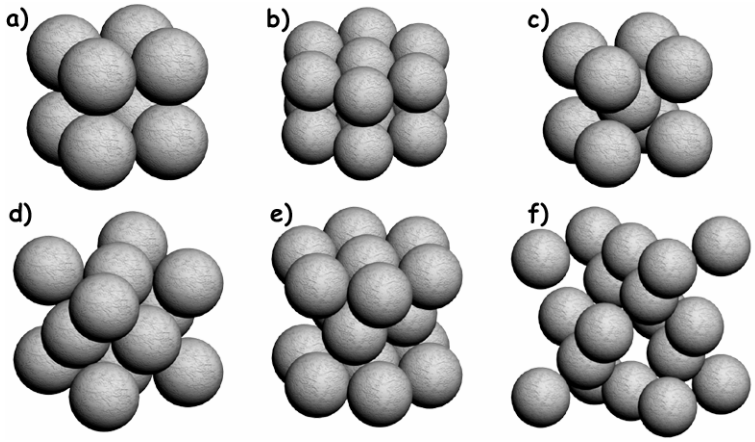

Fig. 1.1: Computer rendering showing different kinds of symmetries. a) simple cubic, b) simple hexagonal, c) body centered cubic, d) face centered cubic, e) hexagonal close packed and f) diamond lattice.

- Filling fraction and effective refractive index. The relative amount of material composing the scattering building block is called filling fraction (*ff*). The effective refractive index (n_{eff}) is usually calculated as the square root of the average dielectric constant (e_{av}). As happens with the lattice parameter, the range of wavelengths of the optical spectrum where our photonic crystal works will also depend on n_{eff}.
- Refractive index contrast (*d*). This value offers a general idea of the scattering strength of a two components crystal. This parameter is defined as the ratio between the RI of the high dielectric constant material (n_h) and the low dielectric constant material (n_l). $d=n_h/n_l$.
- Scalability. One of the most appealing characteristics is that there are no fundamental length scales or dielectric constant values implicit in equations. As a consequence, the results extracted from theory are completely scalable. The solution of the problem at one length scale determines the solutions at all other length scales. The region of the spectrum where the photonic crystal optical properties are to be observed will depend only on the RI of the crystal components and their filling fraction and will be directly proportional to the lattice parameter. Therefore, frequency (*w*) is usually normalized by the lattice parameter since if we keep the rest of the features unchanged, the quantity *wa* will remain invariable. This means that if the lattice parameter is doubled, the mode frequency will be divided by two.

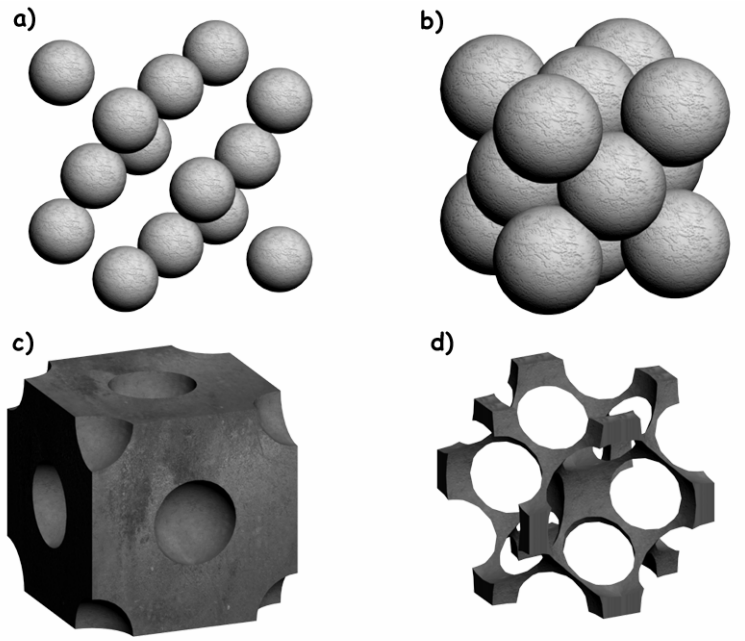

Fig. 1.2: A lattice with the same symmetry (fcc in this case) may present different topologies. a) isolated dielectric spheres in air, b) interpenetrated dielectric spheres in air, c) isolated air spheres in a dielectric and d) interpenetrated air spheres in a dielectric.

1.1.3 Photonic band structure.

The photonic band structure gives us information about the propagation properties of electromagnetic (*em*) radiation within the photonic crystal. It is a representation in which the available energy states are plotted as a function of propagation direction.

In order to understand how the photonic band structure is constructed a 2D system will be studied and compared with the case of a homogeneous dielectric. Although samples presented in this thesis are 3D photonic crystals, a 2D system is easier to explain and the arguments that will be used are immediately applicable to the 3D case. However the polarization effects are more important in 2D systems. As the example presented in this and next sub-section has only a tutorial purpose, the optical response to different polarizations will be ignored. Calculations will be limited to the case of transverse electric polarization (TE modes, transverse to the periodic plane).

The relationship between the wave-vector and frequency (also known as dispersion relation) for free photons in vacuum is well known: $w=ck$, where c is the vacuum light velocity. If photons are propagating through a homogeneous and isotropic dielectric then $w=ck/n$, where n is the RI of the dielectric material. As can be seen, the frequency (and therefore photon energy) depends linearly on the ratio between wave-vector module and the material RI. With an isotropic material there are no directions with special properties and consequently only the norm of the

wave-vector is required to obtain the photons energy. But, what happens if the RI is modulated along some directions? Obviously the dispersion relation written above is not valid for this case and should be different for each propagation direction.

A 2D structure made of cylinders and forming a square lattice is shown in **Fig. 1.3**. The distance between cylinders is the lattice parameter *a*. Vectors a and b in this figure point in directions which present a different RI modulation. Therefore, the dispersion relation for each impinging angle should differ. Fortunately thanks to the symmetry of the lattice there are directions which are equivalent, as shown in **Fig. 1.3 b** for a and a**'**. When two directions are equivalent, the periodicity of the RI is the same and the dispersion relation is the same for both. It can be deduced then, that it is not necessary to represent all the possible.

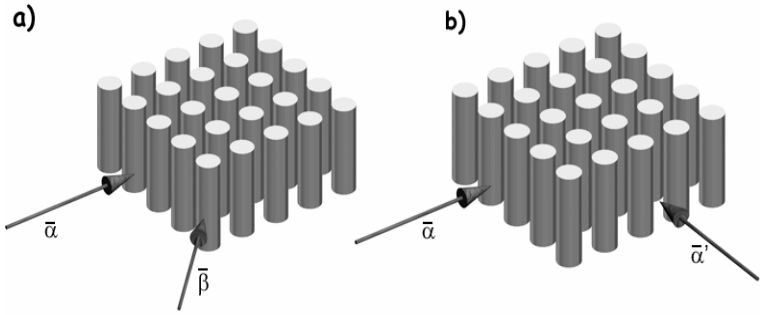

Fig. 1.3: 2D square lattice of cylinders. In a) two directions with a different modulation of the refractive index are pointed out. b) shows two directions in which the periodicity of the refractive index is equivalent.

The method to represent the dispersion relation is the same that is used in solid state physics[1,2] for the electron energy levels in a semiconductor. Bloch theory is used to demonstrate that any wave-vector in the reciprocal space (wave-vector space) can be translated to the first Brillouin zone (BZ) with a linear combination of reciprocal lattice primitive vectors. The result is a compact representation of the most important directions.

In our case the real space primitive vectors are $\mathbf{a_1}=a(1,0)$ and $\mathbf{a_2}=a(0,1)$. The primitive vectors of the reciprocal space are $\mathbf{b_1}=2\pi/a(1,0)$ and $\mathbf{b_2}=2\pi/a(0,1)$. They fulfill the condition $\mathbf{a_i}\cdot\mathbf{b_j}=2\pi\delta_{ij}$. Therefore the reciprocal lattice is a square lattice as well. The first BZ is the figure formed by the lines bisecting the segments joining one of the lattices points with its closest neighbors. In this BZ three high symmetry points are highlighted: Γ, X and M. These points constitute the vertices of the irreducible zone. Other points in this BZ can be obtained by applying symmetry operations (mirror reflection, inversion and rotation) on the irreducible zone. Any other point outside the first BZ can be translated to it by a translation operation with a linear combination of $\mathbf{b_1}$ and $\mathbf{b_2}$. The reciprocal lattice, primitive vectors and BZ is shown in **Fig. 1.4 a**.

In order to be able to compare the dispersion relation of a photonic crystal with a purely isotropic dielectric, the RI of the cylinders is set to such a value that *d* is

very close to unity. Therefore, we have is a system where dispersion relations must be very similar to the case of photons in a homogeneous dielectric.

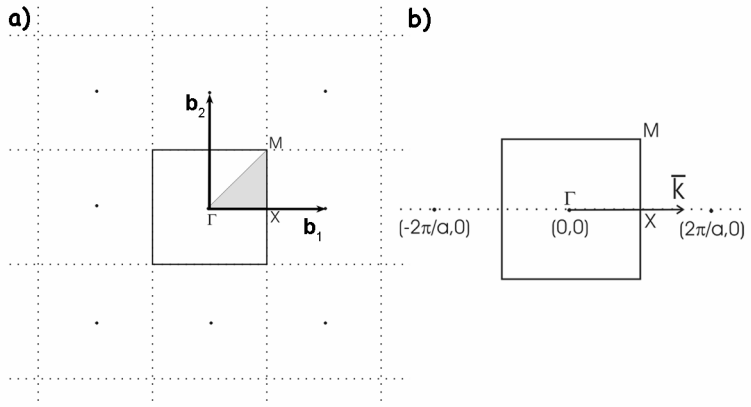

Fig. 1.4: a) shows the primitive vectors and some points of the reciprocal lattice for a 2D square lattice. The first Brillouin zone and most important symmetry points (Γ, X and M) are indicated as well. b) An arbitrary wave-vector **k** propagates in the ΓX direction.

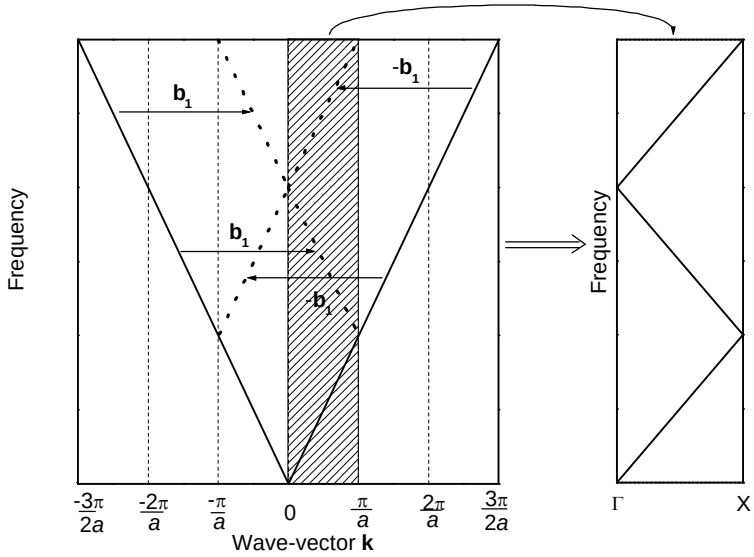

Fig. 1.5: A photon propagates parallel to ΓX, the dispersion relation is folded by applying translations which are linear combinations of the reciprocal lattice primitive vectors. The reduced-zone scheme representation for the dispersion relation is shown in the graph to the right. The frequency is in arbitrary units.

A photon that propagates with **k** contained in the ΓX direction, as shown in **Fig. 1.4 b**, would follow the behavior given by $w=ck/n$. Any of those wave-vectors not lying within the first BZ can be translated to it by a translation operation with a linear combination of the reciprocal lattice primitive vectors ($\mathbf{b_1}$ and $\mathbf{b_2}$). The dispersion relation can then be plotted from $-\pi/a$ to π/a, as shown in the left graph

of **Fig. 1.5** (dotted line). Since it is symmetric, the plot from -π/*a* to 0 is redundant and plotting from 0 to π/*a* gives all the necessary information. These are precisely two important coordinates named as Γ and X respectively (see **Fig. 1.4**). The final representation is shown in the graph to the right of **Fig. 1.5**. This kind of representation is called reduced-zone scheme.

However, the representation in **Fig. 1.5** is incomplete. As explained before, every other wave-vector **k** that lies on a point in the reciprocal lattice that can be translated to the ΓX segment should be represented as well. An example of a wave-vector to which this operation can be applied is shown in **Fig. 1.6 a**. The relation dispersion for any vector that lies on the dotted line follows this equation:

$$w = \frac{c}{n}\left[k_{\Gamma X}^2 + \left(\frac{2p}{a}\right)^2\right]^{1/2}$$

where $k_{\Gamma X}$ is the projection of **k** in the ΓX direction. The result is plotted in **Fig. 1.6 b**. (dashed line) and the reduced-zone scheme representation is shown in **Fig. 1.7 a**. The whole band structure (**Fig. 1.7 b**) is calculated[3] for a square array of cylinders (radius=0.3*a*) with a RI of 1.261 and embedded in a dielectric with *n*=1.260. All the important directions in the first BZ are depicted in this representation. The frequency is normalized by the lattice parameter and other constants to explicitly state the scalability of the calculations and the real structure ($wa/2\pi c$ is a typical expression for normalized frequencies, a/l is used instead many times and it is completely equivalent. Both of them are dimensionless). Of course, there are infinite other positions in the reciprocal lattice that can be translated in this way to the ΓX segment. As a result, many other curved bands appear at higher energies.

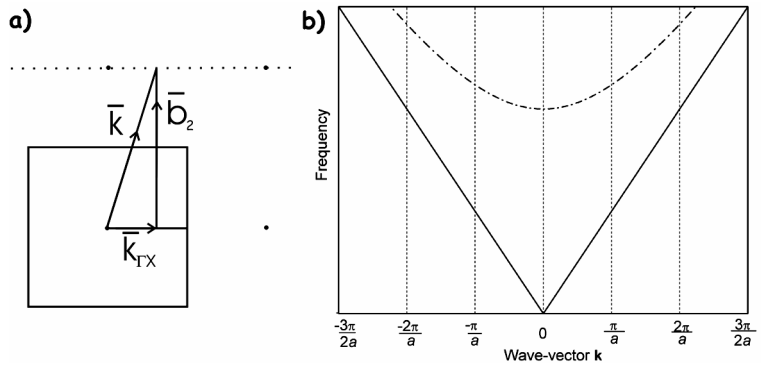

Fig. 1.6: In a) the wave-vectors **k** can be translated to the ΓX segment applying the translation operation $-\mathbf{b_2}$. Any wave-vector that lies on the dotted line can be translated with a linear combination of $\mathbf{b_1}$ and $\mathbf{b_2}$. The relation dispersion for this kind of vectors is plotted in b) (dashed line). The frequency is in arbitrary units.

The representation of band structures for 3D photonic crystals is done similarly. However, the number of high-symmetry points is usually higher and the possibilities of having bands that come from non-linear dispersion relations are

also larger. Generally speaking, the complexity of the band structure increases as the dimensionality of the system rises. In appendix I the BZs of the most common lattices are briefly described along with their most important high-symmetry points.

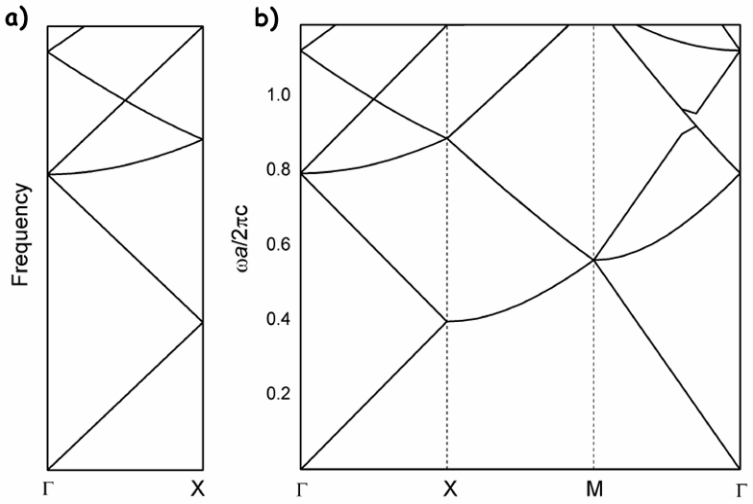

Fig. 1.7: a) The reduced-zone sheme for wave-vectors propagating in the ΓX direction calculated from the dispersion relations. b) Plane wave calculation of the band structure for photons propagating in the most important directions of the first Brillouin zone of a square lattice made of cylinders (radius=0.3*a* and *n*=1.261) embedded in a dielectric (*n*=1.260).

1.1.4 Pseudo-gaps and complete photonic band gaps.

When light enters into a photonic crystal it is scattered at the interfaces between different dielectric regions. Due to the periodicity, scattering can be coherent for certain directions and frequencies. As a result, some propagation directions are forbidden for photons of certain energies. In the photonic band structure diagram this is represented as a range of energies not covered by any band in that direction: this is called a photonic band gap.

The photonic crystal represented in **Fig. 1.7 b** has almost no RI contrast (*d*) between different dielectric regions (*d*=1.0008) and scattering effects are very weak. Consequently no gaps are observed. However, if *d* is increased, gaps begin to open. In **Fig. 1.8** the band structure for the ΓX direction is compared to the theoretical transmission spectrum[4] for the same structure with *d*=1.5 since the RI of the cylinders is now set to 1.890. As can be observed, between the first and second band (plotted in black and red respectively) there is a region of energies where no bands are available. As a result, photons of these energies cannot propagate through the crystal and, therefore, transmission goes to zero at those frequencies. The interpretation of the band structure is not always such a trivial task. It may happen that photons do not couple to states that are apparently available (the region is covered by a band). An example of this can be seen in **Fig. 1.8** for a normalized frequency around 0.7. Despite the third band (in green), some transmission dips

can be observed. Coupling of photons to certain bands depends on symmetry considerations which are out of the scope of this introduction.[5]

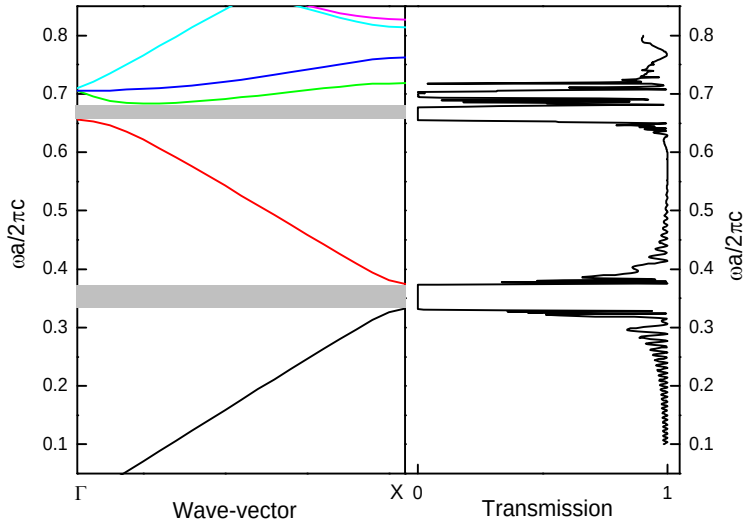

Fig. 1.8: The band structure (plane wave method) in the ΓX direction (left panel) is compared with transmission (right panel) theoretical calculations (transfer matrix method) for a square lattice made of cylinders (radius=0.3*a*) with a refractive index contrast (*d*) of 1.5. Gaps between bands (grey labels) result in transmission dips. (Only TE modes).

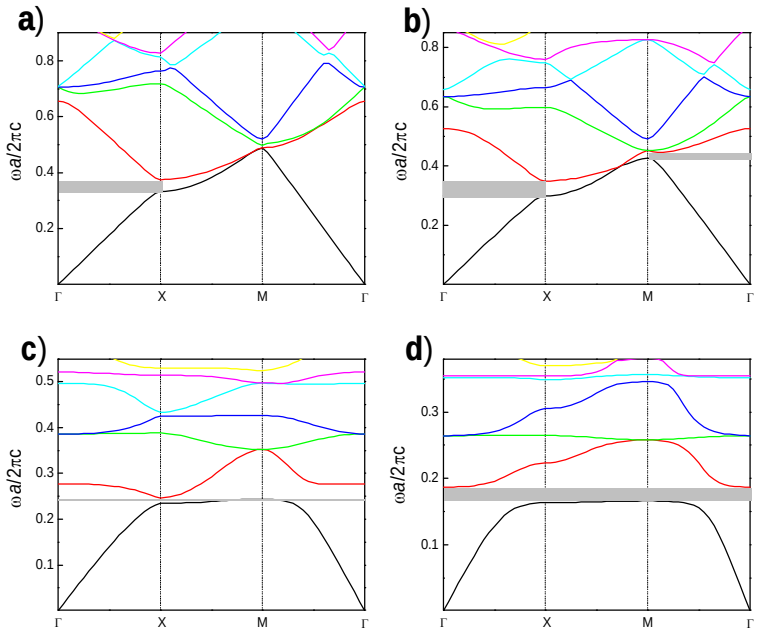

Fig. 1.9: Band structure calculations (plane wave method) for different *d* values of a square lattice made of cylinders (radius=0.3*a*). a) *d*=1.5, b) *d*=2.0, c) *d*=4.0 and d) *d*=6.0. a) and b) show pseudogaps and c) and d) a complete photonic band gap (grey labels). (Only TE modes).

Fig. 1.9 shows the photonic band structures for the same photonic crystal in which *d* is gradually increased: a) 1.5, b) 2.0, c) 4.0 and d) 6.0. In the first case, a gap appears in the ΓX direction (same as that depicted in **Fig. 1.8**). When *d* is augmented to 2.0, another gap opens in the ΓM direction. A further increment of *d* causes both gaps to overlap. As can be observed in c) and d) the gap occurs now for all propagation directions. This means that photons within that range of frequencies cannot propagate through the crystal. Under these circumstances the gap is called *complete photonic band gap* (cPBG). Conversely, gaps that are open just for certain directions (as those shown in **Fig. 1.9 a** and **b**) are called *pseudogaps*.

Obtaining a cPBG strongly depends on having a high *d* value. As **Fig. 1.9** shows, for a square lattice of cylinders such as the one described before, no cPBG opens until $d>4.0$. From a practical point of view this means that achieving a cPBG in the optical regime with this kind of lattice is very difficult since few materials with such a high RI exist in nature. Fortunately, formation of cPBGs is not only a question of large refractive index contrasts. The choice of an appropriate symmetry and topology plays a very important role as well.

To obtain a cPBG, the pseudogaps for different propagation directions must overlap. Increasing *d* usually entails the widening of gaps and facilitates this overlapping. However, if pseudogaps for different directions open at very dissimilar energies, the overlapping is less probable. From solid state physics we know that gaps happen for wave-vectors that lay on the BZ boundary. Consequently, photonic crystals with a circular BZ will have pseudogaps opening at similar frequencies and therefore will be better to achieve a cPBG. For 2D photonic crystals, a hexagonal lattice would be a wiser election than a square lattice. In the case of 3D photonic crystals a sphere-like BZ optimizes the lattice symmetry to obtain a cPBG. Among 3D Bravais lattices, the face centered cubic (fcc) one has the most sphere-like BZ (see Appendix I).

Topology of the lattice is also a parameter to take into consideration. Although not explained here, photonic crystals where high dielectric constant regions which are both all but isolated and linked by narrow veins favor the opening of cPBGs.[6] **Fig. 1.2 d** shows a 3D example of such topology.

1.1.5 Light within Photonic Crystals. Anomalous band dispersion.

It is well known that when light with a given frequency (w) passes from one dielectric with a certain RI (n_1) to another (with n_2) the propagation direction changes (see **Fig. 1.10 a**). This phenomenon is called refraction. In the wave-vector space, the parallel components of the wave-vector must be conserved.[7] Of course the energy, and therefore the frequency, is also conserved. As $w=ck/n$, the equi-frequency surfaces (EFS) follow this form: $w=c/n\ (k_{\wedge}^{2}+k_{||}^{2})^{1/2}$. This means that the EFSs have a circular shape (spherical in 3D). We also know that propagation direction can be obtained from the group velocity expression: $\mathbf{v}_g=\nabla_k w$. **Fig. 1.10 b** shows the EFSs for photons with a certain energy in two different dielectrics where $n_1<n_2$. Knowing that the parallel component of the wave-vectors must be conserved

and that $\mathbf{k_2}$ must be normal to the EPS the Snell law can be easily deduced. Indeed, $k_{i||}=k_i \cdot \sin(q_i)$ and $k_i=wn_i/c$, therefore $n_1 \cdot \sin(q_1)=n_2 \cdot \sin(q_2)$. In the case of circular EFSs, $\mathbf{v}_g$ and $\mathbf{k_2}$ will be parallel.

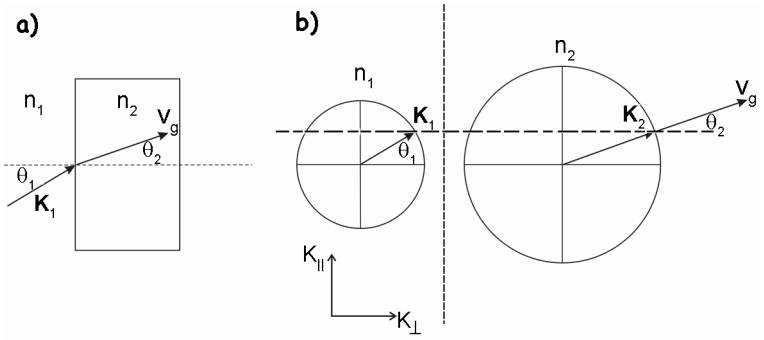

Fig. 1.10: Refraction of light when it enters a material with a different refractive index. Refraction scheme in the a) real space and b) in the wave-vector space. The parallel component of the wave-vector is conserved and the propagation direction is derived from the gradient on the equi-frequencial surface.

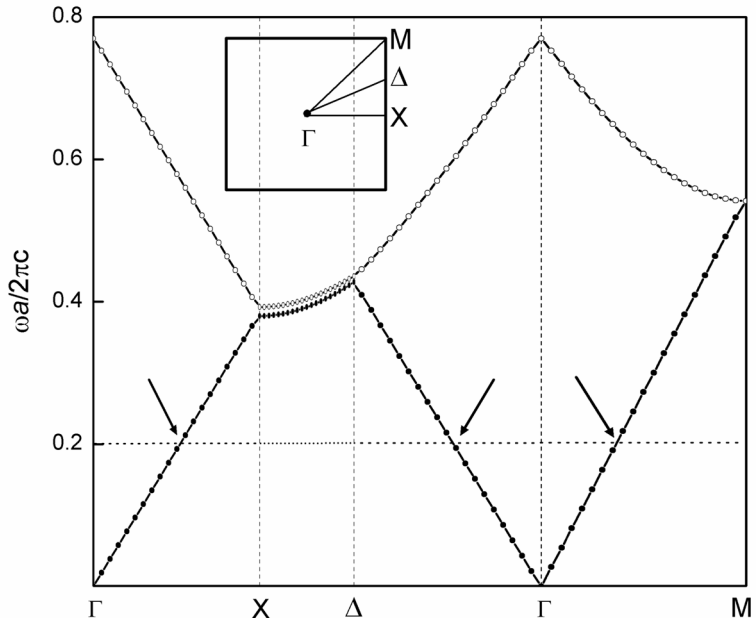

Fig. 1.11: Photonic band structure showing the first two bands of a square lattice of cylinders (r=0.3a) with d=1.10. The inset shows the Brillouin zone and the points at which the structure has been calculated. For a given frequency the branches are intercepted (horizontal dotted line) at different values for the wave-vector. (Only TE modes).

This holds for isotropic dielectric materials but, what happens with photonic crystals? The dispersion relation depends on the RI and this is not isotropic any more. In order to plot the EFS, it is necessary to know the allowed wave-vector for each direction. This information can be extracted from the photonic band structure.

Fig. 1.11 shows the first two bands* of the same square lattice presented before with a d=1.10. For a given normalized frequency (w=0.20) the wave-vector values are obtained for three different directions: Γ-X, Γ-Δ and Γ-M. With this information only three points of the EFS are obtained. Bands for other directions must be calculated to complete the EFS. Fortunately only directions within the irreducible zone are needed since the EFS must have the same symmetries than the BZ.

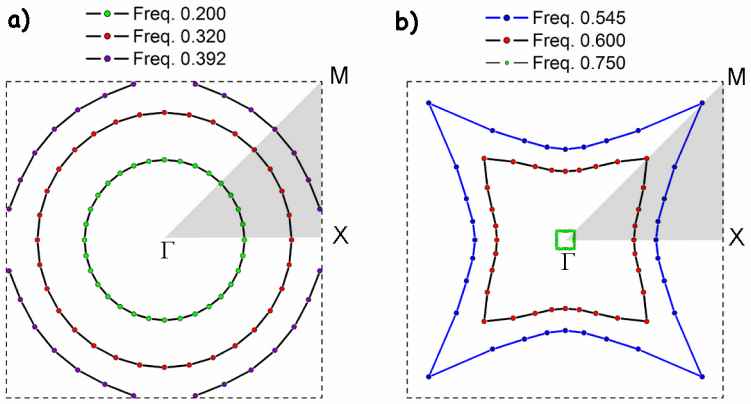

Fig. 1.12: Equi-frequency surfaces for a photonic crystal made of cylinders (r=0.3a) in a square lattice with d=1.10. a) EFSs for two frequencies below the psedogap and another frequency that overlaps with the pseudogap (w=0.392). The EFSs are obtained from the first band, their shape is circular and their radii increase with frequency. b) EFSs for frequencies above the pseudogap and belonging to the second band. The shape of the EFSs is star-shaped and its size decreases with frequency. (Only TE modes). The irreducible zone is shaded in grey.

Fig. 1.12 shows the EFSs for several frequencies. Although 32 points form the EFSs, in fact only five points were calculated within the irreducible zone (shaded areas) for each of them, symmetry properties allow to infer the rest. In **Fig. 1.12 a** three EFSs obtained from the first band are represented. The first two EFSs have a circular shape and their radii increase with frequency. This means that refraction of photons at that energy is similar to that of conventional isotropic dielectrics. The reason is that for low energies the wavelength of photons is large compared to the periodicity of the photonic crystal and the material is "seen" as homogenous. When the frequency of the EFS lies in the pseudogap (w=0.392), the surface is discontinuous and wave-vectors with certain directions do no propagate through the photonic crystal. It is also interesting to notice that curvature of the EFS close to the BZ is different from the rest since effective refractive index is higher here. The shape of the EFSs dramatically changes when frequencies above the

* Surfaces corresponding to other bands should be plotted as well since photons may couple to several bands when more than one is available. Each band would have its own EFS and light would be diffracted when more than one possibility were available. For the sake of explanations simplicity only two bands will be used for calculations here.

pseudogap are scanned. **Fig. 1.12 b** shows EFSs for three different frequencies that belong to the second band. This time the shape is not circular at all and its size decreases with frequency, therefore $\mathbf{v}_g$ (which gives the propagation direction) points inwardly. The non-circular shape of the EFS will entail an anisotropic response of the photonic crystal in terms of refraction (which is always assumed to be in the forward direction). The propagation direction is not necessarily parallel to the wave-vector anymore. As an example, **Fig. 1.13** shows the refraction of two photons with same frequency (w=0.545) and different incidence angle. In the first case (**Fig. 1.13 a**) the photon propagates through the crystal with a very small change in its direction as if the photonic crystal were a dielectric with a RI close to that of the environment. In the second case (**Fig. 1.13 b**) the EFS presents a strongly curved shape in the point where conservation is held, therefore there is a drastic change in its propagation direction. So drastic that the resulting refraction is negative!

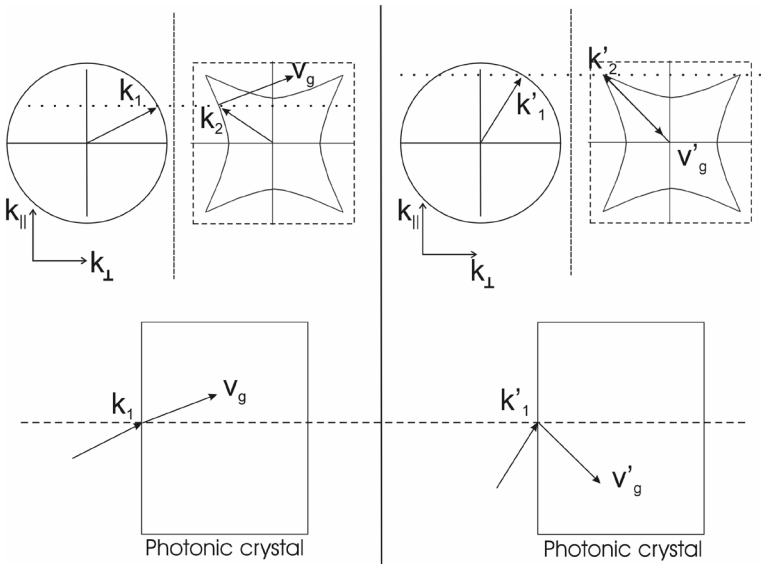

Fig. 1.13: Anomalous refraction for photons with w=0.545 for a square lattice of cylinders with d=1.10. a) and b) show examples for two different angles of the impinging photons. Propagation direction is obtained from the group velocity $\mathbf{v}_g=\nabla_{\mathbf{k}}w$. In the first case light is slightly refracted while in the second case photons are negatively refracted.

Depending on the curvature of the EFS the photonic crystal may behave as a collimator, a divergent lens or a convergent lens as shown in **Fig. 1.14**.[8] Negative refraction can be achieved as well for photonic crystals with a high d since EFS tend to be more circular above the gaps and $\mathbf{v}_g$ still keeps pointing inwardly.[9] Although negative refraction effects can be achieved for non-circular EFSs, circular EFSs allow defining a (negative) RI that remains constant for all propagation directions.

It is important to realize that anomalous refraction in photonic crystals does not depend on the existence of a cPBG. Actually, the effects shown in **Fig. 1.14** are

more likely observed in structures with a low *d* value. In 3D photonic crystals, the behavior is basically the same. The main difference is that real space and wave-vector representations are three dimensional and this makes its comprehension harder.

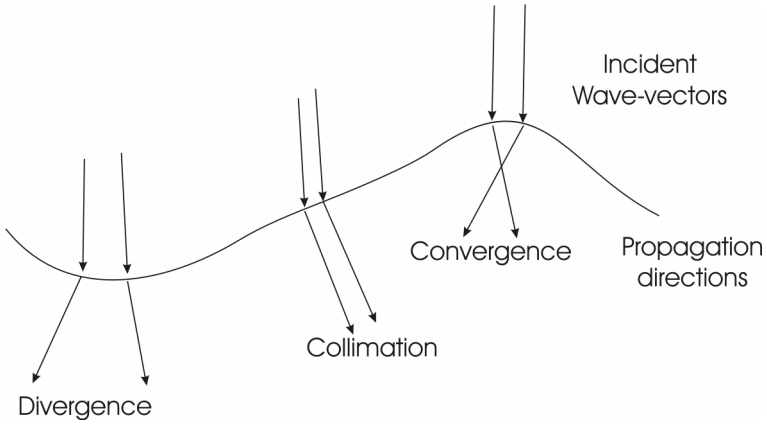

Fig. 1.14: Behavior of photons of same frequency for different curvatures of the EFS. For some range of directions and energies, photonic crystals may act as collimators, convex or concave lens.

1.1.6 Defects.

As it happens with semiconductors, the interest of photonic crystals with a cPBG would be limited without the inclusion of controlled defects. A defect creates allowed states for particular photon frequencies in the band gap.

A line defect within a photonic crystal can guide photons through the system. If the frequency of light lies within the cPBG, it will have to be confined to the defect line since propagation is forbidden through the rest of the photonic crystal. The advantage of such a system over conventional optic fibers or waveguides is that in this case, light confinement does not rely on total internal reflection. Therefore sharp bends should not present any transmission losses (only reflection).

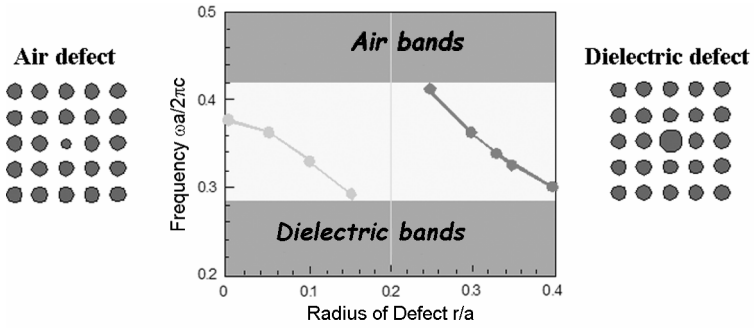

Fig. 1.15: Point defects in a square lattice made of dielectric rods (radius=0.2*a*). Depending on the radius (*r*) of the point defect, localized states are created within the cPBG. This figure has been extracted from ref. 6.

Point defects are of paramount importance for spontaneous emission inhibition[10] and light localization.[11] A point defect consists of an imperfection created deep in the bulk of the crystal. It can be obtained by removing one of the building blocks, changing its refractive index or modifying its size. In **Fig. 1.15** we can see an example of the effects on the band structure of a point defect in a square lattice of dielectric rods. In this case defects are created by varying the radius of the cylinders. When the defect involves the removal of dielectric it is called air defect and an allowed mode appears close to the bands below the cPBG (also called dielectric bands) and evolves towards bands above the cPBG (air bands). Conversely, defects involving dielectric addition are called dielectric defects and the cavity mode evolves from air to dielectric bands as dielectric is added.[6] Point defects can be regarded as cavities in which light can be trapped and their size and topology can be designed to tune the frequency of the resonance.

Spontaneous emission is directly related to the density of states (DOS) since the emission rate of an atom depends on the density of available *em* modes for the emitted photon. DOS can be modified and conveniently tailored with the combination of cPBGs and resonant cavities. The magnitude describing the confining power of the cavity is called quality factor $Q \equiv w/\Delta w$, where w is the frequency of the transition and Δw is the frequency width of the resonance.

1.1.7 Applications.

The numerous potential applications for photonic crystals have made this research field very appealing to many scientists. Some of the possible applications are shown here.

Although it is still under study, the effects of anomalous dispersion are very promising. Photonic crystals without a cPBG can be designed to obtain super-collimators and super-lenses (see **Fig. 1.14**).[8] Based on the same effect, two photons that impinge a photonic crystal with the same angle but a slightly different energy, may find EFSs with a very different curvature. As a consequence their propagation angles would be very dissimilar. This is known as super-prism effect and could be applied to the fabrication of small integrated multiplexers.[12] Besides, all-angle negative refraction[13] (**Fig. 1.16**) can be used to obtain super-lenses that could potentially overcome the diffraction limit inherent in conventional lenses.[14] The origin of this negative refraction must not be confused with that obtained in left handed materials[15] where both the dielectric constant and magnetic permeability are negative.

Fabrication of integrated circuits in which information carriers were photons instead of electrons is one of the most expected applications for photonic crystals. In this sense wave-guides (WG) based on 2D photonic crystals have been designed by researchers at MIT[16-19] (see **Fig. 1.17**) and are being continuously improved by engineers. Although there is already a large amount of work done on WGs based on total internal reflection, photonic crystals provide some advantages. For example sharp bends in a photonic crystal based WG do not present losses as high as those based on total internal reflection. In order to obtain integrated circuits that

could perform logical operations a photonic transistor would be necessary. In this sense John *et al.*[20] has proposed a system based on two-level atoms having population inversion near the cPBG edge.

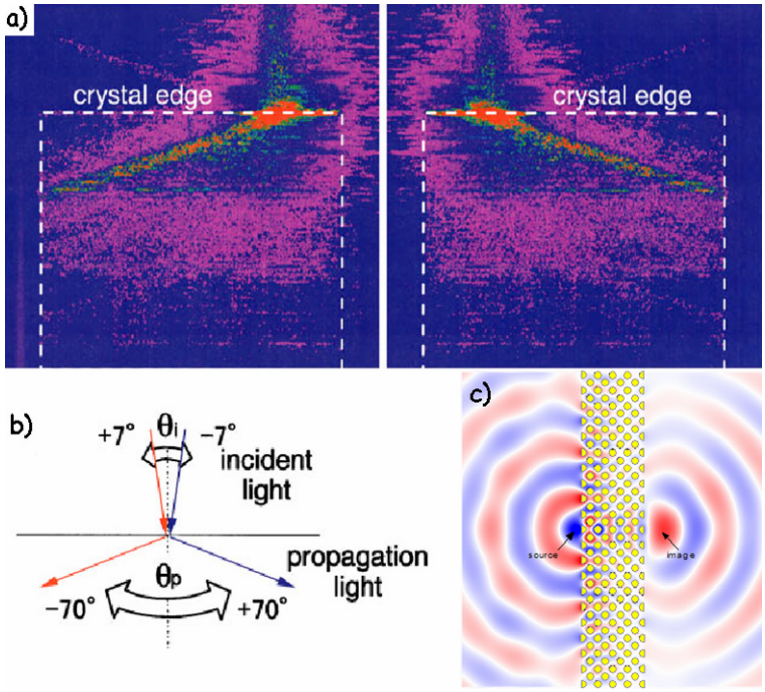

Fig. 1.16: Negative refraction. a) experimental observation of negative refraction as explained in the scheme b) (both images taken from ref. 12). Negative refraction could be used to fabricate *super-lenses* (image taken from ref. 21).

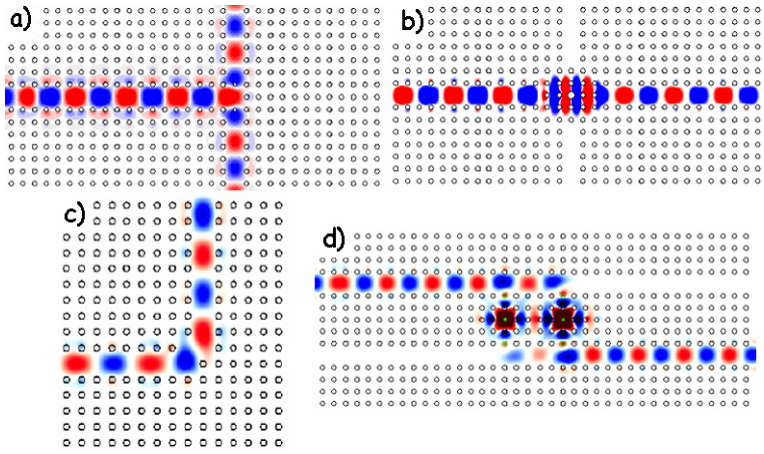

Fig. 1.17: Waveguides. a) wide-angle splitter, b) wave-guide crossing, c) lossless bends and d) channel-drop filter. Images extracted from refs. 16-19.

Optical fibers based on photonic crystals are one of the applications already being commercialized. **Fig. 1.18** shows two examples of these fibers. The first

case, the "omni-fiber",[22] is a hollow core surrounded by an omni-directional Bragg reflector.[23] The Bragg reflector is in reality a 1D photonic crystal which consists of a stack of layers. In the second case, the fiber is again a hollow core but this time surrounded by a 2D photonic crystal.[24]

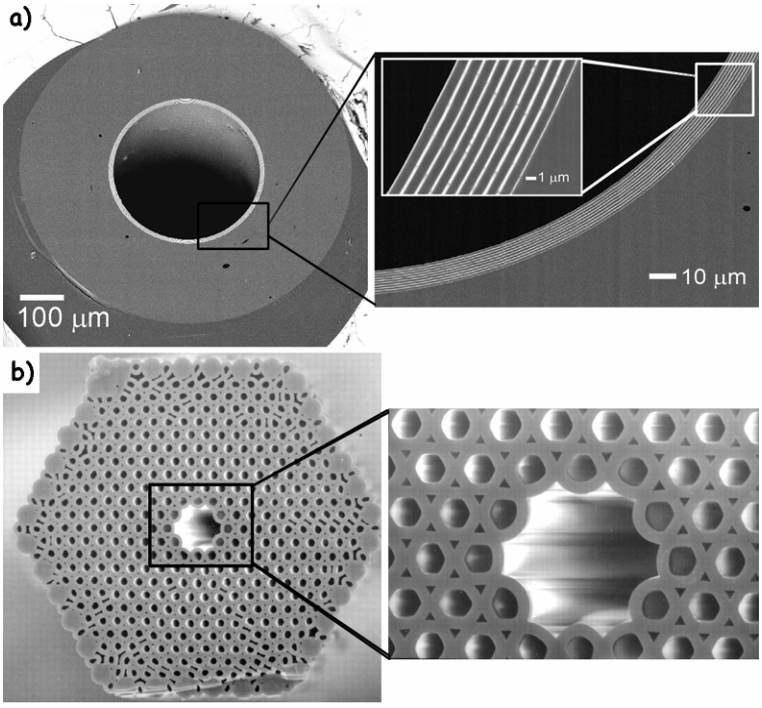

Fig. 1.18: Photonic fibers. a) Cross-section images of the omni-guide (ref. 22). This guide is based on the omnidirectional Bragg mirrors. The fiber in b) consists of a hollow core surrounded by a 2D photonic crystal that confines light within the core (ref. 24).

Inhibition of infrared thermal emission has been demonstrated by Fleming *et al.*[25] with metallic photonic crystals that could be used as highly efficient light sources. Low-threshold lasers[26] are already being developed although, so far, presented works are limited to 1D and 2D photonic crystals. In the microwave regime photonic crystals can optimize performance and directionality of antennas.[27]

1.2 Calculation methods.

As a consequence of the similarities found between electron bands in solid state physics and photonic bands many of the calculation techniques and concepts applied and developed in the former discipline find an use in the latter. An excellent comparison between both can be found in Appendix A of reference 28.

The interaction of *em* radiation with photonic crystals can be modeled with the macroscopic Maxwell equations. As there are no free charges or currents these equations take the following form (Gauss units system):

$$\begin{aligned} \nabla \cdot \mathbf{B} = 0; \quad & \nabla \times \mathbf{E} + \frac{1}{c}\frac{\partial \mathbf{B}}{\partial t} = 0; \\ \nabla \cdot \mathbf{D} = 0; \quad & \nabla \times \mathbf{H} - \frac{1}{c}\frac{\partial \mathbf{D}}{\partial t} = 0 \end{aligned} \tag{1}$$

where **E** and **H** are the macroscopic electric and magnetic fields and **D** and **B** are the displacement and magnetic induction fields.

These equations are difficult to solve even numerically; however, there are certain assumptions that simplify calculations very much. Obviously these assumptions will restrict the number of cases in which results can be applied. Nevertheless, the results obtained from simplified equations will be valid for all the photonic crystals presented in this thesis. Here forth our system will be constrained by the following assumptions:

a) The system has a linear response to *em* radiation.

b) The material composing the photonic crystal is isotropic and macroscopic.

c) The frequency dependence of the dielectric function is neglected. Its value is assumed to be constant for the frequency range where results are required.

d) Magnetic permeability is assumed to be unity.

From a) and b) we have that $\mathbf{D}=e(\mathbf{r},w)\cdot\mathbf{E}$, from c) $e(\mathbf{r},w)=e(\mathbf{r})$. Finally from d) we can conclude that $\mathbf{H}=\mathbf{B}$.

Due to the linearity of Maxwell equations, harmonic modes can be separated into a space dependent field pattern and a time dependent sinusoidal expression:

$$\mathbf{E}(\mathbf{r},t) = \Re\{\mathbf{E}(\mathbf{r})\, e^{iwt}\} \tag{2}$$

where a complex exponential is used to simplify notation. The same can be done with **H**, **B** and **D**. Thanks to these expressions, the time dependence can be dropped from Maxwell equations:

$$\begin{aligned} \nabla \cdot \mathbf{B}(\mathbf{r}) = 0; \quad & \nabla \times \mathbf{E}(\mathbf{r}) + \frac{iw}{c}\mathbf{B}(\mathbf{r}) = 0; \\ \nabla \cdot \mathbf{D}(\mathbf{r}) = 0; \quad & \nabla \times \mathbf{H}(\mathbf{r}) - \frac{iw}{c}\mathbf{D}(\mathbf{r}) = 0 \end{aligned} \tag{3}$$

If these equations are decoupled we obtain:

$$\nabla \times \left[\frac{1}{e(\mathbf{r})}\nabla \times \mathbf{H}(\mathbf{r})\right] = \frac{w^2}{c^2}\mathbf{H}(\mathbf{r}); \qquad \nabla \cdot \mathbf{H}(\mathbf{r}) = 0 \tag{4}$$

$$\frac{1}{e(\mathbf{r})}\nabla \times \nabla \times \mathbf{E}(\mathbf{r}) = \frac{w^2}{c^2}\mathbf{E}(\mathbf{r}); \qquad \nabla \cdot [e(\mathbf{r})\cdot\mathbf{E}(\mathbf{r})] = 0 \tag{5}$$

$$\nabla \times \nabla \times \left[\frac{1}{e(\mathbf{r})} \mathbf{D}(\mathbf{r}) \right] = \frac{w^2}{c^2} \mathbf{D}(\mathbf{r}); \qquad \nabla \cdot \mathbf{D}(\mathbf{r}) = 0 \tag{6}$$

Of course, solving any of the sets of equations from (4) to (6) is enough to solve the problem since **H**, **E** and **D** are closely related by equations shown in (3). The spatial periodicity of the dielectric function within the photonic crystal must be taken into account as well. Indeed, $e(\mathbf{r})=e(\mathbf{r}+\mathbf{R})$, where **R** is an atom location in the real lattice.

Mainly, there are three methods that have been extensively applied to the calculation of photonic band structures:[29] plane wave method, Green's functions expansion method and finite, time or frequency, difference method. The first one computes the available energy states for a given wave-vector within the BZ. The other two methods look for all the wave-vectors for a given energy.

1.2.1 Plane Wave Method (PWM).

The PWM is an adaptation of a classical method to calculate band structures in semiconductors that takes advantage of the periodicity of the lattice. Translational symmetry allows expanding fields in terms of Bloch-vectors.[1] The dielectric function periodicity permits obtaining its Fourier transformation (in the wave-vector space) only in terms of reciprocal lattice vectors. Fourier transformation is now a discrete summation and the problem is reduced to diagonalize a matrix.

Apart from all the assumptions explained before, the PWM requires a real dielectric function; this means that the composing materials of our photonic crystal must be lossless.

1.2.1.1 Full vector calculations.

In the case of *em* radiation the field used for calculations is the macroscopic magnetic field $\mathbf{H}(\mathbf{r})$. $\mathbf{E}(\mathbf{r})$ or $\mathbf{D}(\mathbf{r})$ could be used for calculations as well, but on the one hand the operator applied on $\mathbf{D}(\mathbf{r})$ (left side of equation 6) is not Hermitian and on the other hand $\mathbf{E}(\mathbf{r})$ is not a continuous function. Conversely $\mathbf{H}(\mathbf{r})$ is a continuous field and the operator applied to it (left side of equation 4) is Hermitian. These facts simplify calculations and allow some symmetry properties to be applied in a straight forward manner. (A more detailed discussion can be found in Chapters 2 and 3 of reference 28).

The expressions for $\mathbf{H}(\mathbf{r})$ and $\varepsilon(\mathbf{r})$ in the reciprocal space are:

$$\begin{aligned} \boldsymbol{H}(\boldsymbol{r}) &= e^{i\boldsymbol{k}\boldsymbol{r}} h(\boldsymbol{r}) \hat{e}_{\boldsymbol{k}}; \\ h(\boldsymbol{r}) &= h(\boldsymbol{r} + \boldsymbol{R}); \\ e(\boldsymbol{r}) &= \sum\nolimits_{\boldsymbol{G}} e(\boldsymbol{G}) e^{i\boldsymbol{G}\boldsymbol{r}} \end{aligned} \tag{7}$$

where **k** is a wave-vector in the BZ, $e_{\mathbf{k}}$ is a unit vector perpendicular to **k** and parallel to **H** (polarization vector), and **G** is a vector of the reciprocal space lattice (see Appendix I for more information).

Combining expressions in (4) and (7), we obtain a 2*N* x 2*N* matrix problem of eigenvalues that must be computed. *N* is the number of plane waves and the accuracy of the calculations increases with *N*. In this method the accurate calculation of the Fourier components of the dielectric function is especially important. (Appendix III shows calculations for some specific cases).

1.2.1.2 The scalar wave approximation (SWA).

In the scalar wave approximation the full vector character of *em* fields is neglected. Instead, light is treated as a scalar field and consequently the resulting equations are simpler. This approach is useful to obtain basic information without complicated calculations.

As an approximation, the utilization of SWA must be done very carefully since some of the results can lead to wrong conclusions. For example all the effects caused by polarization are neglected. Therefore some effects concerning band degeneracy can be mistreated.

A further simplification of this method consists in using just one plane wave. This is similar to the weak periodic potentials solved for semiconductors. If we are studying a specific direction, say the {111} direction, the Fourier expansion of the dielectric constant is truncated as $e(\mathbf{r}) = e(G_0) + e(\mathbf{G}_{111})\, e^{i\mathbf{G}_{111}\mathbf{r}}$ and all other terms are neglected. Calculations show that $e(G_0)$ is nothing but the average dielectric constant and $\varepsilon(\mathbf{G}_{111})$ can be easily calculated for many systems (see Appendix III). The eigenvalues problem is just a 2x2 matrix that can be analytically solved.

The solution of the eigenvalue problem gives rise to a simple equation from which important features can be calculated with a good degree of accuracy. Furthermore, appropriate boundary conditions may give us information about the transmitted field through a finite (in the propagation direction) crystal.

Contrary to full-vector calculations, this method fails for high RI values and high energy bands. However, for a number of systems this method gives a great amount of valuable information.

1.2.2 Green's functions. Korringa-Kohn-Rostoker method (KKR).

Again, this method is adapted from a classical procedure used in solid state physics to calculate semiconductors electronic band structures. It was independently developed by Korringa[30] and Konh and Rostoker.[31]

In the semiconductor case, the method begins with the integral form of the Schrödinger equation in terms of Green's functions. For photons the development is similar except for the complications brought about by the full vector character of *em* fields. At some point in calculations, it is assumed that vector field can be expanded, to a reasonable degree of accuracy, by a finite number of spherical harmonics.

The expansion of equations in terms of spherical harmonics is itself an advantage and a limitation at the same time. On the one hand, for systems made of spherical scatterers, the convergence of this method is very fast. Also, the

discontinuities of $\varepsilon(\mathbf{r})$ are accurately represented. On the other hand this method looses its effectiveness when scatterers are not spherical. For example, this method is ideal for colloidal crystals where ordered spheres are significantly apart from each other. However, for close packed arrangements where planes are much more interpenetrated or systems in which spheres are interpenetrated (**Fig. 1.12 b** or **d**) the spherical symmetry is lost. Another disadvantage is the lack of accuracy for high energy calculations ($a/l>1.2$).

A variation of this method called *layer-KKR* has been introduced to compute transmission and reflection spectra of finite (in the propagation direction) photonic crystals.[32] A detailed description and complete equations for the KKR method can be found in works published by Ohtaka,[33] Stefanou *et al.*[34] and Wang *et al.*[35]

1.2.3 Finite difference methods.

The transfer matrix method (TMM) is a real-space method specifically developed in 1992 by Pendry *et al.*[36] to compute the transmission and reflectance spectra of photonic crystals. This method represents a finite difference frequency domain (FDFD) approach based on a discretization of Maxwell's equations for time harmonic *em* fields. The space is divided into a set of small cells with coupling between neighboring cells. The dispersion relation is given through the eigenvalues of a transfer matrix that connects the field distribution of the final space division with the initial one. Alternatively, Chan *et al.*[37] and Sakoda *et al.*[38] developed a method based on finite difference time domain (FDTD) approach. Instead of Maxwell's equations the wave equation is discretized in the time domain. Solutions within the photonic crystal are obtained for the Bloch boundary condition provided by the wave vector under consideration.[29]

The advantages of these methods are that there are no conditions over scatterer shape, absorption effects can be taken into account by introducing imaginary values in the dielectric constant. Furthermore, with appropriate modifications to the boundary conditions, calculations can be performed on finite size (in the propagation direction) photonic crystals or defect structures.[39]

1.3 Fabrication methods.

Several approaches have been followed to fabricate 3D photonic crystals whose properties lie on the optical regime. Crystal periodicity varies from several hundred nanometers if needed for application in the visible (vis) regime to a few microns for those operating in the near infrared (NIR). The techniques that have been most widely used are those based on lithography and the preparation of artificial opals to be used as templates. More recently introduced but very promising is holographic lithography.

Other fabrications methods are continuously being developed and have provided interesting results. Among the many existing examples we could mention block-copolymers self-assembly,[40,41] focused-ion-beam milling (see **Fig. 1.19 a**),[42] glancing angle deposition[43] and nanorobotic manipulation.[44,45]

1.3.1 Lithography.

Lithographic techniques are based on the approach followed in microelectronics to fabricate electronic chips. The procedure begins with the recording of a 2D pattern on a resist deposited on a wafer (made of a high RI material such as Si or GaAs) by means of photo-lithography or electron-beam-lithography. The name of the technique depends on whether photons or electrons are used to write the pattern on the resist. Afterwards, the pattern is transferred to the wafer thanks to an etching process. To fabricate the 3D photonic crystal two procedures have been developed by Noda *et al*.[46,47] and Lin *et al*.[48,49] although both end up with the *woodpile* or *layer-by–layer* structure, designed in 1994 to show a cPBG between the first and second band.

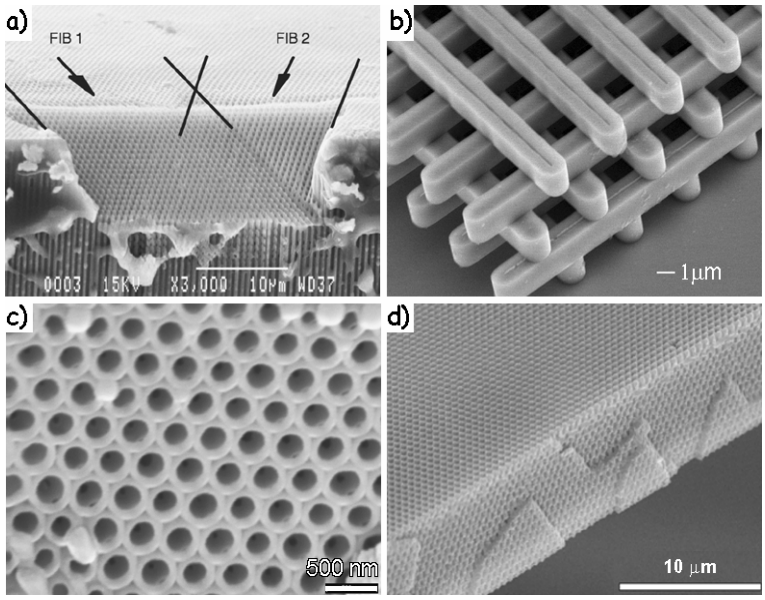

Fig. 1.19: Photonic crystals obtained by means of different methods: a) focus ion beam milling (ref. 42), b) photolithography (ref. 48), c) stibnite inverse opal (see ref. 50) and d) holography (ref. 59).

Noda and co-workers used a wafer-fusion technique.[51] A 2D basic structure made of parallel bars is made on a GaAs wafer by e-beam lithography and then snapped. Then, two halves containing the 2D structure are stacked face to face and fused (by wafer-fusion) so that second layer bars are perpendicular to those of the first. Then one of the substrates of the fused wafers is selectively removed. The result is a 3D structure made of two layers. At this point the wafer is cleaved and stacked again, but this time the alignment of the structure is critical since third layer bars must be parallel to those of the first layer while shifted half a period. The alignment of the structures is carried thanks to a laser beam diffraction pattern observation technique.[52]

Alternatively Lin *et al*. developed a five steps process in which for each layer (see **Fig. 1.19 b**), SiO_2 is first deposited, patterned (photo-lithography) and etched

to the desired depth. The resulting trenches are then filled with silicon and following this the wafer surface is flattened using chemical mechanical polishing. After all the procedure has been repeated (aligning is achieved thanks to line stepper systems) to obtain the required number of layers, SiO_2 is etched with HF. To reduce the minimum feature size of their crystals, a more complex technique relying on the use of fillet processing[49] was developed.

Thanks to lithographic processes photonic crystals with a cPBG at the NIR and made of up to eight layers have been fabricated. An important advantage of this method is the possibility of including linear defects in a relatively straight-forward manner. On the other hand, crystals with only a few layers have been obtained so far. It is also a very expensive procedure that many research laboratories cannot afford.

1.3.2 Artificial opals.

In 1992 Sözüer *et al.*[53] demonstrated that an fcc structure made of touching air-spheres embedded in a high RI material (n>2.8) could show a cPBG between the 8th and 9th band.

The first structure made of touching air spheres with an fcc symmetry (see **Fig. 1.19 c**) was obtained by Velev *et al.*[54] in 1997. In this work they fabricated crystalline structures assembled from polystyrene latex microspheres. These crystals were used as templates for silica polymerization. Subsequently the latex was burned away leaving the desired structure. One year later, similar structures were presented by Zakhidov *et al.*[55] using artificial opals[56] (made of silica microspheres) as sacrificial templates. These structures were called hereafter inverse opals. However it was not until 2000 that Blanco *et al.*[57] fabricated the first inverse opal with a RI contrast high enough to show a cPBG (air spheres in silicon).

The fabrication of artificial opals by means of self-assembly techniques offers a cheap method available for many research laboratories. Among the possible limitations for self-assembly methods we could cite the restrictions to obtain symmetries other than the fcc lattice and the difficulties to control the appearance of unwanted (and wanted) defects. However, thanks to the increasing number of researchers in this field, the novel methods that are being developed everyday offer very interesting and unexpected alternatives.

As fabrication of artificial opals will be the basis for this thesis, further information and detailed discussion of methods will be provided in next chapters (especially in chapters II to IV).

1.3.3 Holography.

An interference of four non-coplanar coherent laser beams forms a 3D structure. This structure is periodic and its periodicity and symmetry can be controlled. Creating this interference within a photoresist renders insoluble the area which has been highly exposed. Unexposed photoresist is then dissolved away to reveal a 3D structure formed of crosslinked polymer with air-filled voids. This

technique is known as holographic lithography. The application of this method to 3D photonic crystals was firstly proposed by Berger *et al*.[58] in 1997 and its viability was empirically demonstrated by Campbell *et al.* in 2000 (see **Fig. 1.19 d**).[59]

The intensity and polarization of each laser beam, along with their wave-vector, are the parameters which will determine the resulting photonic band structure. The success of this technique is based on the use of an especial photoresist named SU8.[60] This photoresist shows low radiation absorption and presents no photorefractive effect (the RI is not changed by intense *em* radiation).

The advantages of this method are numerous. Firstly a 3D photonic crystal can be obtained in a very short period of time (a few minutes). Secondly, the number of parameters allows considerable freedom to design different symmetries and unit cell distribution. Thirdly, the process is relatively cheap. And finally, the method is scalable for large-scale production.

This method is still being developed and improved.[61] First optical spectra are being presented and the fabrication of a photonic crystal with a cPBG with this method is expected for the near future.

1.4 History and state of the art.

The interest of researchers in the field of photonic crystals has been incessantly growing since they were proposed in 1987. The amount of published work (**Fig. 1.20**) shows a spectacular exponential growth and, at present, there are no signs indicating saturation. The number of papers coming out each year is so high that it is hard to keep track of even the most significant achievements.

In this section a brief summary of the most important works related to photonic crystals will be presented. The section has been divided in four periods of time: before the photonic band gap proposal in 1987, the first years after it (1987-1994), a second period from 1995 to 1999, and from 1999 to date (2003). The last period has been chosen to coincide with the lapse of time in which the work presented in this PhD thesis has been developed. That way, the reader will be able to take into account the context in which each task was developed and the current state of the art.

1.4.1 Before 1987.

The creation of terms like “photonic crystals” and “photonic band structures” did not occur until 1987. However, the interaction of light in the optical regime with ordered dielectric structures had been already observed and studied before terms such as photonic band gap or photonic crystal were invented.

Colloidal particles with diameters close to the optical wavelength were available in the first half of the 20th century since the “Dow Chemical co.” commercialized polystyrene microspheres. Structural analyses and light diffraction experiments were performed on the colloidal suspensions formed by these particles. The results were attributed to Bragg reflection of visible light.[62]

On May 15th 1979 Ohtaka published a dynamical theory of the diffraction of visible and ultraviolet light.[33] The aim was modeling the interaction of light with a dielectric system composed of identical spheres ordered in a three-dimensional lattice. The equations he presented were based on the KKR method and the formulation of low-energy electron diffraction (LEED). Both of them were tools widely used in energy bands calculations in semiconductors. To develop the new formalism he applied these methods taking into account that vector Helmholtz's equation was governing the behavior of photons (as Schrödinger's equations does electrons'). It is important to notice that Ohtaka took into account the full vector character of photons and did not use a scalar approximation.

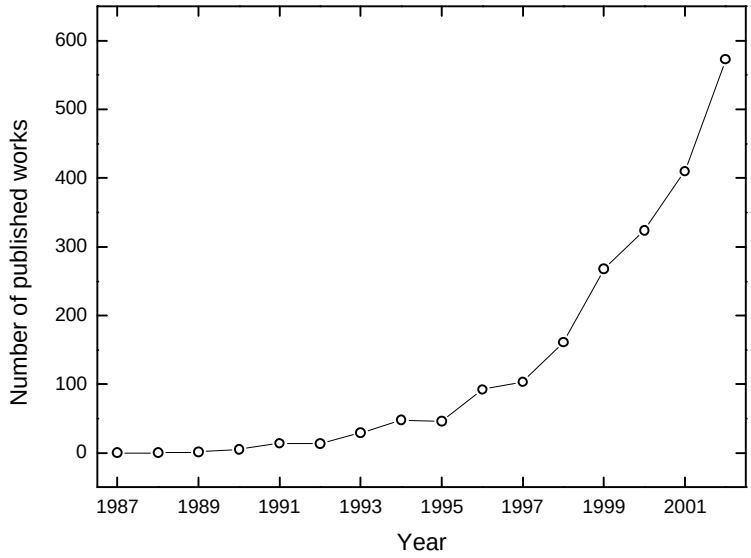

Fig. 1.20: Number of published works per year. Data was obtained by searching for "photonic crystal OR photonic band" at the ISI Web of Science.[63] (Data is not cumulative).

Even though Ohtaka developed his theory borrowing many aspects from semiconductors, he did not realize (or at least, he did not state it) the possibility of having photonic band gaps and their potential applications. For this reason his article has remained unknown during many years to some of the photonic band gap researchers that, actually, have partly repeated his work (see next sections). Besides, the systems he modeled (three dimensionally ordered spherical scatterers) in that paper have also had a tremendous importance as photonic crystals.

1.4.2 From 1987 to 1994.

On May 18th 1987 two independent works appeared in the same issue of the well known journal "Physical Review Letters". The first one was published by Yablonovitch[10] (at Bell Communications Research, USA) and dealt with the possibility of inhibiting spontaneous emission of *em* radiation using a three-dimensionally periodic structure. This lattice should have a photonic band gap, this is, a region of forbidden energy states for photons. The second paper was signed by Jonh[11] (at Princeton University, USA). In that work John discussed the strong

Anderson localization[64] of photons in carefully prepared disordered dielectric superlattices. Defects present within a lattice where certain energy states were forbidden for photons should trap *em* radiation. These two works are considered as the origin of the research field henceforth known as "photonic crystals or photonic band gap materials".

After publishing their work, there were not many clues about which kind of structure should be fabricated. They knew that a lattice with a spherical BZ would help since gaps for different directions would appear at similar energies. Following that argument, the face centered cubic (fcc) lattice seemed to be the best. In order to achieve an overlapping of the gaps at every point of the BZ boundary, a high refractive index contrast (*d*) between the composing materials was required.[10] However very little was known about the minimum values of refractive index for each material and the optimal lattice topology needed to obtain a crystal with a cPBG.

About one year and a half later (1989), John published another work in which he announced that an fcc structure could show a cPBG between the second and third band.[65] Applying the KKR method with the scalar wave approximation he showed that an fcc lattice with a filling fraction of 11% and *d*=3.45 should show a cPBG of a 13% gap to midgap ratio. Other values could show narrower cPBGs. With these data Yablonovitch began to work on the construction of lattices that could prove John's results experimentally. The empirical procedure followed by Yablonovitch *et al.* consisted on a cut-and-try method and *"dozens of fcc structures were painstakingly machined out of low-loss dielectric materials"*.[66] The experimental results from this work showed little agreement with theoretical calculations. The *d* needed for a cPBG seemed to be larger than expected and the behavior of photons at the W point of the BZ was not understood. A degeneracy of two bands due to group-theoretical properties of the W point was apparently the reason for this behavior.[67] Including the full vector nature of the *em* radiation instead of using a scalar wave approximation in the theoretical calculations would take this fact into account.

1990 was a very critical and exciting year for photonic crystals. At the beginning of this year, and with a few weeks difference, Satpathy *et al.*[68] and Leung *et al.*[69] independently published an implementation of the plane wave method with the scalar approximation (PWM) to photonic band calculations. Their work confirmed the KKR results obtained by John. However, shortly after (May of 1999) both groups improved the PWM taking into account the full vector nature of light.[70,71] Their papers appear one after the other in the same issue of "Physical Review Letters". This time theoretical calculations and experimental data showed an excellent agreement. Unfortunately calculations confirmed that the cPBG that had been previously predicted for an fcc crystal, did not actually exist.

These events lead the editor of the well known journal "Nature" to assure that *"Photonic Crystals bite the dust"*.[72] Only two weeks later Ho *et al.* published a work in which they demonstrated that although fcc lattices with spherical atoms did not show the "missing" gap, a diamond structure (**Fig. 1.21 a**) should do it.[73] The

reason for the diamond structure success is that it requires two atoms per unit cell. Introducing non-spherical atoms in the fcc lattice may lift the degeneracy of the bands at the W point in the BZ (notice that diamond structure is an fcc lattice with a two-vector basis). Immediately after this discovery, Yablonovitch *et al.* submitted another work presenting a structure based on an fcc lattice with non-spherical atoms and which presented a cPBG, this structure was called "Yablonovite".[74,75] The structure consisted of a dielectric slab with a triangular array of holes with a set of parallel holes drilled as shown in **Fig. 1.21 b**. The resulting crystal is similar to a diamond lattice grown in the (111) direction with channels following the (110), (101) and (011) directions. It can be easily calculated that these vectors form an angle of $\alpha = \cos^{-1}(2/\sqrt{6}) \approx 35^{o}\ 15'$ respect to the normal and spread 120º on the azimuth. It is worthy mentioning that "Yablonovite" is not exactly like a diamond lattice since three more sets would be needed in the (-101), (-110) and (0-11) directions. However, these vectors are normal the surface and drilling implies some experimental difficulties. A sample was fabricated for the microwave regime to show the effectiveness of this configuration and the cPBG was experimentally demonstrated. Although it was suggested that fabricating this sample for the optical regime by chemical-beam-assisted etching would be relatively easy, it has taken about nine years to obtain such a structure working at a wavelength of 3 microns.[42]

In 1992, Sözüer *et al.* improved the plane wave method to show the behavior of higher energy bands.[53] Surprisingly, they showed that between the 8th and 9th band a cPBG was formed for an fcc lattice of air holes in a semiconductor (**Fig. 1.21 c**) when *d* was above 2.8. Ironically enough, lattices accomplishing this requirement had been experimentally studied by Yablonovitch *et al.*[66] but unfortunately they had not probed the behavior of those high energy bands.

Finally, in 1994, a new proposal of a structure with a cPBG was made by two independent groups.[76,77] The so-called woodpile or layer-by-layer structures (the name depends on the author) follow the diamond symmetry (see **Fig. 1.21 d**) and present a cPBG between the 2nd and 3rd bands. At that time, the advantage of this structure over the others was that, presumably, it could be constructed in the optical regime by means of photolithographic techniques.

1.4.3 From 1995 to 1999.

At the end of 1994 several structures with a cPBG had been proposed and one of them, the Yablonovite, had been fabricated in the microwave regime. It had been demonstrated that photonic crystals actually worked. The basic theoretical tools to calculate band structures and optical properties had been already presented. Some other calculation methods were developed during these years, but basically they complemented and improved those already published.[37,38] The challenge for the upcoming years was fabricating any of these crystals with a periodicity around the micron so that a cPBG could be observed at optical frequencies.

During these five years materials science had the key to continue with the evolution of photonic crystals. Mainly two methods were followed to obtain structures with a 3D micrometric periodicity: lithography and artificial opals.

The existing techniques in lithography for microelectronics made this approach quite appealing. Soon two groups at Sandia Labs (USA) and Kyoto university (Japan) begun to, independently, develop the necessary techniques to apply lithography for their purposes. During the second half of 1998 both groups presented four-layer crystals based on the woodpile or layer-by-layer structures. These crystals showed the effects of the band gap at mid-infrared wavelengths even though the number of layers was rather low.[46,48]

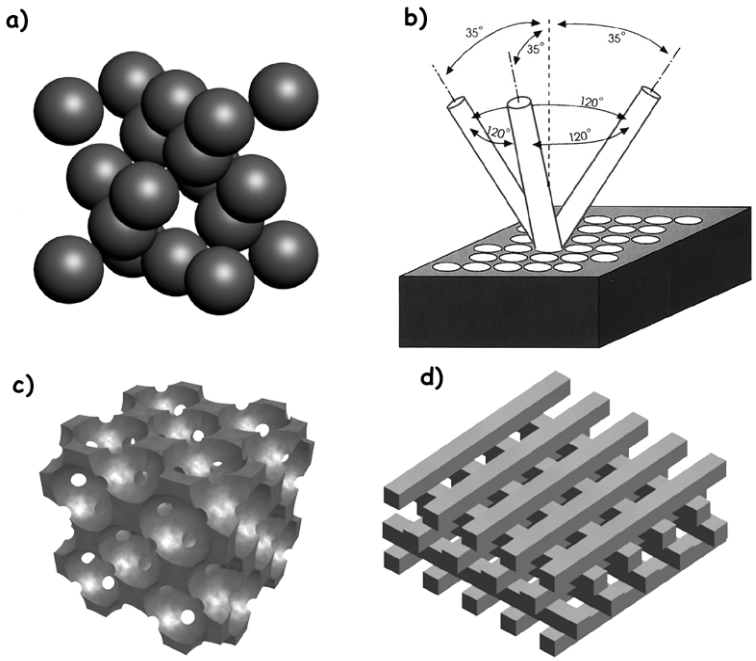

Fig. 1.21: Structures that should present a cPBG. a) diamond lattice, b) Yablonovite (ref. 74), c) air spheres in an fcc lattice and d) layer-by-layer or woodpile structure (refs. 76, 77).

In 1995 Astratov *et al.*[78] decided to follow another approach based on colloidal particles self-assembly. Techniques to obtain artificial opals made of silica and polystyrene spheres were already known.[56] But for the first time they were regarded as potential photonic crystals. These structures formed an fcc packing with sub-micrometric periodicity. Artificial opals were a method that all research laboratories could afford and soon attracted the interest of many other groups. Furthermore, loading the opal voids with a high RI material and then etching away the opal template would result in a structure of air spheres in a dielectric material matrix. Such a structure was precisely the kind of crystal for which Sözüer *et al.*[53] had predicted a cPBG. In 1997 Velev *et al.*[54] succeeded to obtain the first inverse structure (inverse opal). The RI contrast was still to low to present a cPBG, but the race to obtain an inverse opal satisfying all the requirements had begun.

Apart from the experimental developments there was a new aspect in photonic crystals that attracted the attention of researchers: the highly dispersive nature of

bands. In 1996 Lin *et al.*[79] observed that photons were strongly dispersed in 2D crystals when their frequency was close to the band gap edges. Their explanation was given in terms of band curvature and non-linear dispersion. Two years later Kosaka *et al.*[12] showed experimental evidences of novel anomalous dispersion phenomena (including negative refraction). Their explanation was based on dispersion surfaces and group velocity instead.

1.4.4 From 1999 to date (2003).

In 1999 the first photonic crystal working in the NIR was presented by Fleming *et al.*[49] Again it was a four layer crystal following the layer-by-layer structure but the periodicity was reduced to match the NIR frequencies. One year later, Noda *et al.*[47] fabricated an eight layer crystal by the wafer fusion method. Additionally they introduced a controlled defect in their crystals (specifically a 90º bend).

The researchers working with opals were finding two main problems. Firstly, the RI of the material to infill the pores had to be very high (>2.8) and secondly, they also had to be transparent at the desired optical regime. The number of materials accomplishing both requirements is not very large. Germanium and silicon were two candidates for the NIR. However these materials needed an opal template made of silica spheres with a size too large for self-assembly techniques (see Chapter III). In 1999 the first artificial opals with the appropriated periodicity were obtained[80] and in May of 2000 an inverse opal of silicon was presented by Blanco *et al.*[57]

Photonic crystals accomplishing all the requirements to present a cPBG in the NIR had been obtained both with opal-based and lithographic techniques. This range covered the very important wavelength of 1.55 microns which is an optical communication window since silica has a local minimum of absorption. However the existence of a cPBG still lacks a complete experimental demonstration. Indeed, to be able to state its existence all directions should be probed to reconstruct the photonic band structure.[81]

Many research fronts are open and advances are quickly achieved. A general review can be found in reference 82. Some of the current research aims are:

- New techniques to fabricate photonic crystals have been developed, among which, holographic lithography[59] seems very promising and it is quickly spreading.
- Crystal quality improvement to avoid unwanted defects.[83]
- The introduction of controlled defects to create guides or resonant cavities in 3D photonic crystals.[84]
- The search for photonic crystals operating at visible frequencies.[50,85]
- Fabrication of photonic crystals with metallic components.[25,86]
- The design of new structures and topologies[87,88] with cPBGs or interesting features such as highly dispersive bands or frequencies ranges in which light is negatively refracted at all angles.[13]

- Study of the effects of materials with interesting physical/chemical properties in photonic crystals.

1.5 References.

1 Ashcroft, N. W. & Mermin N. D. Solid State Physics (Saunders College, Philadelphia 1976).

2 Kittel, C. Solid State Physics (John Wiley & Sons, New York 1986).

3 All the photonic band structures presented in this chapter have been calculated thanks to the code developed by S. Guo for *MatLab* 6.5. The code is available at: http://www.lions.odu.edu/~sguox002/.

4 This calculation has been done with the Translight freeware developed by A. Reynolds which can be downloaded at: http://wwww.elec.gla.ac.uk/~areynolds.

5 Sakoda, K. Optical Properties of Photonic Crystals (Springer-Verlag Berlin Heidelberg 2001).

6 Joannopoulos, J. D., Villeneuve, P. R. & Fan, S. H. Photonic crystals: Putting a new twist on light. *Nature* **386**, 143 (1997).

7 Hetch, E. & Zajac, A. Optics (Addison-Wesley 1974).

8 Kosaka, H. *et al.* Self-collimating phenomena in photonic crystals. *Appl. Phys. Lett.* **74**, 1212 (1999).

9 Notomi, M. Negative refraction in photonic crystals. *Opt. Quantum Electron.* **34**, 133 (2002).

10 Yablonovitch, E. Inhibited Spontaneous Emission in Solid-State Physics and Electronics. *Phys. Rev. Lett.* **58**, 2059 (1987).

11 John, S. Strong Localization of Photons in Certain Disordered Dielectric Superlattices. *Phys. Rev. Lett.* **58**, 2486 (1987).

12 Kosaka, H. *et al.* Superprism phenomena in photonic crystals. *Phys. Rev. B* **58**, R10096 (1998).

13 Luo, C. Y., Johnson, S. G. & Joannopoulos, J. D. All-angle negative refraction in a three-dimensionally periodic photonic crystal. *Appl. Phys. Lett.* **81**, 2352 (2002).

14 Pendry, J. B. Negative refraction makes a perfect lens. *Phys. Rev. Lett.* **85**, 3966 (2000).

15 Veselago, V. G. Electrodynamics of Substances with Simultaneously Negative Values of Sigma and Mu. *Soviet Physics Uspekhi-Ussr* **10**, 509 (1968).

16 Mekis, A. *et al.* High transmission through sharp bends in photonic crystal waveguides. *Phys. Rev. Lett.* **77**, 3787 (1996).

17 Fan, S. H., Villeneuve, P. R. & Joannopoulos, J. D. Channel drop tunneling through localized states. *Phys. Rev. Lett.* **80**, 960 (1998).

18 Johnson, S. G. *et al.* Elimination of cross talk in waveguide intersections. *Opt. Lett.* **23**, 1855 (1998).

19 Fan, S. H., Johnson, S. G., Joannopoulos, J. D., Manolatou, C. & Haus, H. A. Waveguide branches in photonic crystals. *J. Opt. Soc. Am. B-Opt. Phys.* **18**, 162 (2001).

20 John, S. & Quang, T. Collective switching and inversion without fluctuation of two-level atoms in confined photonic systems. *Phys. Rev. Lett.* **78**, 1888 (1997).

21 Luo, C., Johnson, S. G., Joannopoulos, J. D. & Pendry, J. B. All-angle negative refraction without negative effective index. *Phys. Rev. B* **65**, 201104-1 (2002).

22 Ibanescu, M., Fink, Y., Fan, S., Thomas, E. L. & Joannopoulos, J. D. An all-dielectric coaxial waveguide. *Science* **289**, 415 (2000).

23 Fink, Y. *et al.* A dielectric omnidirectional reflector. *Science* **282**, 1679 (1998).

24 Cregan, R. F. *et al.* Single-mode photonic band gap guidance of light in air. *Science* **285**, 1537 (1999).

25 Fleming, J. G., Lin, S. Y., El-Kady, I., Biswas, R. & Ho, K. M. All-metallic three-dimensional photonic crystals with a large infrared bandgap. *Nature* **417**, 52 (2002).

26 Sakoda, K., Ohtaka, K. & Ueta, T. Low-threshold laser oscillation due to group-velocity anomaly peculiar to two- and three-dimensional photonic crystals. *Opt. Express* **4**, U1 (1999).

27 Cheng S. D. *et al.* Optimized dipole antennas on photonic band gap crystals. *Appl. Phys. Lett.* **67**, 3399 (1995).

28 Joannopoulos, J. D., Meade R. D. & Winn, J. N. Photonic Crystals. Molding the flow of light, (Princeton University Press 1995).

29 Busch, K. Photonic band structure theory: assessment and perspectives. *C. R. Phys.* **3**, 53 (2002).

30 Korringa, J. On the Calculation of the Energy of a Bloch Wave in a Metal. *Physica* **13**, 392 (1947).

31 Kohn, W. & Rostoker, N. Solution of the Schrodinger Equation in Periodic Lattices with an Application to Metallic Lithium. *Physical Review* **94**, 1111 (1954).

32 Modinos, A., Stefanou, N. & Yannopapas, V. Applications of the layer-KKR method to photonic crystals. *Opt. Express* **8**, 197 (2001).

33 Ohtaka, K. Energy-Band of Photons and Low-Energy Photon Diffraction. *Phys. Rev. B* **19**, 5057 (1979).

34 Stefanou, N., Karathanos, V. & Modinos, A. Scattering of Electromagnetic-Waves by Periodic Structures. *J. Phys.-Condes. Matter* **4**, 7389 (1992).

35 Wang, X. D., Zhang, X. G., Yu, Q. L. & Harmon, B. N. Multiple-Scattering Theory for Electromagnetic-Waves. *Phys. Rev. B* **47**, 4161 (1993).

36 Pendry, J. B. & Mackinnon, A. Calculation of Photon Dispersion-Relations. *Phys. Rev. Lett.* **69**, 2772 (1992).

37 Chan, C. T., Yu, Q. L. & Ho, K. M. Order-N Spectral Method for Electromagnetic-Waves. *Phys. Rev. B* **51**, 16635 (1995).

38 Sakoda, K. & Kawamata, J. Novel approach to photonic bands with frequency-dependent dielectric constants. *Opt. Express* **3**, 12 (1998).

39 Sakoda, K. & Shiroma, H. Numerical method for localized defect modes in photonic lattices. *Phys. Rev. B* **56**, 4830 (1997).

40 Fink, Y., Urbas, A. M., Bawendi, M. G., Joannopoulos, J. D. & Thomas, E. L. Block copolymers as photonic bandgap materials. *J. Lightwave Technol.* **17**, 1963 (1999).

41 Urbas, A. *et al.* Tunable block copolymer/homopolymer photonic crystals. *Adv. Mater.* **12**, 812 (2000).

42 Chelnokov, A., Wang, K., Rowson, S., Garoche, P. & Lourtioz, J. M. Near-infrared Yablonovite-like photonic crystals by focused-ion-beam etching of macroporous silicon. *Appl. Phys. Lett.* **77**, 2943 (2000).

43 Toader, O. & John, S. Proposed square spiral microfabrication architecture for large three-dimensional photonic band gap crystals. *Science* **292**, 1133 (2001).

44 García-Santamaría, F. *et al.* Nanorobotic manipulation of microspheres for on-chip diamond architectures. *Adv. Mater.* **14**, 1144 (2002).

45 Aoki, K. *et al.* Microassembly of semiconductor three-dimensional photonic crystals. *Nat. Mater.* **2**, 117 (2003).

46 Yamamoto, N., Noda, S. & Chutinan, A. Development of One Period of a Three-Dimensional Photonic Crystal in the 5-10 μm Wavelength Region by Wafer Fusion and Laser Beam Diffraction Pattern Observation Techniques. *Jpn. J. Appl. Phys.* **37**, L1052 (1998).

47 Noda, S., Tomoda, K., Yamamoto, N. & Chutinan, A. Full three-dimensional photonic bandgap crystals at near- infrared wavelengths. *Science* **289**, 604 (2000).

48 Lin, S. Y. *et al.* A three-dimensional photonic crystal operating at infrared wavelengths. *Nature* **394**, 251 (1998).

49 Fleming, J. G. & Lin, S. Y. Three-dimensional photonic crystal with a stop band from 1.35 to 1.95 microns. *Opt. Lett.* **24**, 49 (1999).

50 Juarez, B. H., Ibisate, M., Palacios, J. M. & Lopez, C. High-energy photonic bandgap in Sb2S3 inverse opals by sulfidation processing. *Adv. Mater.* **15**, 319 (2003).

51 Noda, S., Yamamoto, N. & Sasaki, A. New realization method for three-dimensional photonic crystal in optical wavelength region. *Jpn. J. Appl. Phys.* **35**, L909 (1996).

52 Yamamoto, N. & Noda, S. 100-nm-scale alignment using laser beam diffraction pattern observation techniques and wafer fusion for realizing three- dimensional photonic crystal structure. *Jpn. J. Appl. Phys.* **37**, 3334 (1998).

53 Sözüer, H. S., Haus, J. W. & Inguva, R. Photonic Bands - Convergence Problems with the Plane-Wave Method. *Phys. Rev. B* **45**, 13962 (1992).

54 Velev, O. D., Jede, T. A., Lobo, R. F. & Lenhoff, A. M. Porous silica via colloidal crystallization. *Nature* **389**, 447 (1997).

55 Zakhidov, A. A. *et al.* Carbon structures with three-dimensional periodicity at optical wavelengths. *Science* **282**, 897 (1998).

56 Philipse, A. P. Solid Opaline Packings of Colloidal Silica Spheres. *J. Mater. Sci. Lett.* **8**, 1371 (1989).

57 Blanco, A. *et al.* Large-scale synthesis of a silicon photonic crystal with a complete three-dimensional bandgap near 1.5 micrometres. *Nature* **405**, 437 (2000).

58 Berger, V., GauthierLafaye, O. & Costard, E. Photonic band gaps and holography. *J. Appl. Phys.* **82**, 60 (1997).

59 Campbell, M., Sharp, D. N., Harrison, M. T., Denning, R. G. & Turberfield, A. J. Fabrication of photonic crystals for the visible spectrum by holographic lithography. *Nature* **404**, 53 (2000).

60 Lee, K. Y. *et al.* Micromachining applications of a high resolution ultrathick photoresist. *J. Vac. Sci. Technol. B* **13**, 3012 (1995).

61 Miklyaev, Y. V. *et al.* Three-dimensional face-centered-cubic photonic crystal templates by laser holography: fabrication, optical characterization, and band-structure calculations. *Appl. Phys. Lett.* **82**, 1284 (2003).

62 Hiltner, P. A. & Krieger, I. M. Diffraction of Light by Ordered Suspensions. *J. Phys. Chem.* **73**, 2386 (1969).

63 Web of Sicence database. http://wos1.isiknowledge.com.

64 Anderson, P. W. Absence of Diffusion in Certain Random Lattices. *Physical Review* **109**, 1492 (1958).

65 John, S. & Rangarajan, R. Optimal Structures for Classical Wave Localization - an Alternative to the Ioffe-Regel Criterion. *Phys. Rev. B* **38**, 10101 (1988).

66 Yablonovitch, E. & Gmitter, T. J. Photonic Band-Structure - the Face-Centered-Cubic Case. *Phys. Rev. Lett.* **63**, 1950 (1989).

67 Callaway, J. Quantum theory of the solid state, Part A (Academic, New York, 1974), Appendix C.

68 Satpathy, S., Zhang, Z. & Salehpour, M. R. Theory of Photon Bands in 3-Dimensional Periodic Dielectric Structures. *Phys. Rev. Lett.* **64**, 1239 (1990).

69 Leung, K. M. & Liu, Y. F. Photon Band Structures - the Plane-Wave Method. *Phys. Rev. B* **41**, 10188 (1990).

70 Leung, K. M. & Liu, Y. F. Full Vector Wave Calculation of Photonic Band Structures in Face-Centered-Cubic Dielectric Media. *Phys. Rev. Lett.* **65**, 2646 (1990).

71 Zhang, Z. & Satpathy, S. Electromagnetic-Wave Propagation in Periodic Structures - Bloch Wave Solution of Maxwell Equations. *Phys. Rev. Lett.* **65**, 2650 (1990).

72 Maddox, J. Photonic Band-Gaps Bite the Dust. *Nature* **348**, 481 (1990).

73 Ho, K. M., Chan, C. T. & Soukoulis, C. M. Existence of a Photonic Gap in Periodic Dielectric Structures. *Phys. Rev. Lett.* **65**, 3152 (1990).

74 Yablonovitch, E., Gmitter, T. J. & Leung, K. M. Photonic Band-Structure - the Face-Centered-Cubic Case Employing Nonspherical Atoms. *Phys. Rev. Lett.* **67**, 2295 (1991).

75 Yablonovitch, E. & Leung, K. M. Hope for Photonic Bandgaps. *Nature* **351**, 278 (1991).

76 Sözüer, H. S. & Dowling, J. P. Photonic Band Calculations for Woodpile Structures. *J. Mod. Opt.* **41**, 231 (1994).

77 Ho, K. M., Chan, C. T., Soukoulis, C. M., Biswas, R. & Sigalas, M. Photonic Band-Gaps in 3-Dimensions - New Layer-by-Layer Periodic Structures. *Solid State Commun.* **89**, 413 (1994).

78 Astratov, V. N. *et al.* Optical spectroscopy of opal matrices with CdS embedded in its pores: Quantum confinement and photonic band gap effects. *Nuovo Cimento* **17**, 1349 (1995).

79 Lin, S. Y., Hietala, V. M., Wang, L. & Jones, E. D. Highly dispersive photonic band-gap prism. *Opt. Lett.* **21**, 1771 (1996).

80 Holgado, M. *et al.* Electrophoretic deposition to control artificial opal growth. *Langmuir* **15**, 4701 (1999).

81 Megens, M., Wijnhoven, J., Lagendijk, A. & Vos, W. L. Light sources inside photonic crystals. *J. Opt. Soc. Am. B-Opt. Phys.* **16**, 1403 (1999).

82 López, C. Some material aspects of photonic crystals. *Adv. Mater.* In press. (2003).

83 Jiang, P., Bertone, J. F., Hwang, K. S. & Colvin, V. L. Single-crystal colloidal multilayers of controlled thickness. *Chem. Mat.* **11**, 2132 (1999).

84 Lee, W. M., Pruzinsky, S. A. & Braun, P. V. Multi-photon polymerization of waveguide structures within three-dimensional photonic crystals. *Adv. Mater.* **14**, 271 (2002).

85 Lee, Y. C., Kuo, T. J., Hsu, C. J., Su, Y. W. & Chen, C. C. Fabrication of 3D macroporous structures of II-VI and III-V semiconductors using electrochemical deposition. *Langmuir* **18**, 9942 (2002).

86 Moroz, A. Three-dimensional complete photonic-band-gap structures in the visible. *Phys. Rev. Lett.* **83**, 5274 (1999).

87 Garcia-Santamaria, F., Ibisate, M., Rodriguez, I., Meseguer, F. & Lopez, C. Photonic band engineering in opals by growth of Si/Ge multilayer shells. *Adv. Mater.* **15**, 788 (2003).

88 Fenollosa, R. & Meseguer, F. Non-Close-Packed Artificial Opals. *Adv. Mater.* **15**, 1282 (2003).

Chapter 2: Silica microspheres study at different calcination temperatures.

2.1 Introduction.

The work by Stöber *et al.*[1] showed that hydrolysis of silicon alkoxides leads to the precipitation of very monodisperse silica microspheres. This work presented the starting point for an extensive research[2,3] which indirectly contributed to the, currently, most widespread method to fabricate photonic crystals with micrometric periodicity.

As mentioned in the previous chapter, fabrication of photonic crystals obtained from artificial opals is one of the pillars of this dissertation. Specifically, artificial opals made of silica spheres. In this context, being able to fabricate spherical micrometric silica particles with a very narrow size distribution is tremendously important since they will constitute the fundamental building blocks of our photonic crystals.

In this chapter a detailed study of the refractive index (RI) variations of different diameter monodisperse silica spheres as a function of calcination temperature will be shown. The motivation is that opals usually must be subjected to thermal treatments like sintering[4,5] or guest material synthesis,[6] which often involves high temperatures.

The results of this work show that RI and diameter variations induced by temperature treatments are significant enough to be taken into account whenever optical properties of silica artificial opals are modeled. An explanation of this behavior is given in terms of porosity and the removal of hydration water.

2.2 Silica spheres synthesis.

In 1968 Stöber *et al.*[1] developed a method to synthesize colloidal silica microspheres (called SFB method, honoring creators' names). The procedure consists in hydrolyzing a silicon alkoxide $Si(OR)_4$, R being a radical with the general formula C_mH_{2m+1}. Subsequently, the hydrolyzed species are condensed forming siloxane groups (≡Si-O-Si≡). When reaction happens in a basic medium with a pH between 7 and 11, electrostatic repulsion causes monomers addition to already condensed species.[3] This way, aggregation is avoided and non-soluble particles are obtained as opposed to a sol-gel.

For silica microspheres used in this work, the precursor alkoxide is Tetraethyl ortosilicate (TEOS) and the hydrolyzing agent is doubly distilled water (DDW). Ammonia (NH_3) is used to catalyze the reaction and to obtain a basic medium. Finally, absolute ethanol is the common solvent in which reaction happens.

The hydrolysis velocity will be strongly related to spherical particles quality and diameter. This velocity will be proportional to $[NH_3]^{0.9}$:$[H_2O]^{1.5}$ ratio and temperature dependent.[7] For this reason, TEOS, and NH_3 concentrations are usually kept constant while $[H_2O]$ is varied to obtain different diameters. By means of this method, silica spheres with diameters ranging from 200 to 700 nm can be obtained with a narrow size distribution around 3-4%.

The SFB method allows obtaining spheres larger than 700 nm, however, the size distribution is much wider and the resulting particles cannot be used to fabricate artificial opals. Bogush *et al*.[8] developed a technique in which SFB prepared microspheres where used as seeds for a re-growth process. A slow aggregation of TEOS under controlled conditions to the colloidal suspension obtained by the SFB method allows increasing the diameter of the existing particles without any additional nucleation. Following this procedure the range of available microsphere diameters can be expanded up to 1400 nm.[9]

2.3 Refractive index of silica spheres.

This section shows the index matching (IM) method used to measure the RI of silica microspheres calcined at different temperatures. Using this technique, sample porosity is also demonstrated for certain calcination temperatures.

2.3.1 The index matching method.

The IM method consists in finding a solvent with known RI equal to that of the sample itself. When this happens the optical boundary between both dielectrics disappears and light scattering effects become negligible. This means that forward light scattering intensity will present a maximum when the RI of both materials matches. Therefore, sample RI can be deduced if we know that of the matching solvent. In this section, different solvent compositions have allowed to smoothly vary the medium RI while transmission measurements were performed *in-situ*.[10]

The mediums chosen for this study were mixtures of glycerin and water. Glycerin is an easy available, non-toxic and water miscible liquid with a RI of 1.47. This value exceeds that of pure amorphous silica (usually around 1.45) and water RI is below it. Consequently, mixtures of both liquids provide an appropriate range. **Fig. 2.1** shows the RI values as a function of glycerin volume concentration for a 589 nm wavelength. This corresponds to the yellow line of a sodium lamp (which is a standard). Values are obtained from ref. 11.

Experimental data can be fitted by a second order polynomial which will allow data interpolation for IM experiments:

$$n = 1.333 + 1.21 \cdot 10^{-1} A + 2.1 \cdot 10^{-2} A^2$$

where n is the solution RI and A is the glycerin vol. concentration.

The IM experiments were carried out as follows: the silica spheres were sonicated in a glycerin aqueous solution. While light transmission intensity was being measured, a known volume of silica-water from a reservoir was added with a micro-pipette. This way, glycerin concentration, and therefore medium RI, was always known. Since IM was determined through light transmission, the silica concentration in both the initial solution and water reservoir was kept constant at 0.5 % vol. Therefore variations in silica concentration did not affect light transmission values. A tungsten lamp was used as the light source, the adequate

wavelength was selected thanks to a monocromator and transmitted light detected by a gallium arsenide (GaAs) detector.

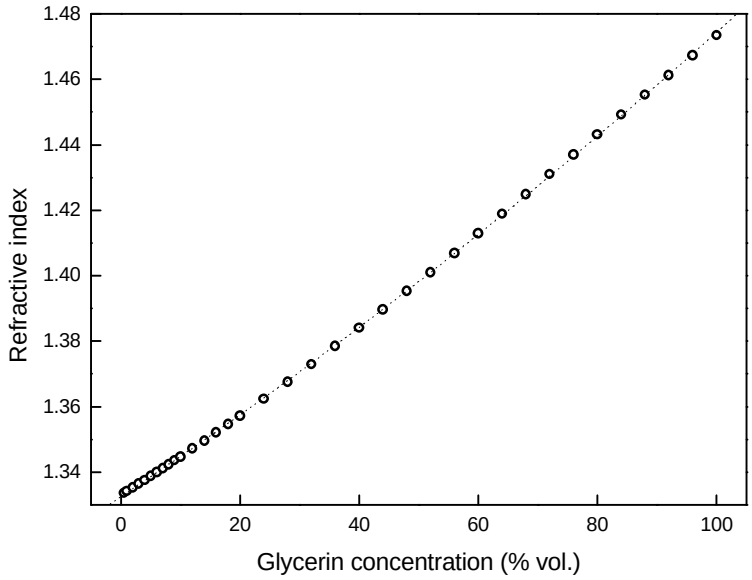

Fig. 2.1: Refractive index of glycerin aqueous solutions as a function of volume concentration.

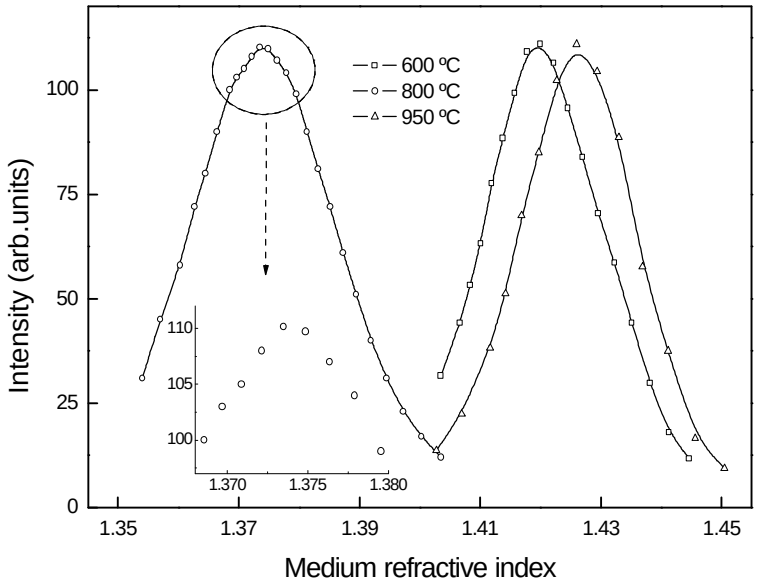

Fig. 2.2: Forward scattering intensity of 589 nm *em* radiation through a dispersion of 870 nm of diameter silica spheres as a function of medium refractive index. Each data-set corresponds to different calcination temperatures. When the medium refractive index matches that of the spheres, a maximum of intensity is achieved. Continuous lines are just eye-guides.

Fig. 2.2 shows examples of IM measurements for a sample made of 870 nm of diameter silica spheres that had been calcined at three different temperatures. As the medium RI gets closer to that of the silica sample, transmission intensity increases. Once it is matched there is a maximum of light transmission. Moving away from the IM situation entails a transmission intensity decrease.

2.3.2 Calcination temperature effects on silica spheres refractive index.

Five samples of spheres of different diameters were prepared: 379, 575, 800, 870 and 1175 nm. Each batch was divided in eleven parts of 100 mg of sample and calcined at eleven temperatures in the following manner: the samples were heated at 70 ºC for three hours, then the temperature was increased (1 degree per minute) up to the desired point and maintained for three hours, finally it was decreased down to room temperature (10 degrees per minute).

The RI of each sample was analyzed by means of the IM method. **Fig. 2.3** shows the results for spheres with diameters of 575, 800 and 1175 nm. The first sample was fabricated by a simple SFB method; the other two samples followed the re-grown procedure mentioned in previous section.

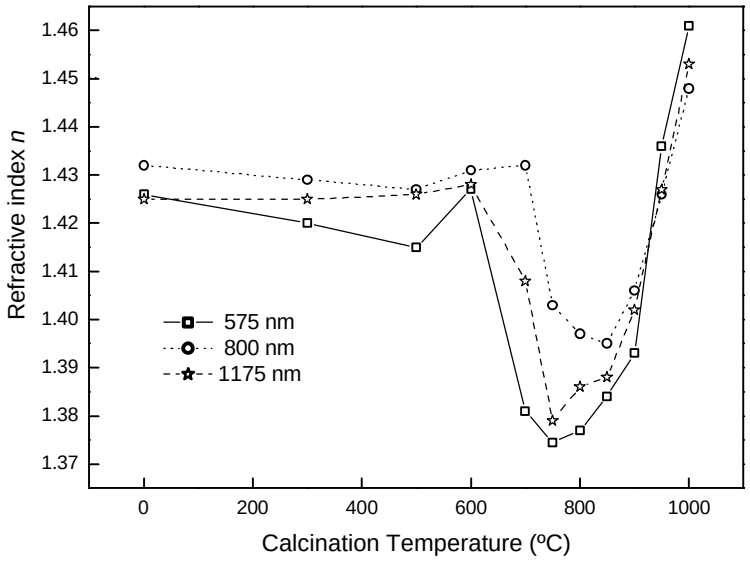

Fig. 2.3: Refractive index of Stöber SiO_2 samples as a function of calcination temperature. Data for three samples of different diameter silica spheres is presented. 575 nm spheres were prepared in a simple SFB process while 800 and 1175 nm spheres followed a regrowth procedure.

Data in **Fig. 2.3** together with other results not presented here show that the behavior is similar regardless of sphere diameter. For this reason the average refractive index for each calcination temperature from all samples is calculated and shown in **Fig. 2.4** along with its standard deviation. The results of IM characterization did not show any important dependence of RI on synthesis methods and data variations seem to be related to small deviations in sample

production. However, calcination temperature dependence is clear. Roughly speaking the RI is constant up to 600 ºC (region I), then it drastically decreases until 800 ºC are reached (region II). Finally, RI increases when temperature is augmented (region III).

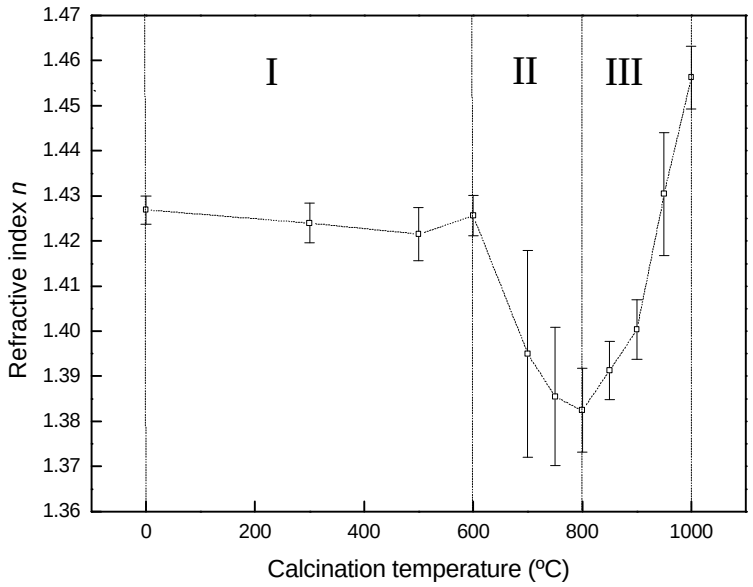

Fig. 2.4: Average refractive index of Stöber SiO_2 samples as a function of calcination temperature. The error bars represent one standard deviation with five determinations. The graph is divided in three regions depending on refractive index behavior.

It was noticed that samples calcined at temperatures around 750 ºC had a RI that changed depending on the time they had been soaked in water before measurements. This could be only explained if samples were porous and pores were being infiltrated with water. Indeed air substitution for water would increase the sphere average RI. A sample which showed its minimum refractive index when calcined at 750 ºC was soaked in DDW for different periods of time before its refractive index was measured. The results displayed in **Fig. 2.5** show that water enters into the spheres pores.

The following equation where the second term is a time dependent exponential decay fits the experimental data:

$$n(t) = n_f - (n_f - n_i)\, e^{-t/t}$$

here n_f is the final refractive index, that is, the saturating value, n_i is the initial refractive index when no water has entered the sphere, t is the time in hours and t is the life-time of the process. The lifetime obtained is 210 hours. Such a high value can be understood if we take into consideration that most of the pores are inside the sphere while its outermost volume remains almost poreless.[12] Refractive indexes obtained from this graph lead to porosity of 25%. This porosity is obtained by calculating the average dielectric constant. The possibility of rehydration

instead of water filling was discarded since the initial RI recovered by heating the sample again just at 200 ºC.

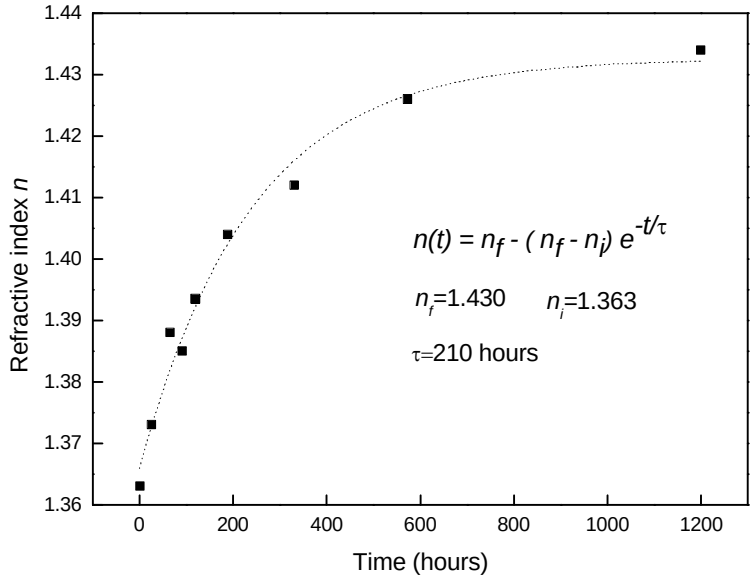

Fig. 2.5: Refractive index variation of a 575 nm diameter sample as a function of time due to water uptake by the pores. Dotted line represents the fit of experimental data to an asymptotic growth.

2.4 Infrared absorption.

Ideally, after sample synthesis all oxygen atoms act as bridges that bond silicon atoms (siloxane groups). However, in fact, many of these bonds are not completed and oxygen atoms form hydroxyl-group: ≡Si-OH. These groups act as dipoles that attract other polar molecules such as H_2O. When silica samples are calcined, hydrogen atoms can be eliminated if temperature is high enough. The reaction products are water molecules and new siloxane groups. Depending on the silanol group situation (isolated, neighboring, internal, external…) the vibration frequency of atoms bonds varies and therefore the energy of the *em* radiation that they absorb. For this reason, *em* absorption can be used to identify the presence of silanol groups.

In order to characterize the water content, Infra Red (IR) reflectance spectra were performed focusing our attention on two principal features: absorption at 3750 cm^{-1} corresponding to isolated silanol groups and water absorption below 3720 cm^{-1}.[13,14] This was performed with a Bruker IFS 66/S Fourier Transform IR spectrometer and 20 mg of dried (at 70 ºC for 3 hours) sample. **Fig. 2.6** shows the reflectance spectra obtained for a sample calcined at 10 different temperatures. It can be seen that up to 600 ºC (region I) there are not significant changes. Conversely, in region II, it can be observed that absorption due to water decreases as temperature increases. This happens because water molecules that are bound to

silanol groups are being removed. This entails the apparition of isolated silanol groups as the absorption dip at 3750 cm^{-1} shows. The intensity of this dip increases until 900 ºC (in region III). For higher temperatures silanols are broken and form siloxane groups. At 1000 ºC the presence of isolated silanols is hardly detected.

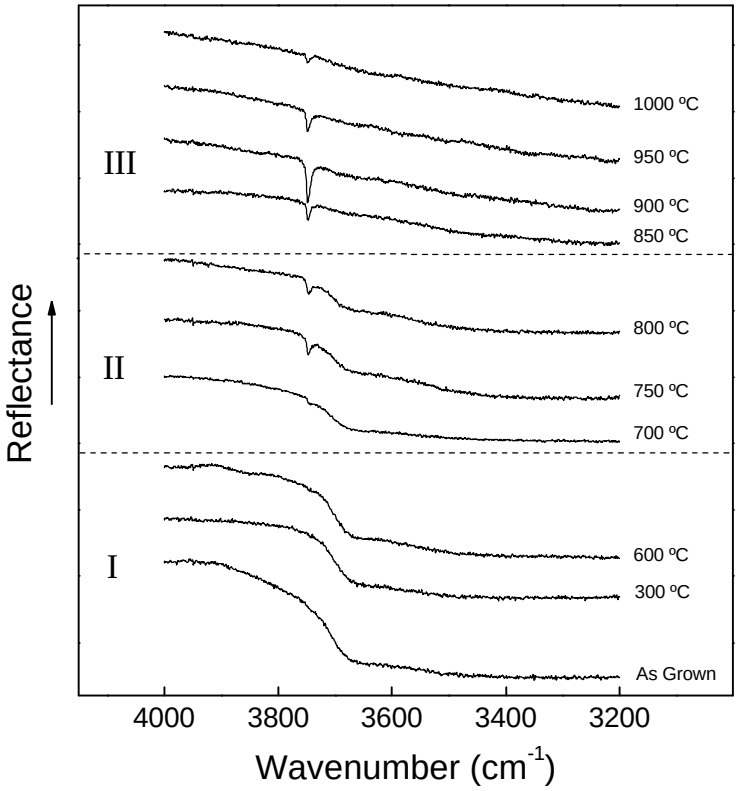

Fig. 2.6: IR spectra from a calcined silica sample with a diameter of 575 nm. See absorption band at 3750 cm^{-1} from isolated silanol groups and the wide absorption band of water onset at 3700 cm^{-1}.

As a complementary study, sample mobility measurements were performed for calcination temperatures up to 900 ºC (samples calcined at higher temperatures could not be dispersed in water as they sintered). As explained before, the silanol groups are responsible for forming dipoles. For this reason, a suspension of silica microspheres in water will be sensitive to electric fields. If spheres are negatively charged (which is the usual situation unless electrolytes are added or pH modified) they will move towards a positively charged electrode. The ratio between particle velocity (**v**) and electric field (**E**) intensity is called mobility (m). In the case of silica microspheres mobility is expected to be larger if the number of external silanol groups is higher.

The results obtained were around 4.5 μm·cm/V·s in all cases and no significant variations were observed. This is in agreement with IR absorption measurements since silanol groups do not collapse for temperatures under 900 ºC.

2.5 Porosimetry.

Results shown in section **2.3.2** reveal the presence of pores, at least for samples calcined at certain temperatures. However whether these pores are formed during the microsphere synthesis or the calcinations process is still unanswered. The later possibility has been observed in some oxides.[15]

Depending on their size, pores in solids are divided in three groups. Each group requires a specific method for their detection:

- Macropores: Diameter above 50 nm. Method: mercury porosimetry.
- Mesopores: Diameter between 50 and 2 nm. Method: adsorption porosimetry.
- Micropores: Diameter under 2 nm. Method: X-rays and adsorption porosimetry.

Calcination Temperature	**Specific surface a_s**
300 ºC	9.1 m^2/g
600 ºC	12.6 m^2/g
700 ºC	11.9 m^2/g
800 ºC	13.7 m^2/g

Table 2-1: Specific surface area for different calcination temperatures.

The main result from porosimetry experiments is the specific surface area a_s. This is the surface area per mass unit. The more porous the sample is the larger specific surface is obtained. For an ideal pore-less sphere the specific surface area is simply $a_s=6/rd$ (where r is silica density, 2.05 g/cm^3, and d is the sphere diameter). An 875 nm of diameter silica spheres sample was chosen for adsorption and mercury porosimetry. If these spheres were pore-less their specific surface area would be 3.4 m^2/g. Mercury porosimetry detected the interstices between spheres but did not show the presence of surface or internal macropores. Liquid nitrogen adsorption porosimetry was performed for the following calcinations temperatures: 300 ºC, 600 ºC, 700 ºC and 800 ºC. Prior to adsorption, samples were heated at 120 ºC under high vacuum (10^{-6} Torr) for 16 hours. Specific surface area results are shown in **Table 2-1**.

Although values in **Table 2-1** are larger than those of a poreless sphere, they are still very low in comparison to a typical porous material. For example, the specific surface area is around 750 m^2/g for momtmorillonite, a laminar silicate. The obtained results are probably due to sphere roughness and not to porosity.

A possible explanation for the inability of these methods to detect pores is that they are mainly internal pores and are not easily accessible by non-polar molecules. This seems to agree with other researchers results.[12]

2.6 Sphere diameter variations with calcination temperature.

In previous sections it was shown that silica microspheres RI increases for calcination temperatures above 750-800 ºC. This fact could be explained if there was a sphere contraction. Pores would collapse at this temperatures leading to a sphere purely made of amorphous silica with a higher RI and a smaller diameter.

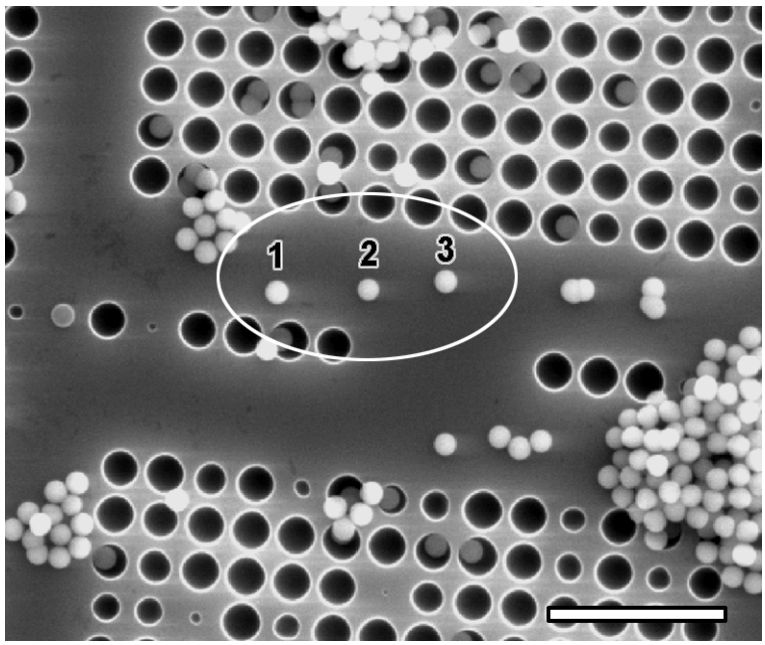

Fig. 2.7: SEM image spheres selected to be measured before and after calcination. Silica spheres have been randomly deposited on the substrate and three specific spheres well apart from each. Scale bar is 5 microns.

Spheres having a 25% of their volume occupied by air pores should show a significant diameter decrease if pores were removed. Final sphere diameter would be around 90% of the initial diameter if this model were true. Such a variation can be easily detected with a Scanning Electron Microscope (SEM) when sphere diameters are above 500 nm. Transmission Electron Microscopy (TEM) would be a better technique to detect small size variations. However SEM allowed using templated substrates that could be heated up to 950 ºC and, therefore, locating specific spheres. Silica suspensions in water with a 0.05% solid content were prepared and a drop was carefully deposited on the substrate and dried. **Fig. 2.7** shows an example of a templated silicon substrate with the silica sample. Three spheres well apart from each other are selected and measured before and after calcination.

Following this method several spheres of different diameters were measured before and after calcinations at 750 ºC and 950 ºC. Results are shown in **Fig. 2.8**. From values fitting it can be calculated that calcination at 750 ºC causes an average decrease of 97% ± 3% of the original diameter, which is almost a negligible but systematic effect. However, for a calcination temperature of 950 ºC, the average diameter decreases to 89% ± 3%. This variation is in excellent agreement with the expected value and supports the pore collapse model to explain the RI increase from 750 ºC to 1000 ºC shown in **Fig. 2.4**.

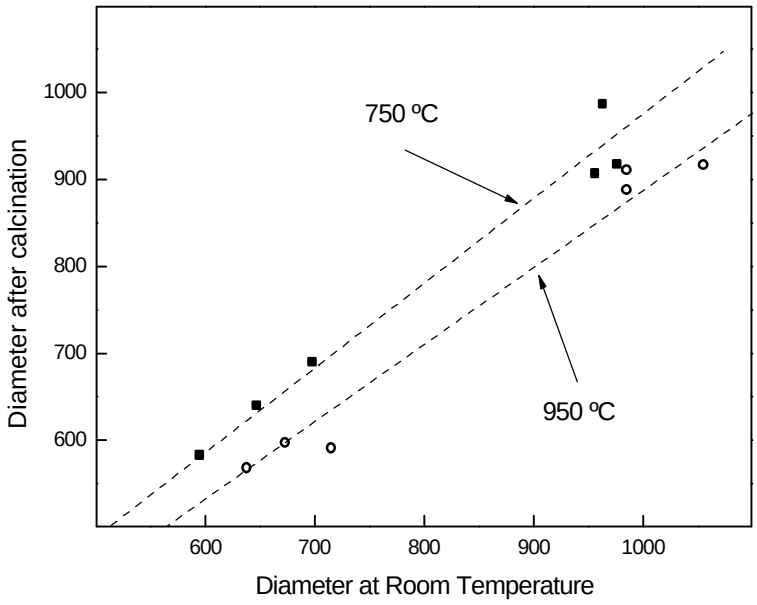

Fig. 2.8: Diameter variation for six samples from room temperature to 750 ºC (solid squares) and 950 ºC (hollow circles).

2.7 Summary.

In this chapter the refractive index behavior of silica spheres with calcination temperature (from room temperature to 1000 ºC) has been characterized. A strong dependence was observed between 600 ºC and 1000 ºC that can be assigned to pore formation and water removal. Although nitrogen and mercury porosimetry have not shown the presence of pores, their existence has been demonstrated by filling the silica spheres with DDW and by checking their compaction when calcined above 750 ºC.

In a previously published experiment,[5] optical properties of structures made of silica spheres were studied for different calcinations temperatures. In that work they did not find a fully satisfactory explanation to the diffraction peak shift when temperatures around 600 ºC were exceeded. Thanks to results obtained in this chapter for the refractive index behavior the optical properties of those structures can now be explained.[16]

2.7.1 Conclusions.

- An appropriate RI value for as-synthesized silica spheres is 1.425±0.005.
- Temperature treatments under 600 ºC hardly affect the silica spheres RI. When temperatures exceed this value their RI shows important variations that must be taken into account.
- The behavior of silica spheres RI versus calcination temperature does not seem to be dependent on sphere diameter or re-grown synthesis procedures.
- As-synthesized silica spheres present porosity typically around 25%. These pores can be accessed by water molecules.
- For temperatures above 750 ºC pores begin to collapse and sphere diameter significantly diminishes.

2.7.2 Future research.

Even though several agreements between this work and some published papers have been found, there are two points that apparently contradict results presented here. Thermogravimetric measurements done by Sacks *et al.*[13] showed water loss with calcination temperature mainly under 300 ºC. However, an important release of water should be observed between 600-800 ºC to explain the RI decrease. The same authors performed picnometry experiments showing a continuous increase of mass density with calcination temperature. Again, a decrease of this parameter should be observed between 600 and 800 ºC. These are two questions that would require further research.

Finally, although sphere diameter diminution from 750 to 950 ºC has been shown, TEM measurements could help to obtain a more accurate characterization of sphere size variations.

2.8 References.

1 Stöber, W., Fink, A. & Bohn, E. Controlled Growth of Monodisperse Silica Spheres in Micron Size Range. *J. Colloid Interface Sci.* **26**, 62 (1968).

2 van Helden, A. K., Jansen, J. W. & Vrij, A. Preparation and Characterization of Spherical Monodisperse Silica Dispersions in Non-Aqueous Solvents. *J. Colloid Interface Sci.* **81**, 354 (1981).

3 Iler, R. K. The Chemistry of Silica (John Wiley and Sons: New York, 1979).

4 Sacks, M. D. & Tseng, T. Y. Preparation of SiO_2 Glass from Model Powder Compacts 2. Sintering. *J. Am. Ceram. Soc.* **67**, 532 (1984).

5 Míguez, H. *et al.* Control of the photonic crystal properties of fcc-packed submicrometer SiO_2 spheres by sintering. *Adv. Mater.* **10**, 480 (1998).

6 Blanco, A. *et al.* Large-scale synthesis of a silicon photonic crystal with a complete three-dimensional bandgap near 1.5 micrometres. *Nature* **405**, 437 (2000).

7 Harris, M. T., Brunson, R. R. & Byers, C. H. The Base-Catalyzed-Hydrolysis and Condensation-Reactions of Dilute and Concentrated TEOS Solutions. *J. Non-Cryst. Solids* **121**, 397 (1990).

8 Bogush, G. H., Tracy, M. A. & Zukoski, C. F. Preparation of Monodisperse Silica Particles - Control of Size and Mass Fraction. *J. Non-Cryst. Solids* **104**, 95 (1988).

9 Ibisate M. Cristales fotónicos basados en ópalos. (PhD. thesis, Universidad Autónoma de Madrid, 2003).

10 van Blaaderen, A. & Vrij, A. Synthesis and Characterization of Monodisperse Colloidal Organo-Silica Spheres. *J. Colloid Interface Sci.* **156**, 1 (1993).

11 Wolf, A. V.; Brown, M. G.; Prentiss, P. G. Handbook of Chemistry and Physics, 57^{th}, p D-218 (CRC Press: Boca Raton, FL, 1976).

12 Vrij, A. *et al.* Light-Scattering of Colloidal Dispersions in Non-Polar Solvents at Finite-Concentrations - Silica Spheres as Model Particles for Hard-Sphere Interactions. *Faraday Discuss.*, 19 (1983).

13 Sacks, M. D. & Tseng, T. Y. Preparation of SiO_2 Glass from Model Powder Compacts 1. Formation and Characterization of Powders, Suspensions, and Green Compacts. *J. Am. Ceram. Soc.* **67**, 526 (1984).

14 Míguez, H. Los ópalos artificiales como cristales fotónicos. (PhD. thesis, Universidad Autónoma de Madrid, 2000).

15 Wilson, S. J. & Stacey, M. H. The Porosity of Aluminum-Oxide Phases Derived from Well-Crystallized Boehmite-Correlated Electron-Microscope, Adsorption, and Porosimetry Studies. *J. Colloid Interface Sci.* **82**, 507 (1981).

16 García-Santamaría, F., Míguez, H., Ibisate, M., Meseguer, F. & López, C. Refractive index properties of calcined silica submicrometer spheres. *Langmuir* **18**, 1942 (2002).

Chapter 3: Artificial opal fabrication methods.

3.1 Introduction.

In order to obtain photonic crystals working in the visible or near infrared range of the spectra, monodisperse building blocks in shape and size are needed. As periodicity for such crystals must be of the order of microns, the kind of particles used as building blocks are among those known as colloidal particles. Under certain conditions colloids may spontaneously form ordered lattices. This phenomenon is called self-assembly, an important subject of research since the beginning of the second half of the 20th century.

Nature provides some examples of colloidal particles forming crystals. In 1957 Williams *et al.*[1] found a crystallizable insect virus whose suspensions showed iridescences. The *Tipula Iridiscent* virus size is around 130 nm and forms a face centered cubic (fcc) close packing array in concentrated suspensions. The gemstones known as opals are another example. In 1964 Sanders[2] discovered that precious opals were formed by silica microspheres in a random stack of close-packed layers.[3] Darragh *et al.*[4] suggested that formation of opals could be based on the precipitation of silica and a posterior aggregation of the spherical particles to make the opaline structure. Only two years later (1968) Stöber *et al.*[5] showed a method to synthesize silica colloidal microspheres (see Chapter 2). However, it was not until 1989 that Philipse[6] fabricated the first solid packings of colloidal silica spheres, in other words, artificial opals.

In the photonic crystals research field, artificial opals have been of paramount importance since Astratov *et al.*[7] published in 1995 an experimental work in which opals made of silica spheres were envisioned as templates valid as photonic crystals. The method to fabricate the opals they used was based on the natural sedimentation of silica spheres. Later on, a large effort has been put on improving the opal fabrication methods to obtain samples free of defects in short periods of time.

When this PhD Thesis begun in 1999, natural sedimentation in water was the most widespread method. However, this approach allows little control on opal characteristics and is not well suited to obtain crystalline sediments of silica spheres larger than 500 nm. In this chapter, a brief introduction to the crystallization mechanisms will be presented along with the description of the fabrication methods used to grow the opals shown in this dissertation. These methods will include the electrophoretically assisted sedimentation, by means of which silica spheres with diameters over 500 nm were self-assembled for the first time. A brief description of other crystallization methods is presented in Appendix IV for the sake of completeness.

3.2 Crystallization.

The crystallization of monodisperse colloidal suspensions of micrometer-sized spheres is still under extensive research. Systems with long-range repulsive potentials show a richness of phases which makes them quite complicated for their

understanding.[8] For that reason most of the theoretical models and experiments to explain the crystallization mechanisms have been performed with hard spheres where no interactions must be considered.

A suspension of hard spheres can be regarded as a non-ideal gas whose equation of state is:

$$\frac{PV}{Nk_BT} = 1 + B_2\left(\frac{N}{V}\right) + B_3\left(\frac{N}{V}\right)^2 + ... + B_n\left(\frac{N}{V}\right)^{n-1};$$

where P is the osmotic pressure, V is the system volume, N is the number of spheres, k_B is Boltzmann's constant, T is the temperature and B_n are the so called virial coefficients. It can be shown that in reality, the expression on the right can be expressed as a function of the spheres volume fraction (f). Therefore:

$$P = \frac{f}{V_{sp}} k_B T Z(f);$$

where N/V has been expressed as f/V_{sp}, this is, the sphere volume fraction divided by the sphere volume. Reduced osmotic pressure (Π) is the dimensionless value usually presented. To obtain it P is divided by P_0 which is the osmotic pressure the system would have for a close-packed configuration if the system were an ideal gas:

$$P_0 = \frac{f_{cp}}{V_{sp}} k_B T = \sqrt{2} k_B T d^{-3}; \quad \Pi = \frac{P}{P_0} = \frac{f}{f_{cp}} Z(f);$$

$f_{cp}=\pi/\sqrt{18}$ being the volume fraction of spheres for a close-packed array and d the sphere diameter.

Computer calculations performed by Alder *et al.*[9] showed that hard spheres systems should have a first order transition between a solid and a liquid phase. Several virial coefficients were calculated by Ree *et al.*[10] among others which led to approximate equations for the liquid and the solid phase. A valid equation for the former case is that of Carnahan-Starling:[11]

$$Z(f)_{liquid} = \frac{1 + f + f^2 - f^3}{(1-f)^3};$$

In the case of the solid equation, Hall's expression offers accurate results:

$$Z(f)_{solid} = \frac{1 + f + f^2 - 0.67825f^3 - f^4 - 0.5f^5 - 6.028e^{x(7.9-3.9x)}f^6}{1 - 3f + 3f^2 - 1.04305f^3}; \quad x = f_{cp} - f;$$

Hoover *at al.*[12] made a Monte Carlo determination of the pressure and absolute entropy to discover the density of the coexisting liquid and solid phases present in these systems. They found that the hard-sphere solid and fluid phases are in thermodynamic equilibrium of pressure and chemical potential over a density

interval from 0.494 to 0.545. The critical osmotic pressure for this coexistence region was calculated to be Π_c=8.27 (P_c=11.7·k_BT/d^3). The equations of state showing the solid, liquid and coexistence regions are shown in **Fig. 3.1**.

From all the results presented so far, a solid phase of hard spheres could be obtained if spheres are concentrated till the osmotic pressure value is higher than Π_c. However, a solid phase can be crystalline or glassy. If a crystalline solid phase is required, another condition must be fulfilled: the compression rate of spheres must not exceed the maximum crystallization rate. Intuitively this means that the velocity by which new spheres are added must be slow enough to allow the system to crystallize, otherwise an amorphous solid results. The maximum crystallization rate (g) is proportional to the self-diffusion coefficient of the spheres in the liquid divided by the sphere diameter: $g \propto k_BT/\eta d^2$, where η is the medium viscosity.[13] This relationship reveals that small spheres will crystallize faster and therefore allow a higher aggregation rate.

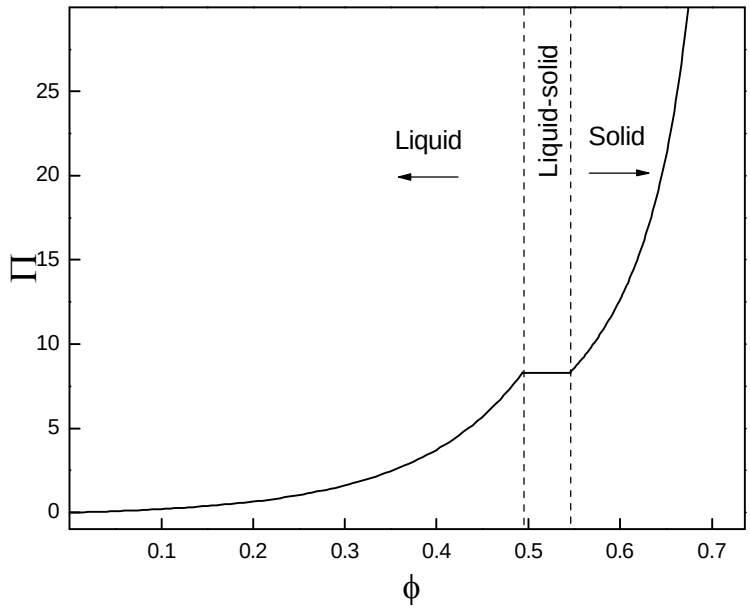

Fig. 3.1: Reduced osmotic pressure as a function of volume fraction of hard spheres. The liquid phase is represented by the Carnahan-Starling equation of state, while solid phase is given by Hall's equation. A solid-liquid coexistence region exists for the volume fraction regime 0.494<f<0.545 and a reduced osmotic pressure of 8.27.

The experimental confirmation of liquid to crystal (solid) phases over the density interval 0.494<f<0.545 was obtained for spheres of polystyrene (PS),[14] poly(methyl methacrylate) (PMMA)[15] and silica.[16] Attractive or repulsive potentials between spheres had to be cancelled to obtain an ideal system of hard spheres. In all cases the surface charge of the spheres was screened or eliminated by high ionic strengths or low dielectric constant mediums and the attractive van der Waals forces suppressed by a refractive index matching medium.

So far it has been said that crystallization occurs for close-packed arrays. However there are three possible structures with a close-packed volume fraction. Namely the hexagonal close packed array (hcp), the fcc lattice or a random stack of hexagonal layers. In 1997 Woodcock[17] demonstrated the fcc phase is the most stable thanks to a small entropy difference.

3.3 Natural sedimentation.

Natural sedimentation of silica spheres is probably the simplest method to fabricate artificial opals.[18] The silica spheres are just dispersed in an aqueous solution to obtain a diluted suspension (usually 0.5% volume) and allowed to settle down on a flat surface. Once sedimentation is completed, the supernatant is removed by evaporation at 45ºC and the opal sintered[19] to give it a higher mechanical strength.

Obviously sedimentation accomplishes the requirements stated on the previous section. Firstly, it offers a way to obtain a concentrated suspension where the volume fraction is high enough to begin crystallization. Secondly, provided a low enough sedimentation velocity and initial volume fraction, the aggregation of spheres will not be faster than the maximum crystallization rate. Although the surface charge of the spheres is not screened and therefore the system is not ideally composed of hard-spheres, the qualitative results obtained are comparable.

3.3.1 Sedimentation velocity.

Sedimentation velocity will be a very important parameter to control the growth of high quality artificial opals with this method. High velocity values may result in glassy sediments. The model of constant velocity particle packing is based on the interaction of gravitational ($F_g=1/6\pi r_s g d^3$), Archimedes buoyancy ($F_A=1/6\pi r_m g d^3$) and frictional ($F_f=3\pi h d U_0$) forces. Where r_s and r_m are the spheres and medium mass densities, g is the gravity acceleration and U_0 is the sphere velocity. When all forces are balanced, the Stokes law is obtained:

$$U_0 = \frac{d^2(r_s - r_m)g}{18h}$$

This easily obtained equation allows obtaining accurate results for dilute suspensions of spheres. However the actual velocity U of a particular sphere differs from U_0 owing to the hydrodynamic interaction between the various particles in the dispersion. The study of sedimentation has been quite extensive, in 1952 Kynch[20] stated that actual sedimentation velocity should have the form: $U=U_0(1-f)^b$ where b has an uncertain value ranging from 5 to 7.[21,22] A theoretical study done by Batchelor[23] showed that $U=U_0(1-6.55f)$ for low concentrations ($f<0.05$). In any case, for the particular case of natural sedimentation in which the volume fraction is typically around 0.005 the sedimentation velocity is *ca.* $0.97 \cdot U_0$, meaning that there is almost no hydrodynamic interaction since colloidal dispersion is very diluted. If sphere diameter is calculated from Stokes law for this diluted dispersion

without taking into account hydrodynamic interactions the value is underestimated only by a 1.5%. Since sphere polydispersity is usually around 5%, corrections for such diluted dispersions are negligible. In natural sedimentation experiments with silica spheres in water at room temperature: h =1.005 cP, r_s-r_m =1050 kg/m^3. For spheres with a diameter between 0.2 and 0.5 microns, sedimentation velocity ranges from 90 to 590 μm/h. As sedimentation tubes are about 6 cm high, the whole process may take from one month to 5 days. In the case of smaller spheres a good way of accelerating sedimentation is increasing the suspension temperature since water viscosity is very sensitive to this parameter. Indeed, water viscosity at 10ºC is 1.792 cP whereas at 40ºC viscosity decreases down to 0.656 cP. Unfortunately, higher temperatures are not advisable since convection forces may prevent the spheres from settling.

Natural sedimentation to obtain artificial opals is not exclusive for silica spheres, however, sedimentation times needed for PS or PMMA spheres is much longer since their density is very close to that of water. When sediments made of this kind of spheres are needed, centrifugation is used to assist the sedimentation.

3.3.2 The large spheres problem.

As mentioned in the introductory section, the natural sedimentation method is well suited to obtain solid opaline packings of silica spheres with a diameter smaller than 500 nm. The reason is that larger spheres sedimentation velocity (U) is too high and spheres aggregation occurs faster than the maximum crystallization rate (g). A useful quantity that may help to predict whether conditions will allow crystallization or not is obtained dividing U by g.

$$\frac{U}{g} \propto \frac{d^4 (r_s - r_m) g}{16 k_B T} (1 - f)^b = P_e (1 - f)^b ;$$

where P_e is known as the Peclet number. The lower this magnitude is, the higher crystalline quality the sediment will have. In the case of silica spheres from 200 to 500 nm in water at 300 K, the Peclet number goes from O(10^{-4}) to O(10^{-2}). From this equation it can be seen that sphere diameter is the most important parameter to consider. The influence of the spheres volume fraction is not so clear. From this equation it seems that high concentrations will decrease the resulting value since sedimentation velocity is slowed down. However, it must be taken into account that a high concentration of spheres entails a larger aggregation rate and this fact is not included in the equation. For this reason the equation written above should be multiplied by a function $f(f)$ which some authors have assumed to be the volume fraction itself and the equation becomes $f \cdot P_e \cdot (1\text{-}f)^b$ instead.[24] The rest of parameters: density and temperature allow little variations on the final value of this equation.

A work presented by Hoogenboom *et al.*[24] shows that low Peclet number and volume fraction do not only result in higher quality crystals; the number of stacking faults which make the structure different from an fcc decreases as well.

This work also suggests that crystals fabricated from non-hard silica spheres (the surface charge is not screened) present a lower number of stacking faults.

So far, there is no parameter that could be realistically changed to obtain crystalline sediments of spheres larger than 500 nm. Nevertheless, it has been observed that increasing the medium viscosity by adding ethylene-glycol helps to fabricate large sphere opals.[25,26] High viscosity involves a lower sedimentation velocity which is favorable; however, it also entails poorer diffusion. For that reason viscosity does not appear in the Peclet number. Further experiments are needed to explain these results.

3.4 Colloidal crystal in aqueous suspension.

Natural sedimentation in a tube is a functional method to obtain solid opals but, unfortunately, it is not well suited for an in-situ crystallization study. The whole sediment thickness is less than one millimeter, the bottom surface has a low crystalline quality and upper surface is covered by the settling suspension or water once sedimentation is over. Therefore, the different solid, liquid and mixed phases present during crystallization and their behavior cannot be well observed. Only the water-colloid interface can be clearly appreciated and used to measure the sedimentation velocity.

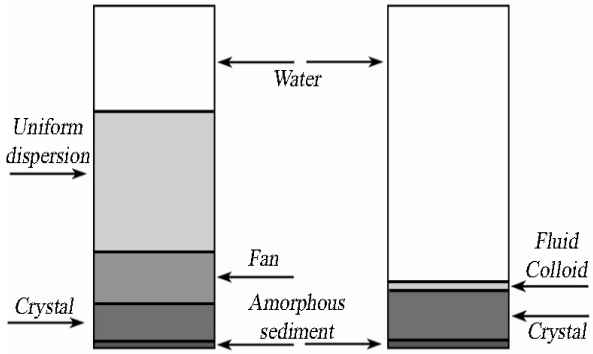

Fig. 3.2: Different phases that can be identified during (left) and after (right) colloid sedimentation.

In this section a different sedimentation mechanism that allows phase characterization is proposed. To prepare the cell, a silicon wafer is inserted between two glass-slides. The borders of the slides are glued together with a molten plastic and once the plastic is solidified the silicon slide is removed. The resulting cell contains an air chamber with an approximated thickness of 700 microns. A 20% volume aqueous suspension of silica spheres is then injected in the cell. The advantage of this cells when compared with previous experiments[14-16] is that small amounts of solid contents allow a clear observation of the different sedimentation phases.

Fig. 3.2 shows the different phases that can be observed during and after sedimentation. From the initial uniform dispersion of silica spheres in water, several phases are formed: the not yet settled uniform dispersion, an amorphous sediment at the bottom of the cell, a poly-crystalline sediment where long columnar crystals are present, a region known as the fan, at the bottom of which the critical osmotic pressure is reached. An interesting characterization of these phases and their growth velocity was published by Davis *et al.*[16] Once sedimentation is concluded, the fan and the uniform dispersion are no longer present and only the amorphous and crystalline sediments remain. Above the crystal, a liquid phase can be observed as well. In equilibrium in a gravitational field, the weight of all particles above any horizontal cross-section is compensated by the osmotic pressure.[27] Therefore, on the top of the sediment the osmotic pressure is below the critical value and a liquid phase exists. Although it is always present, this phase is still hardly observable for small spheres since the overall height of the liquid phase above the interface scales like:[28]

$$\frac{kT}{V_{sp}\left(r_s - r_m\right)g};$$

This means that for spheres with diameters around 200 nm, the height of this phase is of the order of a hundred microns, however for spheres of 500 nm, the height decreases to a few microns.

The amorphous sediment at the bottom of the cells is also present in solid opals grown by sedimentation (previous section) and offers an explanation to the low optical quality of the bottom side of those samples.

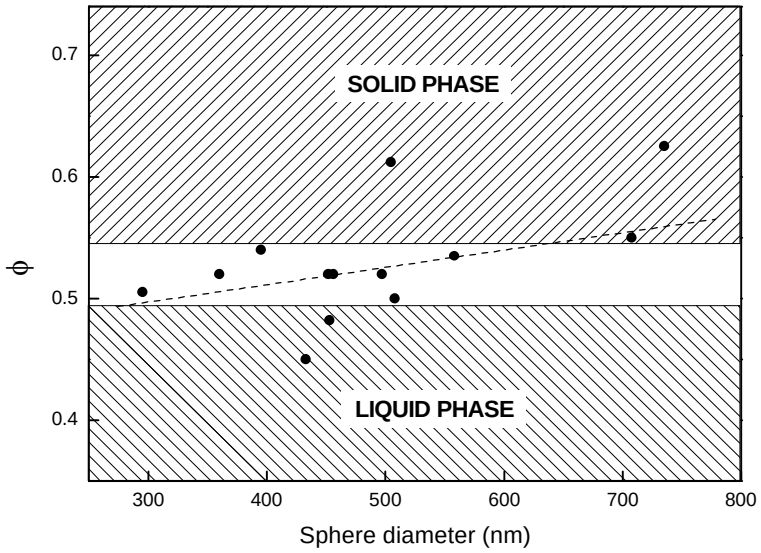

Fig. 3.3: Volume fraction of the crystalline phases obtained from optical measurements for different silica sphere diameters. The three regions predicted for hard spheres (solid, liquid and coexistent) are also depicted. The dashed line is a linear fit indicating a possible relationship.

The crystalline phase volume fraction for different diameters samples was obtained from optical measurements once the sedimentation process was over. The {111} planes are parallel to the glass slides. The results are shown in **Fig. 3.3**. The liquid, solid and coexistence phases predicted for hard spheres are also depicted. It can be seen that in our case most of the samples show a crystalline phase at a volume fraction region that belongs to the liquid-solid coexistence range for hard spheres. In fact, two of the samples show a crystalline phase for $\phi<0.49$. The explanation to these differences is that our system is not formed by hard spheres since their surface charge has not been screened. However, their qualitative behavior is very similar to that of hard spheres.[24] In some occasions this kind of systems are said to be made of nearly-hard spheres. Hard spheres equations are used introducing an effective diameter larger than that of the real sphere. In the case of charged spheres the Coulomb forces are added to the osmotic pressure to keep the spheres apart from each other.

Another interesting result from these experiments is that samples made of spheres larger than 500 nm presented a crystalline phase with good optical properties. In ref. 16, where the silica spheres surface charge was screened, spheres with diameters larger than 400 nm formed an amorphous sediment. Although other factors such as monodispersity are important to fabricate good quality crystals, results shown here suggest that surface charge may help to obtain crystals made of large spheres.

It is also remarkable that solid opals fabricated by means of natural sedimentation do not present good optical properties for diameters over *ca.* 500 nm. However, in the case of colloids in a suspension, same size spheres show a crystalline phase. A possible explanation is that the drying process destroys the existing crystals. Indeed, for large spheres, these crystals must be smaller since optical properties are worse. Therefore, perturbations may easily turn them into an amorphous solid.

The distance between two neighbor spheres (surface to surface) in terms of the volume fraction is given by:

$$d = \left[\frac{1}{\sqrt{2}} \left(\frac{4p}{6f} \right)^{1/3} - 1 \right] d;$$

from this equation it can be calculated that for crystals shown in this section where the volume fraction typically ranges from 0.45 to 0.60, the nearest neighbor distance varies from 18% to 7% of the sphere diameter. This is an interesting indication of the long range effects of electrostatic repulsive forces. In experiments with hard spheres, crystals show a volume fraction around 0.65. Consequently, the distance between spheres is only a 4-5% of the sphere diameter.

3.5 Electrophoretically assisted sedimentation.*

This technique was proposed as a solution to the problems which arise when SiO_2 monodisperse microspheres of diameters under 300 nm or over 550 nm are used to obtain opal based photonic crystals.[29,30] If the microspheres are too small, the sedimentation rate is very slow or even may never occur, a problem that has seemed as an inconvenience somewhat difficult to solve.[31,32] Conversely, if spheres are large enough no significant order can be achieved because sedimentation velocity and Peclet number are too high. Both problems make it quite unpleasant to work out of the limits of this reduced diameter range (300-550 nm) which corresponds to sedimentation velocities from 0.2 mm/hour to 0.7 mm/hour according to Stokes law.

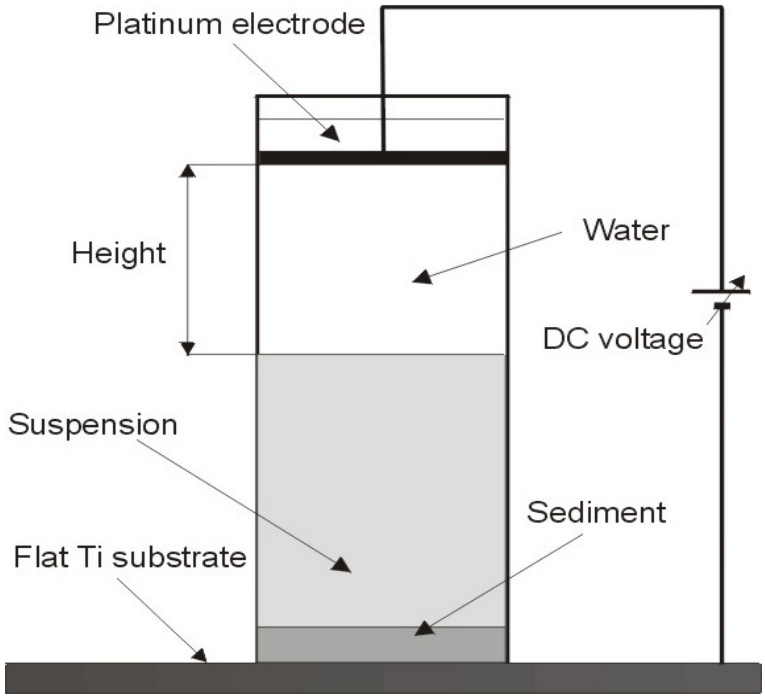

Fig. 3.4: Experimental set up of the electrophoretic cell. (Design and scheme made by M. Holgado)

The method here presented, based on the electrophoretic phenomenon, allows controlling the sedimentation velocity. The forces between particles[33] and the effects of electric fields over colloidal particles have been widely observed,[34,35] e.g. modulation of lateral attraction between particles and particle clustering.[36] The aim of this method is using the electric field to drive the sedimentation velocity and keep it around 0.4 mm/hour to solve the difficulties mentioned before.

* Results presented in this section were obtained in collaboration with M. Holgado who initially made use of electrophoresis with titania coated silica spheres.[30]

It is well known that silica microspheres in a colloidal suspension have a surface charge density when they are away from the point of zero charge (PZC), in which case the electric charge is null. Taking into consideration the force produced by an electric field *E* parallel to all other forces, the following equation is obtained for the velocity:

$$U = \frac{d^2(r_s - r_w)g}{18h} + mE$$

where, the first part of this equation is the classical Stokes law and the second part corresponds to the contribution of the electric field to the sedimentation velocity, related to the mobility of the spheres *m*. Now, the main problem is how to calculate the particle's mobility. The application of the electrophoretic concept can solve it. Provided that Stokes velocity without electric field is calculated with great accuracy, the electrophoretic mobility can be obtained in a straightforward manner if Stokes velocity is subtracted from the experimental velocity of the sample under a known electric field. Once the mobility is determined, the electric field necessary to achieve a given velocity can be stated beforehand.

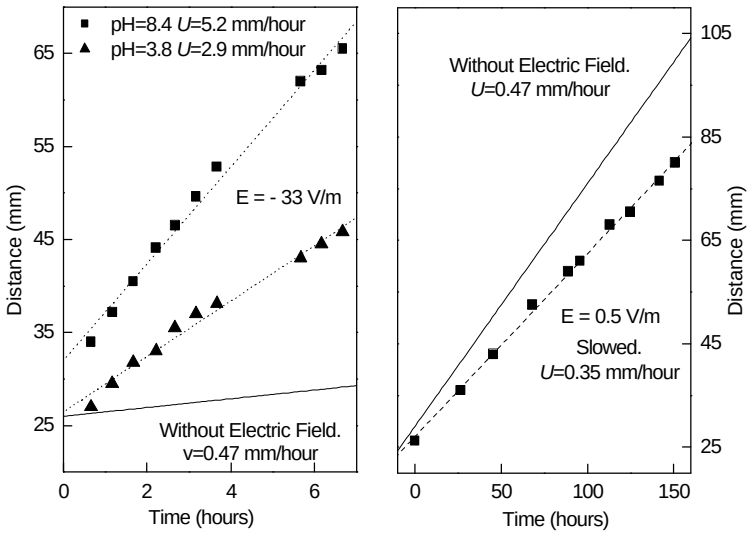

Fig. 3.5: SiO_2 spheres of 500 nm of diameter fall obeying the Stokes law. The sedimentation is faster (left) as the pH values move away from the PZC when an electric field is applied and slower (right) if it is inverted. The dotted lines are the data fits and their slopes give the velocities.

Several experiments according to what has been explained were performed and the mobility values obtained varied from -2 to -8 μm cm/V s in agreement with the range of values given by an independent study of the electrophoretic mobility in a Delfa Coulter 440. As moving away from the PZC increases the particle's charge, variations of the pH must involve changes in the mobility values. The colloidal suspensions of these experiments consisted of silica spheres in double-distilled water (with no added salt) in which the solid content was 0.5 vol.-%. The cell

where electrophoresis was performed (**Fig. 3.4**) consisted of a cylindrical tube (2 cm of diameter) of methyl acrylate fixed to the basis where the opal should settle, obtained from a standard silicon wafer sputtered with titanium (with less than 1 Armstrong of roughness and thick enough to assure a good conductivity). One of the main problems when dealing with these experiments was the electrolysis phenomenon, which has been reported elsewhere.[34] The solution adopted was the use of platinum for the upper electrodes because they have the highest Redox potential. Then, both electrodes were connected to a dc source used to obtain an electrical field. With this method compacts with thickness ranging between a few monolayers and 1 mm (depending on the amount of silica spheres used) with surfaces about 3.1 cm^2 are produced. To measure the sedimentation velocity, the height descended by the colloid/clear water interface (setting 0 mm the initial height) was monitored with time. The velocity results from experimental fit of height vs. time.

The response of SiO_2 spheres was studied. An electric field was applied to colloidal suspensions of SiO_2 spheres in which the original pH was varied by adding HCl to change the surface charge. The PZC of silica occurs at a pH=2.5, so pHs of the suspensions were chosen to be different enough without being close to the PZC: pH=3.8 and the reference value (no acid added) of pH=8.4. The results of the sedimentation velocities for silica spheres of 500 nm of diameter are graphically compared with the theoretical Stokes fall of a sample without electric field in the left panel of **Fig. 3.5**. It can be clearly seen that, as one moves away from the PZC, the mobility increases and so does *mE*.

pH	E(V/m)	m (mm cm/V s)	U (mm/h)
3.8	-33	-2.0	2.90
8.4	-33	-3.9	5.20
8.4	0.5	-3.9	0.35

Table 3-1: Mobilities and velocities from SiO_2 spheres of 500 nm of diameter at different pH and electric fields.

In order to study the effects of velocity variations on silica particle ordering, two more sedimentations were prepared from the same sample. One of them was left to fall without electric field, whereas in the other one the electrodes were inverted to decrease the sedimentation velocity by opposing the electric field to gravity. Since the mobility can be extracted from the previous experiment (m= -3.9 μm cm/V s), as explained, the electric field needed to get the desired velocity (U=0.4 mm/hour) was calculated to be 0.5 V/m. The experimental value (U=0.35 mm/hour, see right graph in **Fig. 3.5** was close to it. In **Table 3-1** the results from these experiments are numerically compared.

Electronic and optical microscopy studies of all these samples were made and it was observed that the slowed sedimentation sample presented a better ordering

than the one settled without field, while the accelerated samples from the previous experiment presented no order at all. Bragg diffraction was performed as well showing that the slowed opal presented well-defined Bragg peaks.

To prove how useful this method could be, SiO_2 spheres with a diameter of 870 nm were used. The purpose was to obtain a well ordered array by decreasing the natural velocity of this colloid (no electric field applied). **Fig. 3.6 a** shows a cleaved edge SEM image of a naturally settled opal. A high velocity (1.54 mm/hour) is obtained for these large spheres and no long-range order is achieved as shown by the Fourier transformed image in the insets of **Fig. 3.6**. An equal colloid of the same spheres was prepared and settled under a slowing electric field, in which the velocity was kept close to 0.35 mm/hour. **Fig. 3.6 a** and **b** show that only very small domains appear when electrophoretic technique is not applied while large domains are obtained when sedimentation is performed under an appropriate electric field. To check this, Fourier transforms from both images were performed; the opal settled under electric field presents a clear pattern that is not present in the natural settled opal.

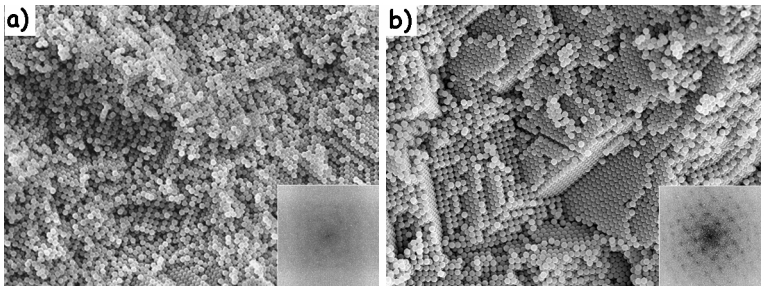

Fig. 3.6: SEM images of a cleaved edge of 870 nm of diameter SiO_2 spheres opal settled a) without and b) with an electric field. Insets show the images Fourier transform to make clearer the presence or not of periodicity in the samples. Images taken by H. Míguez.

A sample of quite small (205 nm of diameter) SiO_2 spheres, which would take one month to be settled, was prepared for sedimentation. It was accelerated from 0.09 mm/hour (natural velocity) to 0.35 mm/hour in order to complete the sedimentation in less than two weeks without decreasing the optical quality.

3.6 Vertical deposition of thin film opals.

In 1999 Jiang *et al.*[37] published a novel method to fabricate thin film solid artificial opals. The procedure was based on the results obtained by Nagayama and collaborators.[38] This method, known as vertical deposition, is becoming widely used and has taken over from other methods due to its multiple advantages:

- Good control over sample thickness.
- Samples with sizes of several square centimeters can be fabricated in one or two days.

- Samples are attached to a substrate (usually a glass or silicon slide) and its manipulation becomes easier.
- With the same amount of material used to obtain an opal by natural sedimentation several thin film opals can be fabricated.
- Since opals are much thinner, the number of defects when transmission optical measurements are performed is much lower.
- Infiltration of air voids with guest materials is easier in thin film opals since material must penetrate just a few layers.

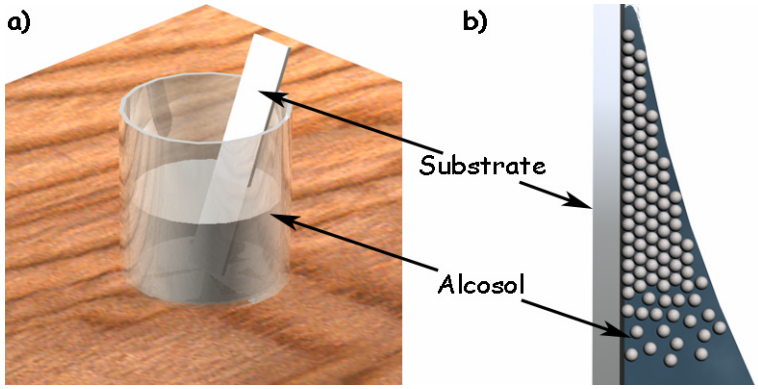

Fig. 3.7: a) Experimental setup to fabricate a thin film opal by means of the vertical deposition method. b) Meniscus formed in the interface between the substrate and the alcosol where the silica spheres are aggregated to form an fcc array.

Fig. 3.8: Thin film opal made of 660 nm silica spheres. The "level curves" denote the boundary between different number of layers. Scale bar is 250 microns.

In the experimental setup (**Fig. 3.7 a**), a clean substrate is placed into a vial containing a silica alcosol. The alcosol is a suspension containing a volume fraction ranging from 0.1% to 5% of silica spheres in ethanol. The resulting sample thickness depends on the volume fraction. The system is then left at room temperature. As was explained in section **3.2,** in order to crystallize, the spheres must reach a critical volume fraction. In this case capillary forces cause the spheres crystallization in the meniscus formed by the alcosol and the substrate (**Fig. 3.7 b**). To avoid a too fast aggregation rate, high initial volume fractions and evaporation rates must be avoided. The {111} planes are parallel to the substrate.

As presented, this method based on convection forces has a drawback: once again large spheres fail to crystallize. The reason is that for this method to work, spheres must be present at the suspension surface. In the case of silica spheres with diameters smaller than 500 nm, the evaporation rate is faster than sedimentation and spheres are always present in the meniscus. However, for larger spheres sedimentation velocity is higher. If temperature is increased the evaporation rate is boosted as well, but unfortunately spheres aggregation is too fast and an amorphous solid is obtained. A solution to this problem was presented by Vlasov *et al.*[39] Their proposal consisted in placing the vial in a temperature gradient. On the one hand the temperature at the surface of the suspension was low enough to obtain a valid evaporation rate. On the other hand, the temperature gradient causes convection forces and a continuous flow of spheres is directed towards the surface. Unfortunately their description was rather incomplete and the growing conditions have proven to be dependant on many parameters such as spheres initial volume fraction, the angle formed by the substrate on the vial and the kind of material the substrate is made of. Currently, there is still a need for a more detailed description of a reproducible procedure. Here, a route that has been successful to fabricate thin opals from silica spheres of 660 nm of diameter is described. Domains sizes are enough to obtain good spectra from areas as large as 330 x 330 μm^2. The procedure must, however, be improved further to control the number of layers and homogeneity. Nevertheless the samples produced were ideal for use in the experiments presented in Chapter 5.

The following recipe provides good results for silica spheres of 660 nm of diameter synthesized by means of the Stöber-Fink-Bohn[40] method. Although it has been said[37] that a coating of 3-(trimethoxysilyl)propyl methacrylate (TPM)[41] is not a key parameter in film deposition of smaller spheres it is our experience that order in samples is increased when TPM is used. The spheres are then dispersed in ethanol (0.8 % vol.). Si substrates (6 cm x 2 cm) are carefully cleaned in a solution of HF (1%) and afterwards another of H_2SO_4/H_2O_2 (2:1 vol). It must be noticed that conditions for glass slides would be significantly different. Finally the substrates are rinsed in doubly distilled water, acetone and ethanol. The dispersion of silica spheres and the substrates are placed in a clean scintillation vial (30 ml) within a furnace at 36 ºC and covered with a beaker. It is important not to set the substrates completely vertical (tilted 30 to 40 degrees respect to the vertical direction) or too thin opals (1-3 layers) are obtained. **Fig. 3.8** shows an optical microscope image taken with a 4X objective from one of the samples fabricated

with this method. The number of layers usually varies from 15 to 20 layers. In some occasions the number of layers can be counted very easily since “level curves” denote the boundary between different layers.

3.7 Summary.

In summary, a qualitative description of the parameters that influence crystallization and several methods to obtain artificial opals and study their growth have been reported.

3.7.1 Conclusions.

- Silica spheres in water tend to form crystalline sediments with a volume fraction close to 55%. Conversely, hard silica spheres crystallize at significantly higher volume fractions.[16]
- The crystalline quality of colloidal suspensions decreases with sphere diameter.
- Electrophoretically assisted sedimentation has proved to be a good technique to obtain solid opaline sediments made of silica spheres as large as 870 nm. In these experiments sedimentation velocity is reduced without affecting their diffusion coefficients.
- Sedimentation velocity could be increased as well to accelerate the fabrication of opals made of small silica spheres (200 to 300 nm).
- A recipe has been developed to fabricate thin film silica opals on silicon substrate made of spheres with a diameter close to 660 nm.

3.7.2 Future research.

- The effects of ethylene-glycol in the natural sedimentation method must be studied in more detail.
- The electrophoretic concept could be used to control the presence of small spheres in sedimentation when monodispersity is not granted. With appropriate electric fields small spheres could be directed towards the upper electrode while larger spheres form a sediment at the bottom.
- A reproducible and reliable method to fabricate uniform and thickness controlled thin film opals made of silica spheres with diameters larger than 500 nm is still needed.

3.8 References.

1 Williams, R. C. & Smith, K. M. Crystallizable Insect Virus. *Nature* **179**, 119 (1957).

2 Sanders, J. V. Colour of Precious Opal. *Nature* **204**, 1151 (1964).

3 Sanders, J. V. Diffraction of Light by Opals. *Acta Crystallographica Section a-Crystal Physics Diffraction Theoretical and General Crystallography* **A 24**, 427 (1968).

4 Darragh, P. J., Gaskin, A. J., Terrell, B. C. & Sanders, J. V. Origin of Precious Opal. *Nature* **209**, 13 (1966).

5 Stöber, W., Fink, A. & Bohn, E. Controlled Growth of Monodisperse Silica Spheres in Micron Size Range. *J. Colloid Interface Sci.* **26**, 62 (1968).

6 Philipse, A. P. Solid Opaline Packings of Colloidal Silica Spheres. *J. Mater. Sci. Lett.* **8**, 1371 (1989).

7 Astratov, V. N. *et al.* Optical spectroscopy of opal matrices with CdS embedded in its pores: Quantum confinement and photonic band gap effects. *Nuovo Cimento* **17**, 1349 (1995).

8 Yethiraj, A. & van Blaaderen, A. A colloidal model system with an interaction tunable from hard sphere to soft and dipolar. *Nature* **421**, 513 (2003).

9 Alder, B. J. & Wainwright, T. E. Phase Transition in Elastic Disks. *Physical Review* **127**, 359 (1962).

10 Ree, F. H. & Hoover, W. G. 7th Virial Coeffcients for Hard Spheres and Hard Disks. *J. Chem. Phys.* **46**, 4181 (1967).

11 Carnahan, N. F. & Starling, K. E. Equation of State for Nonattracting Rigid Spheres. *J. Chem. Phys.* **51**, 635 (1969).

12 Hoover, W. G. & Ree, F. H. Melting Transition and Communal Entropy for Hard Spheres. *J. Chem. Phys.* **49**, 3609 (1968).

13 Broughton, J. Q., Gilmer, G. H. & Jackson, K. A. Crystallization Rates of a Lennard-Jones Liquid. *Phys. Rev. Lett.* **49**, 1496 (1982).

14 Hachisu, S. & Kobayashi, Y. Kirkwood-Alder Transition in Monodisperse Latexes 2. Aqueous Latexes of High Electrolyte Concentration. *J. Colloid Interface Sci.* **46**, 470 (1974).

15 Pusey, P. N. & van Megen, W. Phase-Behavior of Concentrated Suspensions of Nearly Hard Colloidal Spheres. *Nature* **320**, 340 (1986).

16 Davis, K. E., Russel, W. B. & Glantschnig, W. J. Disorder-to-Order Transition in Settling Suspensions of Colloidal Silica - X-Ray Measurements. *Science* **245**, 507 (1989).

17 Woodcock, L. V. Entropy difference between the face-centered-cubic and hexagonal close-packed crystal structures. *Nature* **385**, 141 (1997).

18 Mayoral, R. *et al.* 3D long-range ordering in an SiO2 submicrometer-sphere sintered superstructure. *Adv. Mater.* **9**, 257 (1997).

19 Miguez, H. *et al.* Control of the photonic crystal properties of fcc-packed submicrometer SiO2 spheres by sintering. *Adv. Mater.* **10**, 480 (1998).

20 Kynch, G. J. A Theory of Sedimentation. *Transactions of the Faraday Society* **48**, 166 (1952).

21 Richardson, J. F. & Zaki, W. N. The Sedimentation of a Suspension of Uniform Spheres under Conditions of Viscous Flow. *Chem. Eng. Sci.* **3**, 65 (1954).

22 Maude, A. D. & Whitmore, R. L. A Generalized Theory of Sedimentation. *British Journal of Applied Physics* **9**, 477 (1958).

23 Batchelor, G. K. Sedimentation in a Dilute Dispersion of Spheres. *J. Fluid Mech.* **52**, 245 (1972).

24 Hoogenboom, J. P., Derks, D., Vergeer, P. & van Blaaderen, A. Stacking faults in colloidal crystals grown by sedimentation. *J. Chem. Phys.* **117**, 11320 (2002).

25 Ibisate M. Cristales fotónicos basados en ópalos. (PhD. thesis, Universidad Autónoma de Madrid, 2003).

26 Ibisate, M. *et al.* Effect of the Solvent Composition on the Optical Quality of Colloidal Photonic Crystals. *To be published.*

27 Piazza, R., Bellini, T. & Degiorgio, V. Equilibrium Sedimentation Profiles of Screened Charged Colloids - a Test of the Hard-Sphere Equation of State. *Phys. Rev. Lett.* **71**, 4267 (1993).

28 Pieranski, P. Colloidal Crystals. *Contemp. Phys.* **24**, 25 (1983).

29 Holgado, M. *et al.* Electrophoretic deposition to control artificial opal growth. *Langmuir* **15**, 4701 (1999).

30 Holgado, M. Cristales de ondas. (PhD. thesis, Universidad Politécnica de Madrid, 2000).

31 Park, S. H., Qin, D. & Xia, Y. Crystallization of mesoscale particles over large areas. *Adv. Mater.* **10**, 1028 (1998).

32 Mei, D. B. *et al.* Visible and near-infrared silica colloidal crystals and photonic gaps. *Phys. Rev. B* **58**, 35 (1998).

33 Atkins, D., Kekicheff, P. & Spalla, O. Adhesion between colloidal silica as seen with direct force measurement. *J. Colloid Interface Sci.* **188**, 234 (1997).

34 Trau, M., Saville, D. A. & Aksay, I. A. Field-induced layering of colloidal crystals. *Science* **272**, 706 (1996).

35 Sarkar, P. & Nicholson, P. S. Electrophoretic deposition (EPD): Mechanisms, kinetics, and application to ceramics. *J. Am. Ceram. Soc.* **79**, 1987 (1996).

36 Solomentsev, Y., Bohmer, M. & Anderson, J. L. Particle clustering and pattern formation during electrophoretic deposition: A hydrodynamic model. *Langmuir* **13**, 6058 (1997).

37 Jiang, P., Bertone, J. F., Hwang, K. S. & Colvin, V. L. Single-crystal colloidal multilayers of controlled thickness. *Chem. Mat.* **11**, 2132 (1999).

38 Dimitrov, A. S. & Nagayama, K. Continuous convective assembling of fine particles into two-dimensional arrays on solid surfaces. *Langmuir* **12**, 1303 (1996).

39 Vlasov, Y. A., Bo, X. Z., Sturm, J. C. & Norris, D. J. On-chip natural assembly of silicon photonic bandgap crystals. *Nature* **414**, 289 (2001).

40 Stöber, W., Fink, A. & Bohn, E. Controlled Growth of Monodisperse Silica Spheres in Micron Size Range. *J. Colloid Interface Sci.* **26**, 62 (1968).

41 Philipse, A. P. & Vrij, A. Preparation and Properties of Nonaqueous Model Dispersions of Chemically Modified, Charged Silica Spheres. *J. Colloid Interface Sci.* **128**, 121 (1989).

Chapter 4: Optical characterization of artificial opals.

4.1 Introduction.

Opals are used as templates to fabricate other topographies which may present different optical properties. Obviously it is necessary to have an accurate knowledge of the initial structure to understand the final photonic crystal optical behavior. In Chapter 3 some of the methods to fabricate artificial opals were presented. In order to characterize them, Scanning Electron Microscopy (SEM) allowed obtaining some information about the structural properties of the samples. Unfortunately this technique is destructive and the amount of information extracted does not provide a rich enough description of the opal properties. Lattice parameter and refractive index (RI) are two of these characteristics for which SEM does not provide as accurate information. In the present chapter techniques based on optical characterization will be introduced to complete the photonic crystal description.

As a structure where the refractive index is modulated, the optical response of an opal varies depending on the direction studied. Even though RI contrast is rather low for silica opals (1.425:1.000), the anisotropy effects, especially at high energies, make the data interpretation a non trivial issue. From sections 4.2 to 4.4 some of the valid and more widespread approximations to understand the optical behavior of the structures will be presented along with their validity limits. The remaining sections will show actual cases of opals that have been characterized thanks to those theoretical approaches.

Although optical experiments shown in this thesis correspond to artificial opals made of silica spheres, techniques described in this chapter can be applied to other similar systems. As an example, optical properties of opals made of polystyrene (PS) or poly(methyl methacrylate) (PMMA) spheres are analogous since their refractive indexes are relatively close to that of silica.

4.2 Artificial opal photonic band structure.

An artificial opal made of silica spheres does not present a complete photonic band gap (cPBG).[1] As explained in Chapter 1, to obtain a cPBG an fcc structure of spheres embedded in a high dielectric constant material should be made so that the RI ratio between the embedding material and that of the spheres were above 2.8. For this reason opals are usually regarded as templates to load with a high RI material. They are used as an intermediate step to obtain a structure with a cPBG.

Fig. 4.1 shows the photonic band structure of the twenty lowest energy bands for an fcc structure made of spheres with a RI of 1.425* in air, calculated with the plane wave method (PWM).[2] The diagram shown in this band scheme shows the most relevant directions. As mentioned above there is no cPBG. However, for some directions and energies there are regions not covered by any band, these are the so called pseudogaps. These pseudogaps do not allow the propagation of light

* This value was the average refractive index for as-synthesized silica spheres (Chapter 2).

through the opal and cause transmission dips or reflectance peaks in the sample spectra. Studying the experimental behavior of the pseudogaps helps to characterize the artificial opal and gives information about the optically relevant parameters (i.e. structure, topography, lattice parameter, refractive index, etc).

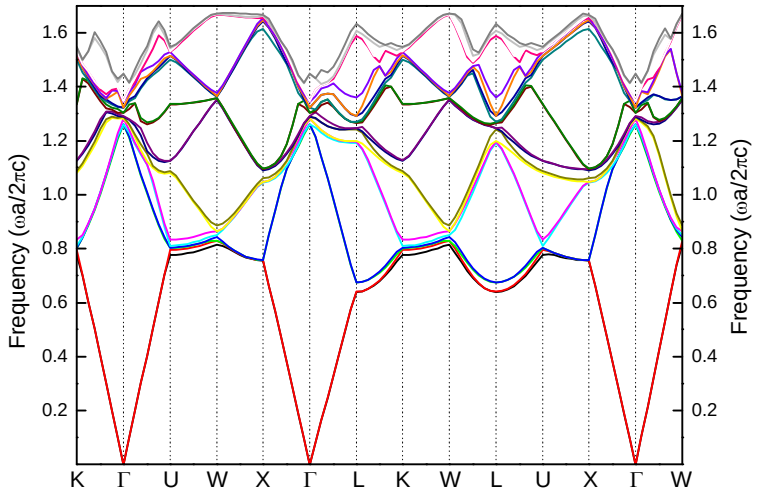

Fig. 4.1: First 20 bands of the photonic band structure for an fcc structure made of spheres with a refractive index of 1.425 in air.

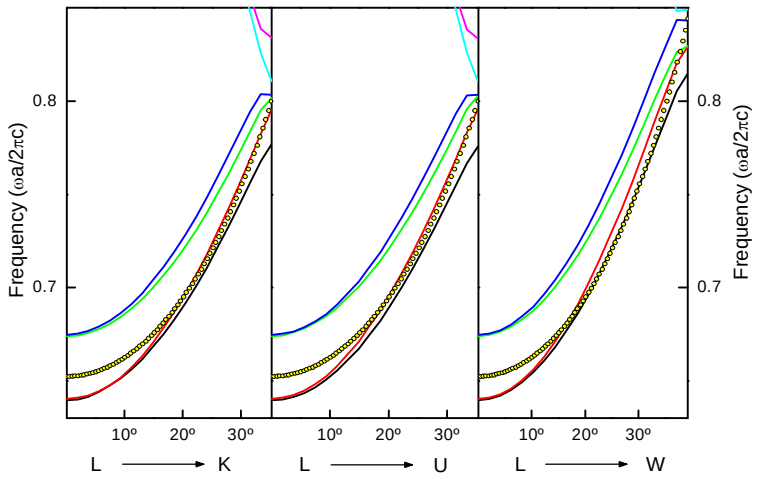

Fig. 4.2: Bands 1 to 4 for different directions in terms of the internal angle compared to Bragg's law (yellow circles). Bands are extracted from **Fig. 4.1**.

4.3 Bragg's law.

Being able to experimentally study all the directions would provide a lot of useful information about the photonic crystal. However, opals are usually grown in the (111) direction[3] and, therefore, only the optical properties around the ΓL

direction can be probed. The first pseudogap in this direction will cause a diffraction peak centered at a/l=0.657 (see **Fig. 4.1**). By introducing the wavelength of this diffraction peak in this relationship, the lattice parameter can be deduced. In the case of touching spheres in an opal $a=\sqrt{2}d$ and therefore the diameter can be calculated as well: $d=0.465\cdot l$.

If the sample is tilted, the diffraction peak wavelength will change. Depending on the orientation of the sample, the Brillouin zone (BZ) could be scanned from the L point towards the U, K or the W points (see Appendix I). Unfortunately, artificial opals usually present domains showing a mosaic spread effect and it is very difficult to know the direction under study while tilting the sample. Nevertheless, this does not present an important inconvenience since the four lowest bands in the vicinity of the L point for an opal structure are identical irrespective of the direction along the surface of the BZ for an internal angular range of 0–34° and slightly departing from a common behavior only for higher angles. This can be observed in **Fig. 4.2**.

The experimental results can be compared to the bands shown in **Fig. 4.2**, the impinging external angle is converted into the internal angle by means of the Snell's law. This approach is relatively accurate at low energies but not completely strict since refractive index is not well defined in a photonic crystal. In reality refractive index depends on the direction and light frequency. For this reason, many authors prefer to present bands and data in terms of parallel wave-vector instead of internal angle because this value is conserved[4] on refraction.

Although direct comparison of experimental data and band structure gives the most accurate results, it is very useful to work with an analytical expression. In this sense a simple geometrical approach yields an equation that reproduces the behavior of the first pseudogap wavelength with varying angle. This is nothing but Bragg's law and consists in regarding spheres as point scatterers forming planes. These planes scatter light and for certain directions and wavelengths these scattered waves are added up. The equation can be obtained in the same way it is obtained for X-rays but in this case it must be taken into account that the photonic crystal has a refractive index different to that of air. With some geometrical considerations along with the Snell law this expression is easily obtained:[5]

$$l = 2f\left[e_c - e_m \sin^2(q_{ext})\right]^{1/2};$$

where f is the distance between planes, e_c and e_m are the photonic crystal and surrounding medium dielectric constant respectively and q_{ext} is the external impinging angle with respect to the normal. In the case of the ΓL direction in an opal (fcc lattice) the distance between planes is $f=2a/\sqrt{3}$ where a is the lattice parameter. The results given by Bragg's law are shown as yellow circles in **Fig. 4.2**. To obtain this data, the equation above is written in terms of the internal angle and e_c is taken as the average dielectric constant of the spheres and the host dielectric while e_m is air. Thus:

$$\frac{a}{l_{111}} = \frac{\sqrt{3}}{2\cos(q_{\text{int}})\sqrt{\langle e \rangle}}; \quad \langle e \rangle = fe_s + (1-f)e_h;$$

where f is the filling fraction of the spheres (ca. 0.74 for touching spheres) and e_s and e_h are the spheres (silica, 2.03) and host (air, 1.00) dielectric constants.

As can be seen in **Fig. 4.2** the results given by Bragg's law are rather accurate for a bare opal although there is a slight tendency to underestimate the frequency at which the diffraction peak should be observed. Bragg's law equation allows working with a very simple model to obtain some information about the photonic crystal. However this information is limited to the wavelength of the first pseudogap and other characteristics such as the peak width remain unknown. Also, and due to symmetry reasons, some of the wave-vectors that lie on the Brillouin surface are not diffracted however (see for example that there is no pseudogap for the ΓX direction at low frequencies, see **Fig. 4.1**). This fact is not reflected by Bragg's law and more complex approaches are needed to reproduce this behavior. Finally, the results obtained with Bragg's law will strongly depend on the dielectric constant we choose for the photonic crystal. Here the average dielectric constant was used but this choice is not always valid and this is not a trivial matter as will be shown in the next section.

4.4 Effective dielectric constant.

As explained in Chapter 1, the RI is not a well defined parameter for a photonic crystal.[6] Its value can be extracted from the slope of the bands and it may drastically differ for each frequency and propagation direction. However, the RI is relatively well defined at low energies and some calculations can be done assuming a constant value. An example of one of these approximations was explained in the previous section for Bragg's law. There, the effective dielectric constant (e_{eff}) of a bare opal was taken as the average value of the materials forming the lattice. The questions are: how good this approximation is and, is it always valid? Is the average dielectric constant the best choice?

An accurate way to know the effective dielectric constant for a photonic crystal at low energies is to calculate the band structure and obtain it from the slope of the bands at low energies ($\mathbf{k} \rightarrow 0$). It must be noticed that even for energies as low as those around the first pseudogap the dielectric constant begins to differ from the value obtained at $\mathbf{k} \rightarrow 0$ since bands begin to warp in the proximity of the Brillouin surface.

Although calculation methods are becoming faster and faster it is still very convenient to have an analytic expression to calculate e_{eff}. The average dielectric constant ignores the vector nature of light and is the simplest and fastest way but not the only one. Another widespread approximation that has proven to give better results for some specific cases is that developed by Maxwell-Garnett[7] for small, isolated and diluted spheres embedded in a medium:

$$e_{M-G} = e_h \frac{1+2fa}{1-fa}; \qquad a = \frac{e_s - e_h}{e_s + 2e_h};$$

The values for e_{eff} obtained with these three methods (average, Maxwell-Garnett and band calculations with the plane wave method) are shown in **Fig. 4.3**. The graph on the left shows the values obtained for an opal made of dielectric spheres in air, central plot shows an opal of silica spheres in a dielectric while the graph on the right shows an inverse opal of air spheres in a host dielectric. As can be observed, in both cases, the three methods give similar values when the materials forming the photonic crystals have low dielectric constants. However as the dielectric constant contrast is increased, the values given by the analytical expressions begin to substantially differ from the $\mathbf{k} \rightarrow 0$ value. At sight of these plots, it can be seen that the average dielectric constant will give more accurate results for direct opals while the Maxwell-Garnett expression is definitively better for low RI spheres in a dielectric. This is in accordance with previous works.[8] Nevertheless, for high dielectric constant materials the best option is to calculate e_{eff} from the band structure.

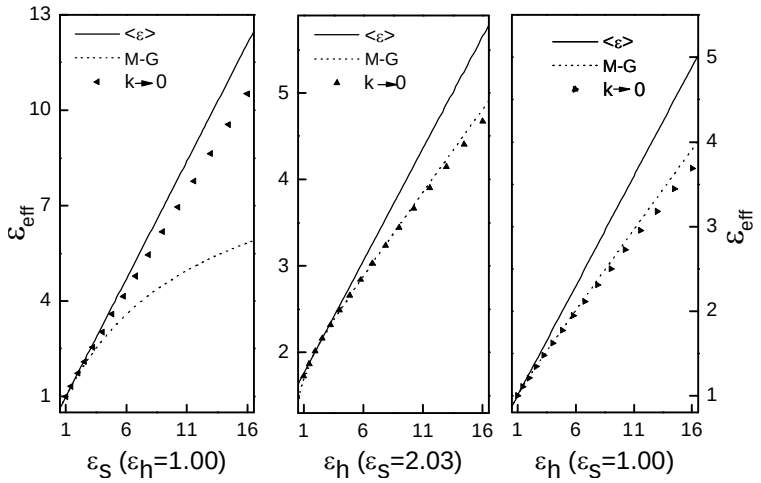

Fig. 4.3: Effective dielectric constant as a function of the sphere or host material dielectric constant obtained from three different methods: average (solid line), Maxwell-Garnett (dashed line) and band structure (triangles) with the plane wave method. The values are given for an fcc structure of dielectric spheres in air (left), silica spheres in a dielectric (center) and an inverse opal of air spheres in a dielectric host (right). The filling fraction is 0.74.

Fig. 4.4 shows the normalized frequency at which the center of the first pseudogap in the ΓL direction should be located for a direct opal of dielectric spheres in air (solid lines) and air spheres in a host dielectric (dashed lines). The results from band structure calculations with the plane wave method are compared to those obtained with Bragg's law and the average dielectric constant. Once again it can be observed that Bragg's law is a good approximation for low dielectric constant contrasts but insufficient when contrast is increased. **Table 4-1** shows

some useful data for different configurations of direct and inverse opals, including the first pseudogap frequency in the ΓL direction and values of the dielectric constant depending on the calculation method. The filling fraction is always 74% for the spheres material (touching spheres).

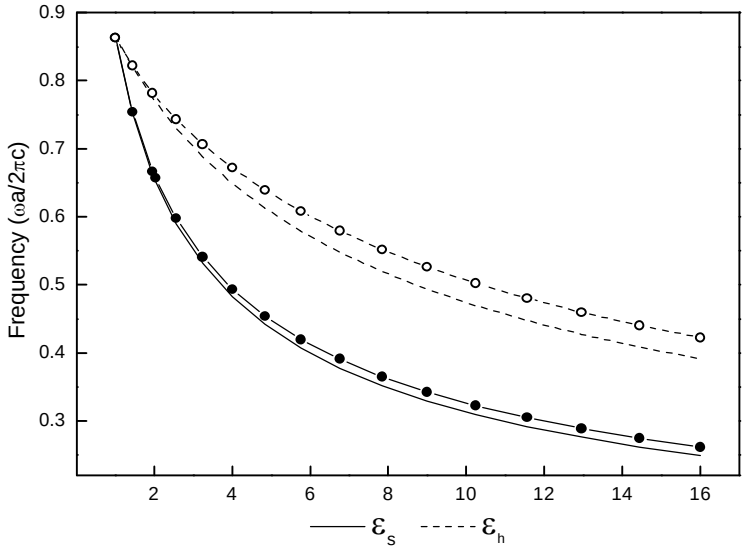

Fig. 4.4: Normalized frequency position for the first pseudogap of an fcc lattice of dielectric spheres in air (solid line) and air spheres in a dielectric host (dashed line). The results obtained from the band structure (circles) are compared to those calculated from Bragg's law (without circles) with an average dielectric constant as the e_{eff}. The filling fraction for all cases is 0.74.

Material	$e_s : e_h$	$wa/2\pi c$	$e_{k\to 0}$	$e_{M\text{-}G}$	$\langle e \rangle$
Silica Opal	2.03 : 1.00	0.657	1.73	1.71	1.77
Latex Opal	2.53 : 1.00	0.600	2.07	2.00	2.13
PMMA Opal	2.25 : 1.00	0.635	1.88	1.84	1.93
Silica IO	1.00 : 2.03	0.777	1.23	1.23	1.27
Silicon IO	1.00 : 11.9	0.475	3.01	3.13	3.83
Germanium IO	1.00 : 16.0	0.423	3.69	3.92	4.90

Table 4-1: Some useful data for different direct and inverse opal (IO) configurations. Filling fraction is always 74% for the material forming the spheres Third column shows the normalized frequency of the first pseudogap in the ΓL direction.

4.5 Colloidal crystal characterization.

In Chapter 3, the formation of a colloidal crystal of silica spheres in water was studied. It was shown that the volume fraction of these structures is around 54%.

However, the volume fractions for each sample were deduced by means of optical measurements, specifically, studying the position of the first order diffraction peak in the ΓL direction. For this purpose Bragg's law should be expressed in terms of the volume fraction and the sphere diameter (known beforehand). The volume fraction for an fcc structure is:

$$f = \frac{2pd^3}{3a^3} \rightarrow a = d\left(\frac{2p}{3f}\right)^{1/3};$$

Now we substitute the lattice parameter in Bragg's equation with the previous expression:

$$l = \frac{2^{4/3}p^{1/3}}{3^{5/6}} d\ f^{-1/3}\left[(e_s - e_h)f + e_h - \sin^2(q_{ext})\right]^{1/2};$$

$$l \approx 1.477\, d\ f^{-1/3}\left[(e_s - e_h)f + e_h - \sin^2(q_{ext})\right]^{1/2};$$

This equation is expected to give reasonably accurate results for low dielectric constant values and contrasts. These conditions are fulfilled in our case since e_s=2.031 (silica spheres) and e_h=1.777 (water). **Fig. 4.5** shows an example of reflectance spectra at different angles for a colloidal crystal. The volume fraction is then extrapolated from the bottom plot which represents the relationship between volume fraction and the wavelength.

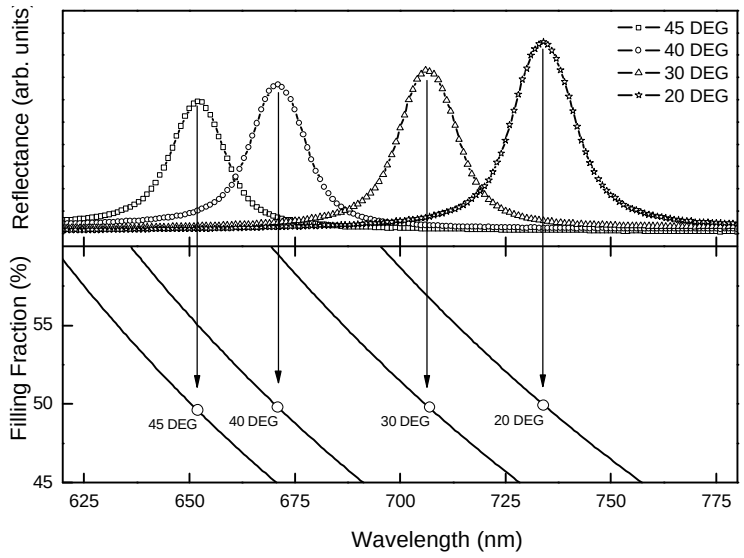

Fig. 4.5: Bragg's diffraction wavelength (top graph) of a colloidal crystal of 295 nm of diameter silica spheres in water is used to determine the volume fraction of the structure (bottom graph). For this sample the volume fraction of silica is 49.8%.

Apart from the volume fraction there is more information that can be extracted from the diffraction peaks. Indeed, the quality of the sample is related to the

breadth of the diffraction peak; a peak broader than what theory predicts is an effect attributed to the disorder within the sample. Bragg's equation presented in the previous section does not give any information about the peak width. In this sense the scalar wave approximation (SWA) gives some results discussed elsewhere.[9] **Fig. 4.6** shows the gap to midgap ratio (first pseudogap in the ΓL direction) as a function of the volume fraction for fcc lattices made of silica spheres in water. The data has been calculated with the PWM.[2]

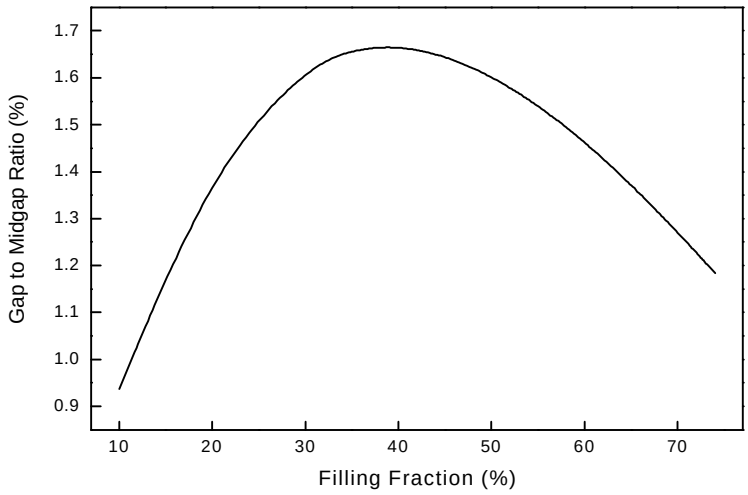

Fig. 4.6: First pseudogap relative width in the ΓL direction for an fcc structure of silica spheres (n=1.425) in water (n=1.333).

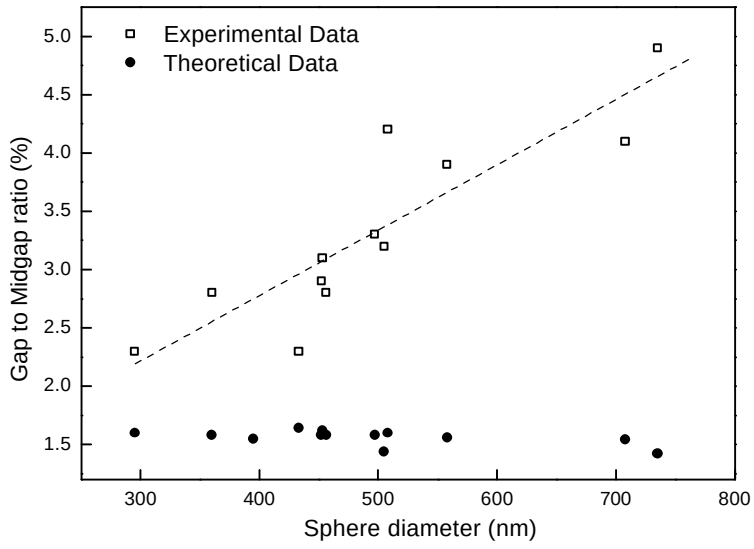

Fig. 4.7: Experimental relative-width of the Bragg peak of colloidal crystals obtained from silica spheres in water compared with the theoretical expectations of the relative-width of the first pseudogap in the ΓL direction. Each sample volume fraction is obtained from Chapter 3 and its theoretical relative-width from **Fig. 4.6**. Dashed line is just an eye-guide.

The experimental diffraction peak relative-width for each of the studied samples is compared with their theoretical relative-width values* in **Fig. 4.7**. It can be clearly observed that experimental peak width broadens as sphere diameter increases. This corroborates that the ordering of samples grown by sedimentation tends to worsen for larger spheres.

4.6 Thin film opal optical properties.

Thin film opals[10] present some special characteristics in their optical properties which cannot be observed on thicker opals. The interference of light reflected by the top and bottom surfaces causes the well known Fabry-Perot interferences.[11] As a matter of fact these interferences are always present in opals. However, opals grown by other techniques such as natural sedimentation or electrophoresis are too thick and fringes form a continuous background. In the case of thin film opals these oscillations can be clearly observed. **Fig. 4.8** shows the band structure (left) in the ΓL direction compared with the experimental spectrum of a thin film opal made of silica spheres and grown on a silicon substrate (center). The first pseudogap position matches the frequency at which the diffraction peak in the experimental spectrum appears. The Fabry-Perot fringes can be seen at both sides of the Bragg peak.

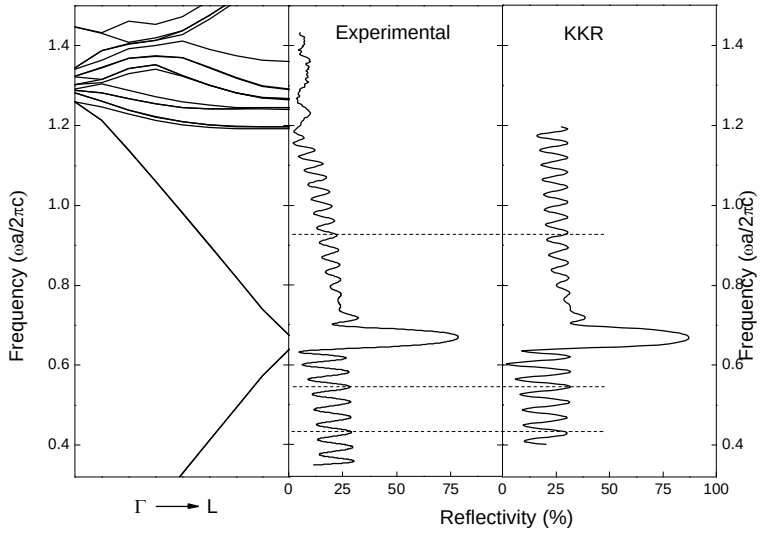

Fig. 4.8: Photonic band diagram in the ΓL direction for an opal of silica spheres in air (left). Experimental reflectance spectrum normal to the (111) planes for a 17 layers thin film opal of 676 nm diameter silica spheres (center). Theoretical reflectance spectrum normal to the (111) planes for the same crystal calculated by the KKR method (right).

* Calculated as the full width at half maximum divided by the center of the peak spectral position.

Dashed lines are eye-guides to show the frequency position agreement between experimental and theoretical results.

Theoretical calculations with the KKR[12] method were performed to simulate a 17 layer opal of silica spheres in air on a silicon substrate. The result is shown on the right plot of **Fig. 4.8** and shows an excellent agreement with the experimental spectrum. The fringes positions match in both cases, especially at the lowest energies. The mismatch at higher energies is probably due to a little difference between the RI used for calculation and the real one. Also the diffuse scattering effects due to defects present in the sample are responsible of a reflectance intensity of the Bragg peak lower than expected by the KKR calculations: 77% and 87% in the experimental and theoretical spectra respectively.

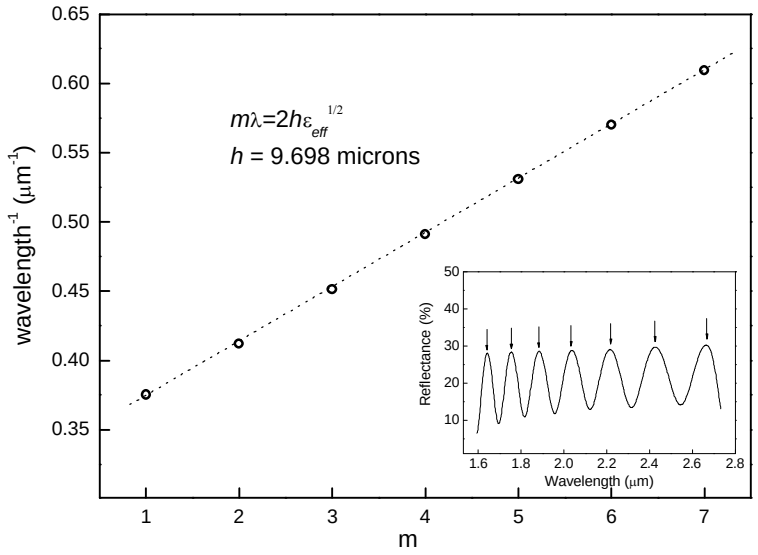

Fig. 4.9: The thickness of the sample can be calculated from the maxima of reflectance of the Fabry-Perot fringes (*m* is the resonance order). The inset shows the actual reflectance spectrum for energies below the first pseudogap.

The thickness of the sample and therefore the number of layers is an interesting parameter to consider when studying the optical properties of the thin film opal. The experimental spectra could be compared with the theoretical data to know the number of layers but calculating it from an analytical expression would be more appropriate for the sake of simplicity. From the spectral separation of the Fabry-Perot fringes the thickness of the sample can be calculated. Local reflectance maxima due to the Fabry-Perot resonances will appear at (for an opal on a substrate with a RI higher than that of the opal[11]):

$$m\,l = 2he_{eff}^{1/2} \quad \Rightarrow \quad \frac{1}{l} = \frac{m}{2he_{eff}^{1/2}};$$

where *m* is the resonance order and *h* is the sample thickness. Plotting the inverse wavelength as a function of the resonance order (that must be an integer although its exact value is unknown), a linear relation is obtained. From the slope of it the thickness of the sample can be calculated. **Fig. 4.9** shows an example of how this procedure is followed. In this case the opal has a thickness of 9.698 μm which corresponds to a 17 layers thin film opal of 676 nm diameter silica spheres. In this case the effective dielectric constant used in calculations is 1.73, which corresponds to the dielectric constant obtained at $\mathbf{k} \rightarrow 0$ from the band structure (see **Table 4-1**).

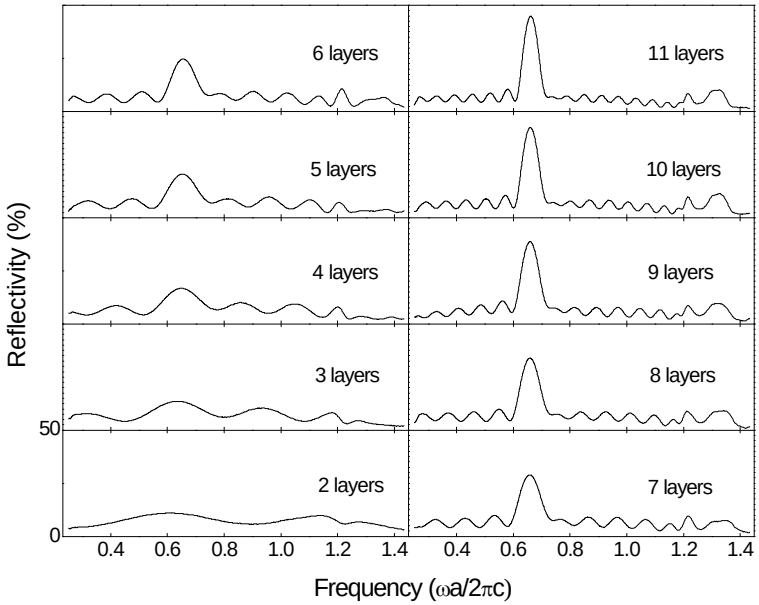

Fig. 4.10: Reflectance spectra from a thin film opal with an increasing number of layers (from 2 to 11). The opal is made of silica spheres with a diameter of 507 nm on a glass substrate. The ordinate axis (reflectance) for every graph ranges from 0 to 50%.

The control that thin film opals growth methods allow on the number of layers makes this kind of crystals suitable to study the evolution of the photonic properties. The theory of photonic band structures has been developed assuming that crystals were infinite; of course this is just an approximation and structures with a large enough number of layers can be taken as infinite crystals. An important question is how many layers an opal should have to be considered as infinite. Bertone *et al.*[9] tried to answer this question with some theoretical considerations and experimental results extracted from optical density spectra of thin film silica opals. Their results showed that a low number of layers (about 13 for silica spheres in air) should be enough to have a constant Bragg peak width and intensity. Experimental results published by Galisteo-López *et al.*[13] for thin film opals made of PS spheres have shown that for a real convergence the number of layers should be increased up to ca. 35. **Fig. 4.10** shows the reflectance spectra of thin film opals made of silica spheres of 507 nm with increasing number of layers

(from 2 to 11). As can be observed, increasing the number of layers boosts the intensity and narrows Bragg peaks while the spectral distance between Fabry-Perot fringes diminishes. It is worthy to notice that at 11 layers the Bragg peak reflectance still increases and its breadth decreases. However, the high energy diffraction peaks centered on 1.25 (normalized frequency) remain constant once the opal is 8-9 layers thick.

Finally, thin film opals allow the study of the hexagonal diffraction patterns due to the light diffraction by the first layer of spheres. Actually, this pattern is the Fourier transform of the crystal surface. Characterizing the behavior of these spots in terms of angular dependence makes possible to infer the size of spheres forming the lattice.[14] This method is quite advantageous since it is non-destructive and does not depend on the effective dielectric constant within the photonic crystal. The diffraction pattern has been successfully used as well as a method to orient the sample since its Fourier-transform gives the arrangement of the spheres in the real space.[13] The only disadvantage of this method is that light wavelength used to observe the diffraction pattern must accomplish that $l_0 < nd\cos(30)$ where n is the embedding RI (usually air) and d is the sphere diameter. **Fig. 4.11** shows the six diffraction spots caused by a He-Ne laser impinging on a sample made of 780 nm spheres.

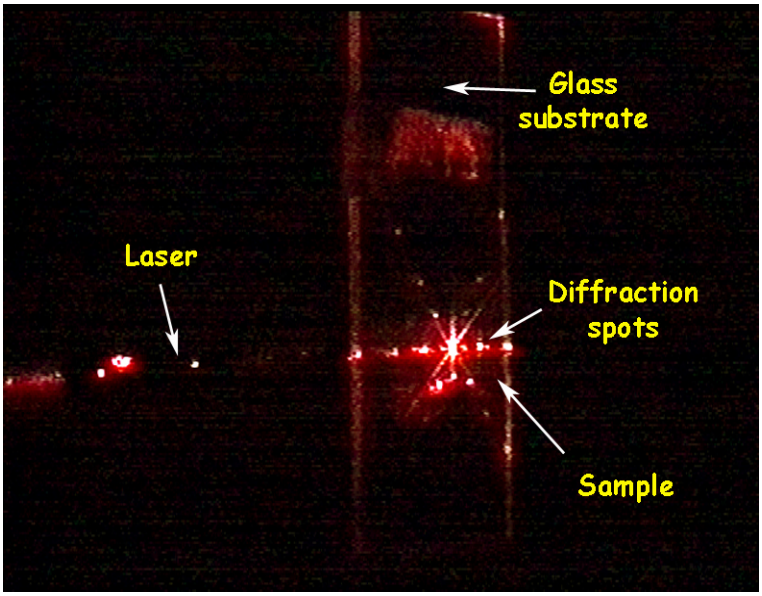

Fig. 4.11: Diffraction spots caused by the {111} planes of an opal made of 780 nm spheres when an He-Ne laser hits the thin film opal. Several diffraction orders can be observed around the zero order spot in the center of the sample.

4.7 Opal made of silica spheres with a metallic core.

The use of composite, nanostructured materials is acquiring a great interest both from a fundamental point of view and for an increasing number of potential

practical applications. The incorporation of several components with markedly different properties opens up a whole range of possibilities that cannot be achieved with conventional single-component systems. Within the broad range of nanoparticle compositions currently under study, noble metals have received a special interest because of the coupled oscillation of surface free electrons when interacting with an external electromagnetic wave of a certain wavelength, which is termed surface plasmon.[15] The frequency of the plasmon resonance mainly depends on the metal nature, the size and shape of the nanoparticle, and the surrounding medium nature.[16,17]

It has been predicted that fcc structures made of metallic spheres (coated or not with a dielectric layer) could lead to important improvements in optical features over those made of dielectric particles.[18,19] Photonic crystals comprising metals in their composition have been prepared previously, either by infiltration of nanoparticles,[20,21] electroless deposition,[22] or electrochemical deposition.[23] Preliminary results were also recently shown on the use of gold nanoshells as units for opal formation.[24] All these methods end up with a system in which bulk-like gold is obtained, since there is direct physical contact between neighboring units.

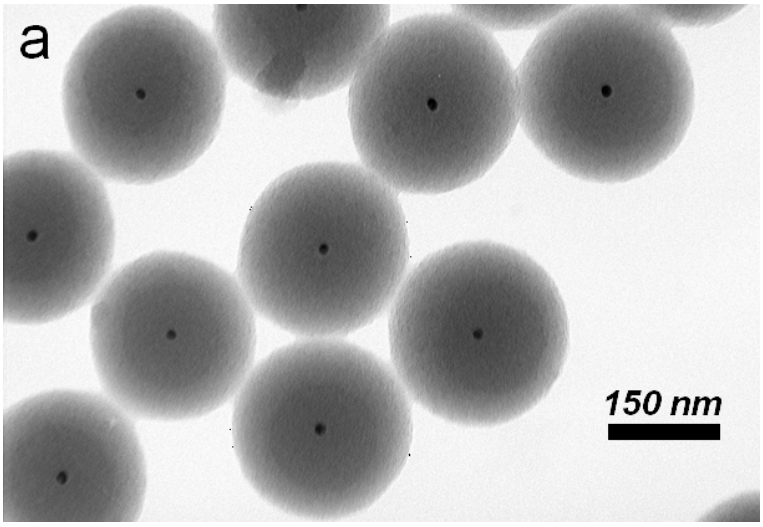

Fig. 4.12: TEM micrograph showing the core-shell morphology of the composite colloid spheres used for opal formation. Sphere diameter is 225 nm and gold nuclei are 15 nm ca. (Picture obtained by J. B. Rodríguez from the CACTI of Vigo University).

In this section the optical properties of a novel system that joins together the optical properties of metal nanoparticles and photonic crystals are presented. The incorporation of metal nanoparticles within colloidal crystalline arrangements is made through the synthesis of composite, core-shell colloid spheres comprising a metallic nanoparticle as the core and amorphous silica as the shell.[25*] On the one

* Samples synthesized by V. Salgueiriño-Maceiras and L. Liz-Marzán at Universidade de Vigo.

hand, the size of the core is uniform enough to display a well-defined plasmon band. On the other hand, the thickness of the shell is large enough to enable the formation of a crystalline arrangement with a suitable lattice constant to yield photonic bandgap effects in the visible. After the synthesis of such composite spheres, synthetic opals are obtained by means of the simple natural sedimentation method, and the robustness and mechanical stability of the crystals is enhanced through a sintering process. Since metal cores are far apart from each other, the properties of single nanoparticles are fully preserved in the opal.

Fig. 4.12 shows representative transmission electron micrographs of the core-shell particles used for this study, where the monodispersity, both in the core size and in the total diameter can be easily observed.

4.7.1 Reflectance and transmission spectra.

The study of the optical properties is described, not only for dry opals, but also after infiltration with liquids of varying composition (which implies varying refractive index). The purpose of such an approach was investigating the possible coupling between plasmon absorption and Bragg reflection. Therefore, an optical study of the opals was performed through measurements of both transmittance and reflectance. In order to cover a range that includes the refractive index of silica, mixtures of water (n=1.333) and glycerol (n=1.475) were used. The results are shown in **Fig. 4.13** and **Fig. 4.14** for reflectance and transmittance, respectively.

In principle, two independent phenomena are expected to govern the optical properties of these composite systems. On the one hand, the plasmon resonance associated with the Au nanoparticle cores embedded in a medium with the refractive index of silica (ca. 1.46). For these systems, the band is expected to be around 525 nm[23] and it must be clearly observable, since their concentration is relatively high, as compared with standard dispersions.* On the other hand, we expect Bragg reflection arising from the regular arrangement of the spheres in an fcc lattice. The surface plasmon resonance is mainly an absorbance when the nanoparticle concentration is low enough and hardly contributes to reflectance for interparticle separations larger than 50 nm.[26] For this reason plasmon absorption is expected to be better observed during transmittance experiments.

The reflectance spectra shown in **Fig. 4.13** are basically identical to what would be expected for opals made of 225 nm pure silica spheres, and no sign of the gold cores is found. The Bragg peak spectral positions can be fitted with the equation given in section **4.3**. The 15 nm Au cores have not been included in the calculation, since they occupy less than 0.1% of each particle, and therefore their contribution to diffraction should be negligible. The specular reflectance spectra of **Fig. 4.13** simply show a red-shift of the maximum, due to an increase of the opal interstices refractive index. The progressive decrease of intensity and relative-width are a consequence of the optical contrast diminution between the spheres and

* Simple calculations performed assuming a perfect fcc packing (filling fraction equal to 74%) yield an estimate for the gold concentration in the sintered opals of ca.0.03 mol L^{-1}.

the background. The match point would be placed at an intermediate composition between 75% and 100% of glycerol, but closer to pure glycerol. This shows again that the presence of the metal cores does not visibly alter the diffraction properties of the opals.

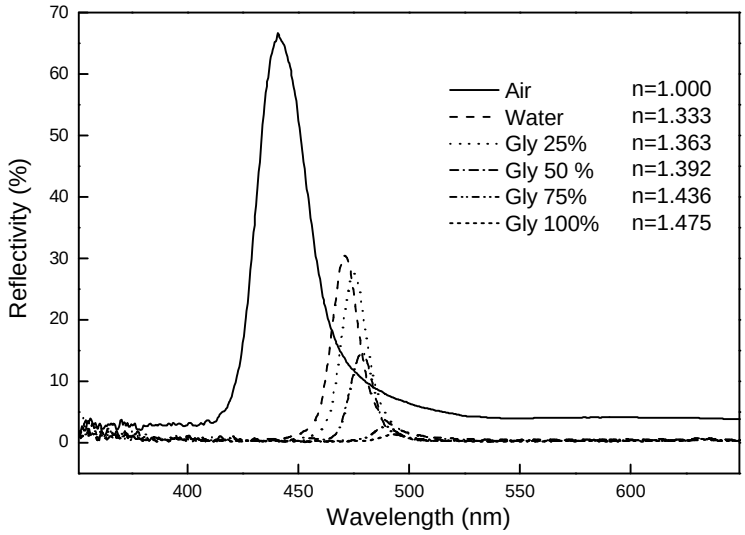

Fig. 4.13: Specular reflectance spectra in different media (air, water and water-glycerol mixtures) for sintered opals made of $Au@SiO_2$ particles with 15 nm core diameter and 225 nm total diameter. The corresponding void refractive indexes are given.

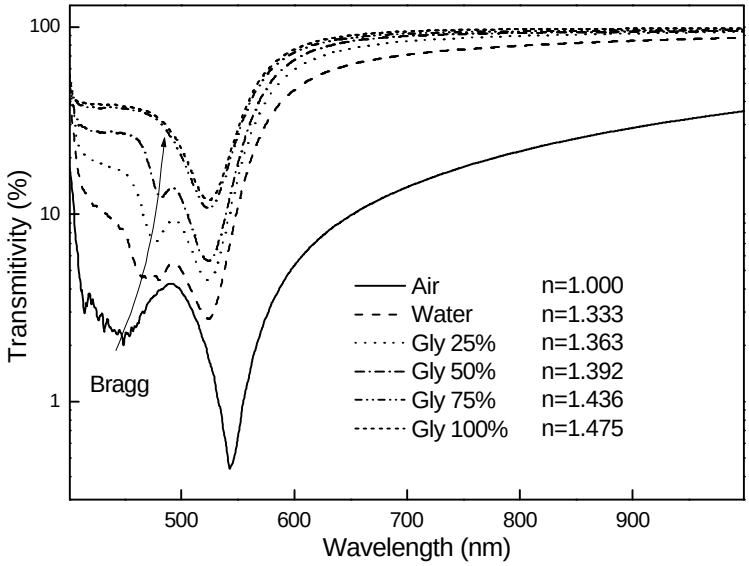

Fig. 4.14: Transmittance spectra in different media (air, water and water-glycerol mixtures) for sintered opals made of $Au@SiO_2$ particles with 15 nm core diameter and 225 nm total diameter. The corresponding void refractive indexes are given.

A richer description of the optical behavior is found in the transmittance spectra, where both the surface plasmon resonance and the Bragg diffraction are observed. Several features should be commented from the spectra of **Fig. 4.14**. With respect to the Bragg peaks, their positions basically coincide with those measured in reflectance, though for the samples with a low background refractive index the peaks are close to the lower wavelength detection limit of the instrument, and therefore appear noisy. It is also clear that the intensity of the Bragg peaks decreases when approaching the refractive index matching with silica, exactly as was observed in the reflectance spectra.

Regarding the plasmon band, invariance in its position can be seen for all the infiltrated samples. The bands are consistently centered at 523 nm, which agrees with the predictions for non-interacting nanoparticles dispersed in silica shown for thin films.[27] The silica shells are sufficiently thick, that gold cores do not "feel" the solvent anymore. However, the scattering gets reduced when the index matching point is approached, and therefore the global intensity of the spectra (including the plasmon band) decreases. The only sample that does not stick to this behavior is the dry, non-infiltrated opal, in which the plasmon band is noticeably red-shifted with respect to all the others (543 nm). Also, the transmittance is drastically reduced, which can be again attributed to a much stronger scattering, since the contrast between silica spheres and voids is also much larger than in all the infiltrated samples.

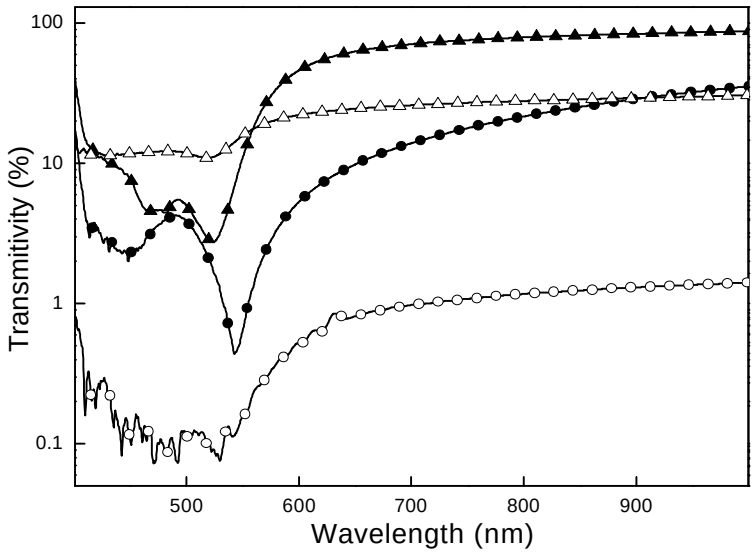

Fig. 4.15: Transmittance spectra in air (circles) and water (triangles) for opals (solid symbols) and disordered packings (open symbols) of $Au@SiO_2$ particles.

A further experiment was carried out to test the influence of order on the optical properties. To this end, a piece of the sintered opal was ground, so as to destroy the crystalline structure, and the transmittance was measured, both for the sample in air and after infiltration with water. The spectra obtained are shown in

Fig. 4.15, where spectra for the corresponding ordered samples are included for comparison. As expected, the strong scattering from the disordered sample in air renders the gold surface plasmon band hardly visible. In water, there is still a diffuse scattering contribution, but the plasmon band is clearly observed. In the case of the ordered samples, scattering is coherent (diffraction) and the effect on the plasmon band is only observed as a red-shift as explained above.

4.8 Summary.

4.8.1 Conclussions.

- Spectral position and width of the Bragg diffraction from the {111} planes in opals give information about lattice parameter, filling fraction, effective dielectric constant and crystal quality.
- Bragg's law is a good approximation for a first study of the pseudogap behavior of an opal around the ΓL direction when refractive indexes and their contrast are not high.
- Both the average and the Maxwell-Garnett equation give an accurate value for the effective dielectric constant when materials composing the opal have a low refractive index (<2.0). For higher refractive indexes the effective dielectric constant must be extracted from other methods such as a Plane Wave expansion.
- The increasing width of Bragg peaks with sphere diameter points out that the quality of colloidal crystals of silica spheres in water gets worse for larger spheres.
- Thin film opals number of layers can be calculated studying the Fabry-Perot fringes.
- Thin film opals allow the study of optical phenomena that cannot be observed in opals grown by other methods (evolution of optical properties with number of layers, diffraction pattern, Fabry-Perot fringes…)
- The optical properties of the opals made of silica spheres with a gold core are determined both by the Bragg diffraction inherent to the ordered structure, and by the surface plasmon absorption of the metal cores.
- Plasmon absorption band due to gold cores can be observed with transmission measurements while reflectance spectra only show the Bragg diffraction peaks.
- The position of the plasmon band is red-shifted in the dry opal, as compared to the isolated particles and to infiltrated opals, which seems to be due to a coupling with scattering.

4.8.2 Future research.

- Further research is needed to explain the red-shift of the plasmon absorption band in dry opals and confirm its relationship with scattering effects.
- Spheres with larger metallic cores must be synthesized and ordered in a fcc lattice to obtain a cPBG in the visible.

4.9 References.

1 Leung, K. M. & Liu, Y. F. Full Vector Wave Calculation of Photonic Band Structures in Face-Centered-Cubic Dielectric Media. *Phys. Rev. Lett.* **65**, 2646 (1990).

2 All the photonic band structures presented in this chapter have been calculated thanks to the code developed by S. Guo for *MatLab* 6.5. The code is available at: http://www.lions.odu.edu/~sguox002/.

3 Pusey, P. N. & van Megen, W. Phase-Behavior of Concentrated Suspensions of Nearly Hard Colloidal Spheres. *Nature* **320**, 340 (1986).

4 Hetch, E. & Zajac, A. Optics (Addison-Wesley 1974).

5 Hiltner, P. A. & Krieger, I. M. Diffraction of Light by Ordered Suspensions. *J. Phys. Chem.* **73**, 2386 (1969).

6 Sakoda, K. Optical Properties of Photonic Crystals (Springer-Verlag Berlin Heidelberg 2001).

7 J. C. M. Garnett, Philos. Trans. R. Soc. London 203, 385 (1904).

8 Datta, S., Chan, C. T., Ho, K. M. & Soukoulis, C. M. Effective Dielectric-Constant of Periodic Composite Structures. *Phys. Rev. B* **48**, 14936 (1993).

9 Bertone, J. F., Jiang, P., Hwang, K. S., Mittleman, D. M. & Colvin, V. L. Thickness dependence of the optical properties of ordered silica-air and air-polymer photonic crystals. *Phys. Rev. Lett.* **83**, 300 (1999).

10 Jiang, P., Bertone, J. F., Hwang, K. S. & Colvin, V. L. Single-crystal colloidal multilayers of controlled thickness. *Chem. Mat.* **11**, 2132 (1999).

11 Born, M. & Wolf, E. Principles of Optics (Pergamon Press 1986).

12 Stefanou, N., Yannopapas, V. & Modinos, A. Heterostructures of photonic crystals: frequency bands and transmission coefficients. *Comput. Phys. Commun.* **113**, 49 (1998).

13 Galisteo-López, J. F., Palacios-Lidón, E., Castillo-Martínez, E. & López, C. Optical study of the pseudogap in thickness and orientation controlled artificial opals. *Phys. Rev. B* **68**, 115109 (2003).

14 Amos, R. M., Rarity, J. G., Tapster, P. R., Shepherd, T. J. & Kitson, S. C. Fabrication of large-area face-centered-cubic hard-sphere colloidal crystals by shear alignment. *Phys. Rev. E* **61**, 2929 (2000).

15 Kreibig, U. & Vollmer, M. Optical Properties of Metal Clusters (Springer: Berlin, 1995).

16 Mulvaney, P. Surface plasmon spectroscopy of nanosized metal particles. *Langmuir* **12**, 788 (1996).

17 Link, S. & El-Sayed, M. A. Spectral properties and relaxation dynamics of surface plasmon electronic oscillations in gold and silver nanodots and nanorods. *J. Phys. Chem. B* **103**, 8410 (1999).

18 Moroz, A. Three-dimensional complete photonic-band-gap structures in the visible. *Phys. Rev. Lett.* **83**, 5274 (1999).

19 Moroz, A. Photonic crystals of coated metallic spheres. *Europhys. Lett.* **50**, 466 (2000).

20 Velev, O. D., Tessier, P. M., Lenhoff, A. M. & Kaler, E. W. Materials - A class of porous metallic nanostructures. *Nature* **401**, 548 (1999).

21 Tessier, P., Velev, O. D., Kalambur, A. T., Lenhoff, A. M., Rabolt, J. F. & Kaler, E. W. Structured metallic films for optical and spectroscopic applications via colloidal crystal templating. *Adv. Mater.* **13**, 396 (2001).

22 Jiang, P., Cizeron, J., Bertone, J. F. & Colvin, V. L. Preparation of macroporous metal films from colloidal crystals. *J. Am. Chem. Soc.* **121**, 7957 (1999).

23 Wijnhoven, J. E. G. J. *et al.* Electrochemical assembly of ordered macropores in gold. *Adv. Mater.* **12**, 888 (2000).

24 Graf, C. & van Blaaderen, A. Metallodielectric colloidal core-shell particles for photonic applications. *Langmuir* **18**, 524 (2002).

25 Liz-Marzán, L. M., Giersig, M. & Mulvaney, P. Synthesis of nanosized gold-silica core-shell particles. *Langmuir* **12**, 4329 (1996).

26 Ung, T., Liz-Marzán, L. M. & Mulvaney, P. Gold nanoparticle thin films. *Colloid Surf. A-Physicochem. Eng. Asp.* **202**, 119 (2002).

27 Ung, T., Liz-Marzán, L. M. & Mulvaney, P. Optical properties of thin films of Au@SiO2 particles. *J. Phys. Chem. B* **105**, 3441 (2001).

Chapter 5: Photonic Band Engineering in opals by Growth of Si/Ge Multilayer.

5.1 Introduction.

As was explained in Chapter 1, the fabrication of crystals with a cPBG in the NIR or VIS has been probably the most-wanted achievement by the researchers in this field. Works related with the infiltration of materials within opals were usually concerned with completely loading the opals since these structures were afterwards inverted to obtain a cPBG. For this reason little attention has been paid to incomplete infiltrations. However there is an increasing number of publications showing that photonic crystals without a cPBG may present interesting effects with many potential applications. The anomalous band dispersion effects observed[1] and predicted in 2D and 3D structures are a good example. Superprism effect (**Fig. 5.1 a**), all angle negative refraction[2] (**Fig. 5.1 b**), high group velocity dispersion[3] or the improvement of non linear optics effects are beautiful consequences of what can happen when light couples with the appropriated bands. Thus, smart engineering on the band structure becomes an important discipline.

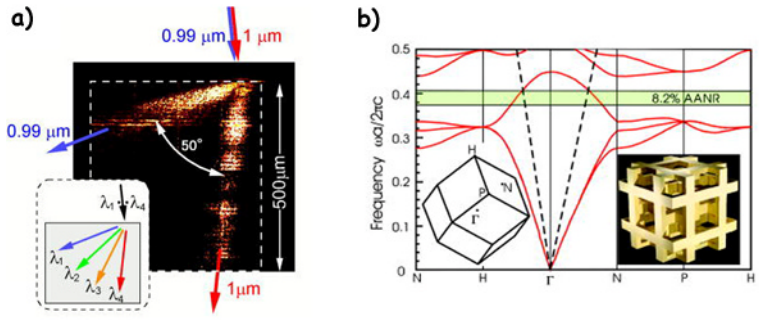

Fig. 5.1: a) The superprism effect observed by Kosaka *et al.* shows how two photons with very similar and parallel input wave vectors can follow very different paths within the Photonic Crystal (from Ref. 1). b) An appropriate design of the band structure may give rise to All Angle Negative Refraction effects (from Ref. 2).

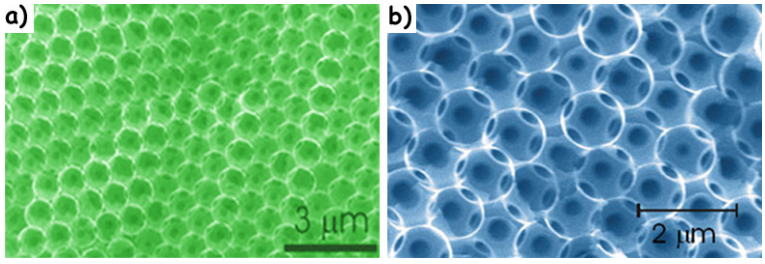

Fig. 5.2: Inverse opals of a) silicon (ref. 4) and b) germanium (ref. 5). These structures satisfy all the requirements to present a cPBG in the NIR.

In order to tailor the shape of a photonic band structure, a good choice of the lattice symmetry is important. Unfortunately, self assembly methods allow few variations since fcc structures of touching spheres are the most usual result. However, when it comes to band engineering, it must be taken into account that

photonic bands not only depend on the underlying lattice but on the primitive cell structure. So, accurate control of the materials composing an fcc crystal is a remaining tool for band engineering. The use of high refractive index semiconductors importantly affects band structure. Also, varying the topography would involve changes and therefore is, another tool to be considered.

The potential of silicon and germanium as materials for photonic applications has been well stated since the appearance of two works published by A. Blanco[4] and by H. Míguez[5] respectively (**Fig. 5.2**). For the first time they presented crystals (based on opals) accomplishing all the requirements to present a cPBG in the NIR. Apart from their high refractive indexes, both materials have a long established technological tradition.

In this chapter a method to accurately control the synthesis of these semiconductors, amorphous silicon and germanium, within thin silica opals will be described. Growth of semiconductor mono-layers or even multiple layers combining air, silicon and germanium will be presented. By means of this method it will be possible to modify the photonic properties of the opals. Optical spectra in accordance to theoretical calculations will be provided to support the statements.

To achieve the results presented here, thin silica opals were prepared by vertical deposition on silicon substrates. A reduced number of layers in these samples was not a problem since it has been shown that a low number of layers (>18) may be taken as an infinite crystal.[6] The samples were made of silica spheres of 660 nm of diameter. Domains were large enough to obtain good spectra from areas as large as 330 x 330 μm^2 (see Chapter 3).

Once the experimental procedures are explained, theoretical calculations will be presented to prove that the photonic band structure of the opals may be manipulated by means of these techniques.

5.2 Controlled growth of Silicon and Germanium by CVD.

Both amorphous semiconductors were synthesized by chemical vapor deposition (CVD) performing slight modifications over already published methods.[4,5] In this system, basically, the sample is placed in a cell where the precursor gas is condensed with liquid nitrogen. The precursor gases used in this work were disilane (Si_2H_6) for silicon and germane (GeH_4) for germanium. The former gas is explosive in the presence of air and the latter is poisonous as well. For this reason the whole system is previously subjected to high vacuum ($3x10^{-6}$ Torr) to avoid the presence of air. Once the precursor gas is condensed, the cell is isolated and placed in a furnace at the selected decomposition temperature.

5.2.1 Process optimization.

Essentially, two parameters will govern the growth of the semiconductor, namely, the precursor gas pressure and the temperature of decomposition. A low pressure presents important advantages. Firstly, it is safer in case of gas leaks and secondly, the waste of precursor gas is reduced. Therefore the precursor gas

pressure was set at 150 Torr for all the experiments. Decomposition temperature plays a very important role in two aspects: growth velocity and the presence of undesired particles. The higher the temperature is, the faster the precursor gas will decompose. As we are interested in controlling the amount of semiconductor loaded in the opals, low growth rates are needed. It has also been observed that high temperatures induce the growth of undesired particles. Due to their high refractive indexes, these particles severely affect the optical measurements making the spectra rather difficult to interpret. In the case of silicon the precursor gas decomposition temperature selected was 375ºC while for germane it was set at 270ºC. Lower temperatures resulted in very slow synthesis rates while higher ones allowed little degree of control. Indeed, as **Fig. 5.3 a** and **b** show, large spherical particles of silicon or tubular germanium wires grew on the sample surface. It is, however, noticeable the similarity existing between Fig 1b and the α-GeO_2 nanowires recently presented and studied by J-Q Hu *et al.*[7] These samples contrast with the clean surfaces of the resulting composites (**Fig. 5.3 c** and **d**) at the optimized temperatures.

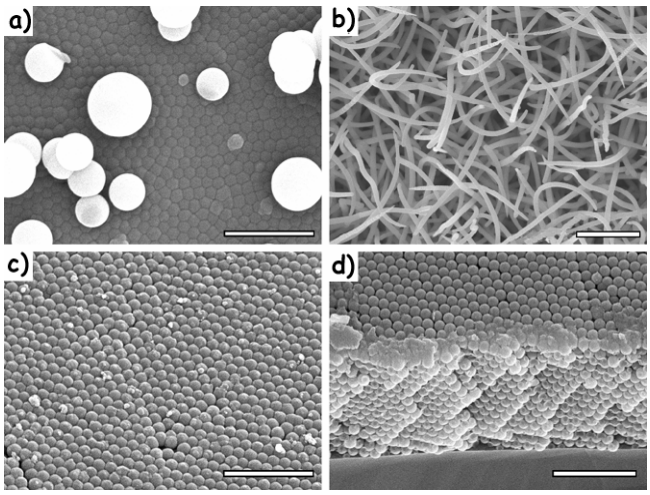

Fig. 5.3: Top images show unwanted particles in a) silicon (450ºC) and b) germanium (350º). This 'contamination' is drastically reduced at lower temperatures for c) silicon (375ºC) and d) germanium (270ºC). Opals are made from silica spheres of 660 nm of diameter. All scale bars are 5 microns.

5.2.2 Experimental results and optical data interpretation.

For silicon and germanium, these being semiconductors with a very high refractive index, optical measurements will be the best method to keep track of the opals infiltration. Samples are oriented so that {111} planes are parallel to the surface of the substrate. Therefore, the wavelength at which the first pseudogap in the Γ-L direction is observed will provide the necessary information to know the amount of loaded semiconductor.

Electron microscope images show that the growth of these semiconductors takes place in a layered manner.[8] This fact has especial relevance when theoretical

calculations are performed. A very easy and widespread method to calculate the amount of material loaded in the opal relies on applying Bragg's law. In this method it is assumed that the opal is fully loaded with a material with a dielectric constant equal to the average of air and semiconductor present in the pores. In other words, the effective dielectric constant in the pores is calculated as the average of the composing materials (air and semiconductor). However, this method is not very accurate for layered growths. Indeed, the effect of a sharp boundary between air and semiconductor on photons can not be neglected, especially when the semiconductor has a high refractive index. In this case it is much better to compare the experimental results to the photonic band structure obtained by theoretical calculations performed with a plane wave method that takes into account the real symmetry of the primitive cell.[9]

To obtain the photonic band structure the relationship between the amount of layered material loaded in the crystal and its thickness must be calculated beforehand. Analytical expressions can be obtained for low infilling ratios but they get more and more complicated as this ratio is increased. A Montecarlo calculation for an fcc structure shows this relationship in **Fig. 5.4**.

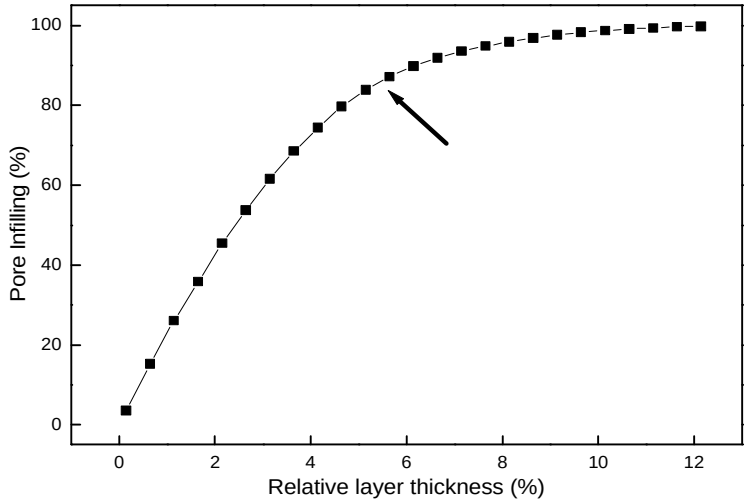

Fig. 5.4: Semiconductor layer thickness dependence of filling fraction for an fcc. Layer thickness is relative to lattice parameter and shown as a percentage. The arrow points at the value where the {111} plane pores are closed.

The width and position of the first stop band in the Γ-L direction were calculated for both semiconductors. The refractive index values used for SiO_2, Si and Ge were: 1.43,[10] 3.80[11] and 4.10[11] respectively. On the other hand, to obtain the experimental spectra, light was collected at normal incidence with respect to the {111} planes. A 4X objective with a numerical aperture of 0.10 was used to focus and collect the light.

Fig. 5.5 and **Fig. 5.6** show the experimental data and theoretical calculations for silicon and germanium respectively. In these spectra we can observe the

diffraction peak caused by the first pseudogap, the Fabry-Perot fringes due to the finite thickness of the sample and other reflection peaks associated with various other photonic bands. Apart from the percentage of loaded semiconductor some other information can be deduced from the spectra. From the Fabry-Perot fringes thickness of the sample can be extracted. Thin opals were typically made of 14-16 layers, having a final thickness of 13-15 microns. The right panel in both figures summarizes positions and peak widths of the first pseudogap extracted from reflectance spectra as in the left panels. For low semiconductor filling fraction full width at half maximum (FWHM) decreases with increasing infiltration and then increases again for further loading. The pseudogap almost closes for a 20 % of silicon in the pores and 15 % in the case of germanium. We shall refer to this percentage as index matching infilling value (IMIV). This is the result of matching the effective refractive index of the pore (air plus semiconductor) and the silica spheres.[8] It is important to mention that the effective refractive index of the pore differs from the average value. The former can be extracted from Bragg's law at the L point: $n_{eff}=(\sqrt{3}/2)/(a/l)$, and for IMIV a/l is around 0.60 and $n_{eff}\cong 1.44$ (very close to that of silica spheres). The values obtained for an average refractive index will be higher ($\cong 1.75$). FWHM of the experimental Bragg diffraction peaks is compared with theoretical expectations in right panel of both figures. The agreement is fairly good.

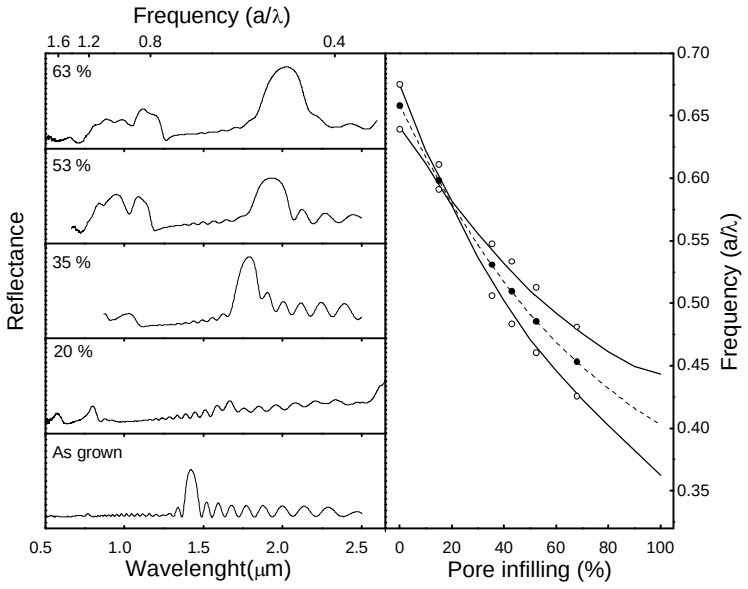

Fig. 5.5: Left panels show the reflectance spectra of the samples loaded with different amounts of Si for opals of 660 nm diameter spheres. The right panel shows the centre (full circles) and edges (open circles) of the first pseudo-gap in the (111) direction as a function of germanium layer thickness along with the theoretical calculations (lines). Frequency units are normalized to the lattice parameter.

Around the first pseudogap the wavelength involved is close to the lattice parameter for which reason the sample is viewed as a uniform medium and Fabry-

Perot fringes show up. (The features of the fringes are determined by sample thickness and effective refractive index). This is much more so near IMIV, where any contrast in the system is washed out making the samples behave as a thoroughly homogeneous thin film. Here, the Bragg reflectance peak will be indistinguishable from the rest of the fringes. It is, however, interesting to notice that even at IMIV the sample crystalline nature can be probed by shorter wavelengths as seen at higher energies. Indeed, although the spectra show that the first pseudogap has almost disappeared, some structure related to the 5th to 9th bands can be observed.

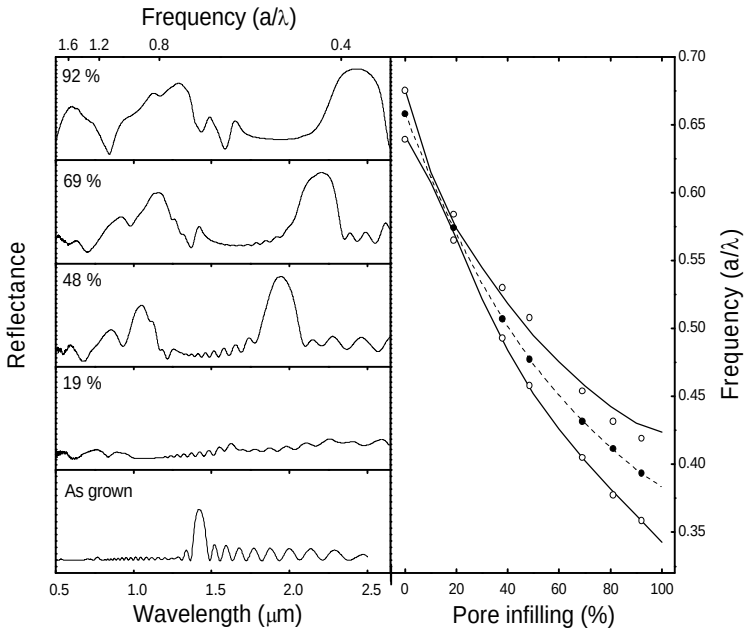

Fig. 5.6: Left panels show the reflectance spectra of the samples loaded with different amounts of Ge for opals of 660 nm diameter spheres. The right panel shows the centre (full circles) and edges (open circles) of the first pseudo-gap in the (111) direction as a function of germanium layer thickness along with the theoretical calculations (lines). Frequency units are normalized to the lattice parameter.

The key parameter to control the amount of semiconductor loaded in the opals is reaction time. This is the time the sample remains at a certain temperature at which the decomposition of the precursor gas takes place. **Fig. 5.7** summarizes the percentage of pore loaded with silicon or germanium as a function of synthesis time. It is important to mention that time lengths are quite reasonable since layer thickness variations of only a few nanometers may be achieved with just several minutes differences. Under these experimental conditions, it can be seen that, for a single reaction, silicon reaches a maximum at approximately 53% of pore infilling (24 nm of layer thickness for opals made of 660 nm silica spheres). In the case of germanium, the pore can be loaded without saturation. Pressure built up by hydrogen production is a limiting factor since it will inhibit the synthesis of the

semiconductor. This factor is more important for silicon since synthesis temperature is 105ºC higher than for germanium and that involves a higher hydrogen pressure. This is probably the reason for such a saturation curve in silicon growth. Another difference clearly appreciable is that germanium growth is rather slow at the beginning of the process when compared with silicon. The temperature at which germanium is grown is very close to the decomposition temperature of GeH_4. This transformation begins with the formation of GeH_2 species.[12] At such a low temperature, the activation energy needed to complete the first step delays the final reaction as can be observed in **Fig. 5.7**.

As a result, silicon, as opposite to germanium, will need further cycles to obtain higher filling fractions. The only limitation for complete infillings seems to be a geometrical one related to the closure of the pores in the {111} close packed planes. This happens for a grown layer of thickness equal to the 5.47% of the lattice constant (corresponding to an 86% infilling, see **Fig. 5.4**).[13] Of course, this top limit is valid for defect free samples. Polydispersity in spheres diameter and vacancies may lead to exceeding this value. This explains why filling ratios close to 100% have been reported.[4]

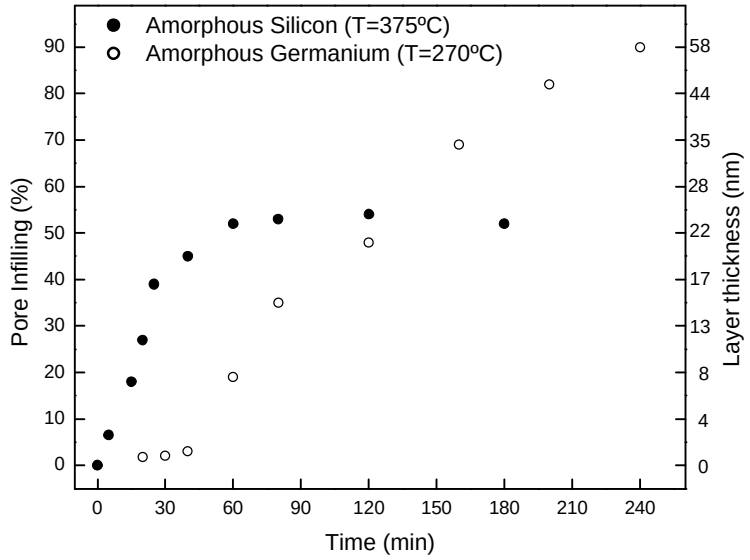

Fig. 5.7: Infilling as a function of single reaction times. Si (full circles) is formed at 375ºC and Ge (open circles) at 270ºC. Silica spheres of 660 nm of diameter are used.

5.3 Multilayer structures.

With this degree of control over the silicon and germanium synthesis the growth of multilayer structures can be tackled. This method allows not only growing both materials on silica but either on the other, as will be shown shortly. A further degree of freedom will be provided by the selectivity of different solvents that can be used to remove some of the materials. *Aqua regia* (a [3:1] mixture of

hydrochloric and nitric acid) can selectively remove germanium damaging neither the silica spheres nor the silicon layer. Furthermore, germanium can be oxidized at 500ºC without changing the properties of the rest of materials: silica spheres remain unaffected and higher temperatures are required for silicon oxidation.

5.3.1 Si/Ge/Air multilayer.

To test the possibility of growing a semiconductor multilayer, a sample with a 30% of the pore loaded with germanium was re-grown with silicon up to the 80%. Then, germanium was etched with *aqua regia*. **Fig. 5.8** shows an electron microscope picture of the resulting structure after etching. The silicon network is interconnected and fixed to the substrate and remains separate from the spheres by the air layer. **Fig. 5.9 a** shows a diagram with the necessary steps to obtain this structure.

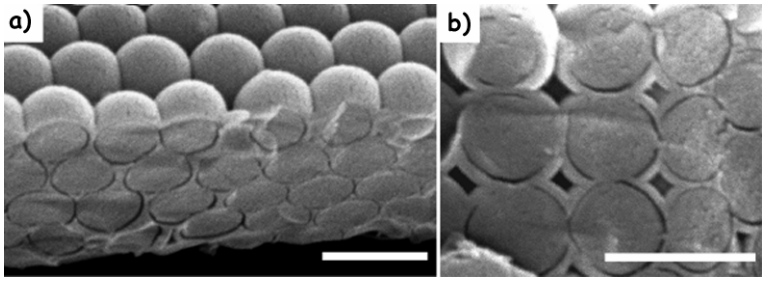

Fig. 5.8: Cleaved edge SEM images of a doubly connected structure. The pictures show a a) {111} plane and a b) {100} plane. The continuous Si layer is separated from the continuous silica structure by an air shell. The dark lines in the cleaved edge are the air gaps between Si shell and the silica spheres. Scale bars are 1 micron.

A more complicated structure was fabricated and optically characterized. First a sample was loaded with Si up to 20% of the pore, then a layer of Ge to complete 45% and finally Si to a 60%. At this point the composite presents the following composition: SiO_2(74%)-Si(5.2%)-Ge(6.5%)-Si(3.9%); percentages representing the total volume fraction of each material and a 10.4% air remaining. This sample was then dipped in *aqua regia* for 60 minutes. The outcome is two homogeneous Si shells separated by an air gap, the inner shell being connected to the silica spheres. The process is schematically shown in **Fig. 5.9 b**.

Fig. 5.10 shows the reflectance spectra evolution at different stages. The bare opal (**Fig. 5.10 a**) is loaded with silicon (**Fig. 5.10 b**) up to a value close to the IMIV. The first pseudogap all but disappears while higher energy features become clearer. Further loading with germanium (**Fig. 5.10 c**) raises the first pseudogap and increases reflectance peaks width. A new layer of silicon (**Fig. 5.10 d**) further red-shifts and widens photonic features. At this point, germanium begins to be etched. Before it is completely removed, spectra collect information from areas with and without germanium at the same time. Both diffraction peaks corresponding to the first pseudogap of each case appear in the spectrum at 2.22 μm and 1.85 μm respectively (**Fig. 5.10 e**). After the etching was completed in 60 minutes (**Fig. 5.10 f**) the peak at 2.22 μm has completely disappeared.

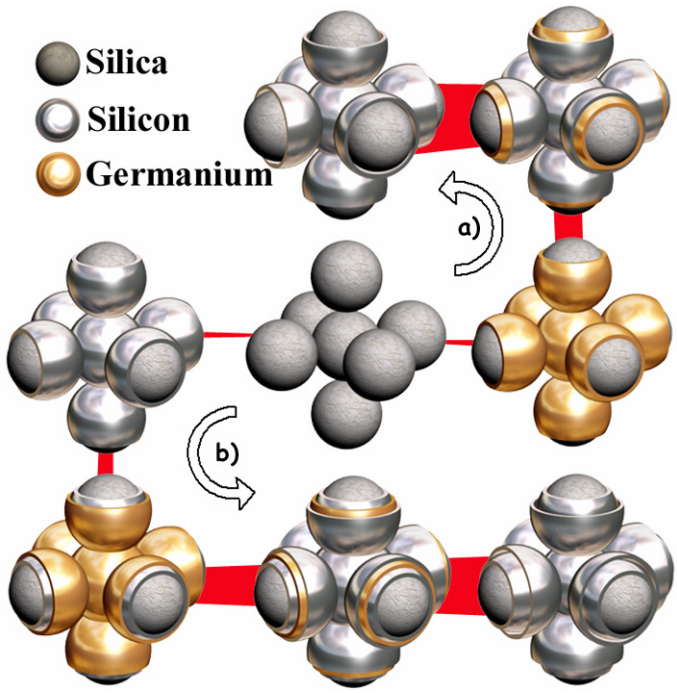

Fig. 5.9: Diagram showing the formation of multilayer systems. Beginning with a bare opal, subsequent growth of semiconductor layers and final selective removal of germanium may give rise to air gaps a) between the silica spheres and silicon or b) between two silicon layers.

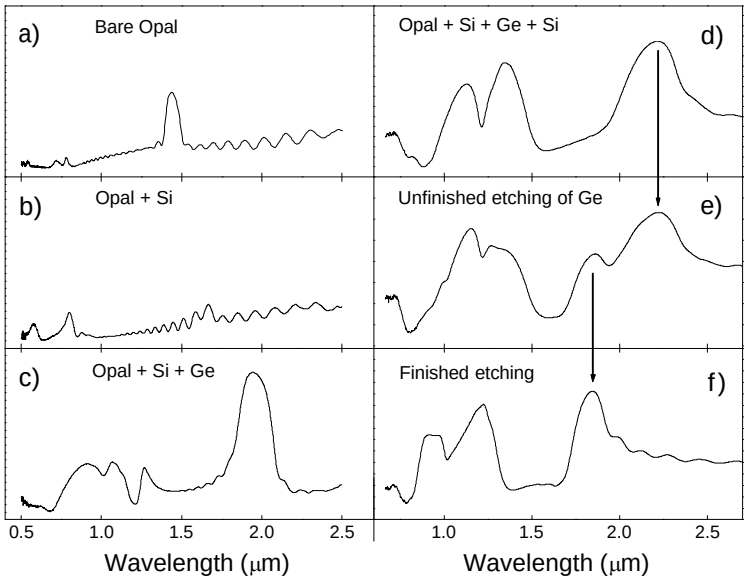

Fig. 5.10: Reflectance spectra of a sample after successive semiconductors infilling and etching. a) Bare opal; b) a Si layer is grown; c) a second layer of Ge and d) a third layer of Si; e) partial etching of the Ge; f) etching is completed and regions with a pseudogap at 2.22 μm disappear.

5.3.2 Other possible materials for multilayer growth.

At this point the possibility of growing multilayer systems of silicon, germanium and or air has been proved. However there are many other possibilities available. For example germanium can be oxidized to obtain germanium dioxide (GeO_2) at 500ºC. Optical spectra of an opal loaded with germanium and then oxidized are shown in **Fig. 5.11**. This temperature is too low for silicon oxidation or producing any change in silica spheres. For this reason the oxidation of germanium can be regarded as a selective process in these systems. However, it must be taken into account that for layers of germanium above ~10 nm it may become rather difficult to oxidize the entire semiconductor. If larger amounts are to be oxidized, it may be advisable to do more than one cycle of germanium growing and oxidation. The refractive index of this material is approximately 1.60.

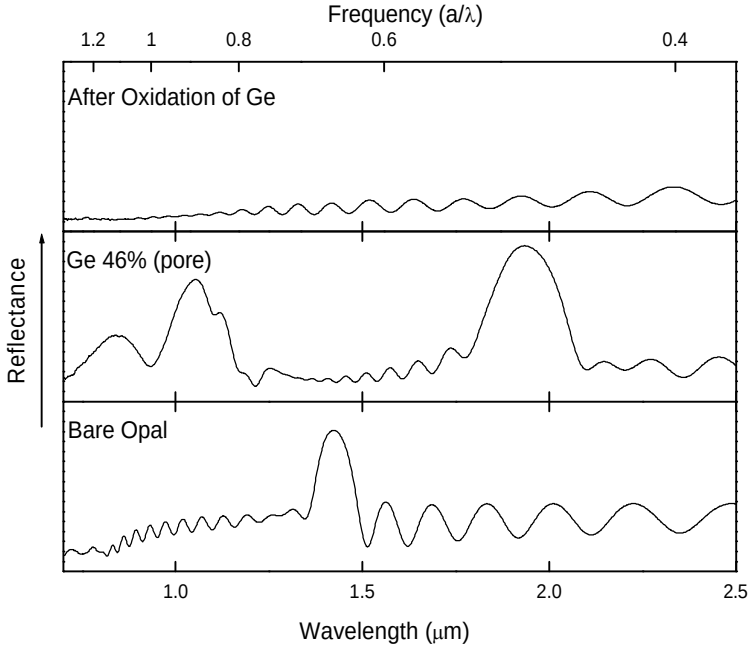

Fig. 5.11: Optical spectra of a sample where 46% of the available pore volume was loaded with germanium. The top graph shows the optical data after the sample has been oxidized at 500ºC. The oxide in the pore (together with possible remains of Ge) fit the IMIV so that no stop-band can be differenced from the Fabry-Perot fringes.

Apart from the materials that can be grown directly or indirectly with a CVD system, other materials that grow in a layered way may be added to increase the number of possibilities. As an example of a compatible method, H. Míguez *et al.* developed a new technique to directly grow silica by CVD at room temperature and atmospheric pressure.[13] Such a technique can be used to interpenetrate the spheres and strength the sample.

Yet another tool is hydrofluoric acid (HF), which can selectively remove both oxides (GeO_2 and SiO_2).

5.4 Engineering on the Photonic Band Structure.

Although limited by the fact that symmetries other than fcc are very difficult to obtain since self-assembly gives rise to fcc lattices, engineering on the photonic band structure is still possible. Indeed, subtle variations in topography or refractive index contrast may lead to very interesting band structures.

5.4.1 First Stop-Band behavior.

In this section the behavior of the first pseudogap in three of the highest symmetry points (of an fcc lattice) is studied as a function of different infilling ratios of germanium. Qualitatively, silicon presents a similar behavior.

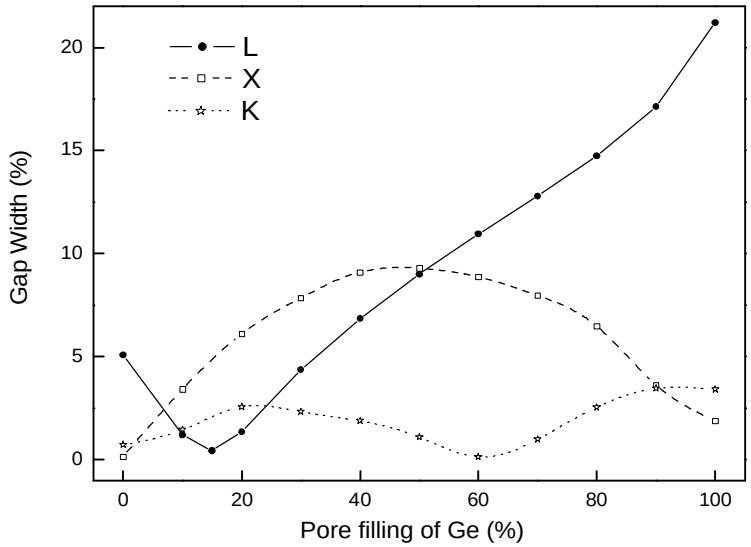

Fig. 5.12: Theoretical calculations of the first pseudogap behavior in three different points of an fcc lattice: L (normal to the {111} planes), X (normal to the {100} planes) and K (normal to the {110} planes).

Fig. 5.12 shows the theoretical predictions for the gap width (gap to midgap ratio) at three important points in the Brillouin zone. The L pseudogap width firstly decreases for initial infiltrations, almost closing at 17%, and then increases again after further loading of semiconductor. This agrees with the experimental results shown in **Fig. 5.6** where for low infilling ratios (around 20%) the pseudogap was too narrow to be distinguished from the Fabry-Perot fringes. In the case of the X point, the pseudogap is closed for bare opals. However when 50% of the available pore volume is loaded with germanium, a wide stop-band is predicted by theory. This gap closes again, although not completely, when pores are fully loaded. Finally, the Γ-K stop-band width varies increasing and decreasing for different infilling ratios.

Some researchers have shown fcc structures that were grown along the (100) direction.[14,15] However, optical measurements of the first pseudogap in this

direction were rarely provided. The probable reason is that in this direction when the opal is bare or fully loaded with a material, the pseudogap is closed or very narrow. The results of this section show that a layered growth to load 50% of the available pore volume should help to observe the pseudogap in this direction.

5.4.2 Flat bands.

Within a photonic crystal the group velocity (v_g) of photons will depend on the band to which these photons are coupled. The value of v_g will be proportional to the derivative of the band with respect to the wave-vector **k**. Photons coupled to flat bands will propagate through the crystal with very slow v_g. As v_g is inversely proportional to the effective refractive index, photons will "see" a medium with a very high refractive index.

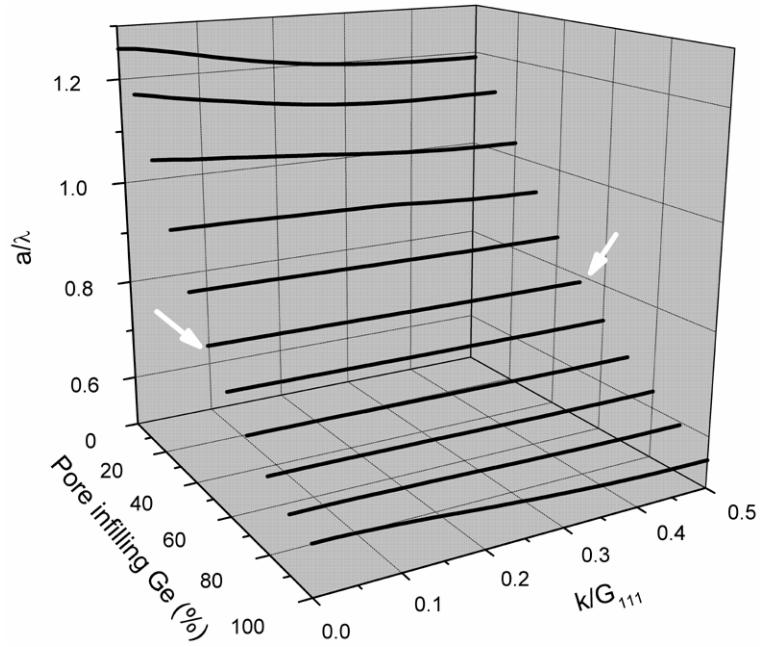

Fig. 5.13: Fifth band behaviour in the Γ-L direction for different infilling germanium ratios. For infillings around the 50%-60% the band becomes very flat. For very high infillings the shape becomes curved again. Arrows point at the band for a 50% of available pore volume loaded with germanium.

Materials in which light propagates with a low v_g are important for non linear (NL) optics. If a photonic crystal with flat bands is made from a NL active material photons would "stay longer within the crystal" and the efficiency of the NL material would be much increased. If photons of different frequencies couple to bands of unlike curvature, the photonic crystal will present high group velocity dispersion. This is an appealing phenomenon that has attracted the interest of several researchers in the last few years.[3]

Theoretical calculations show how controlled growth of semiconductor may vary the shape of photonic bands. Specifically, the fifth band in the Γ-L direction

may become very flat when the opal is loaded with germanium (same is true for silicon) around 50% of the available pore volume. **Fig. 5.13** shows how the fifth band shape gradually changes from curved to flat and curved again as the opal is loaded with germanium.

5.4.3 Structure with a doble complete Photonic Band Gap.

In 1998, K. Busch *et al.*[16] showed that slight variations in the topography of the inverse opals of silicon could lead to important enlargements of the cPBG between the 8th and 9th band. They considered separately the effect of air spheres interpenetration and that of incomplete loads of the pore volume.

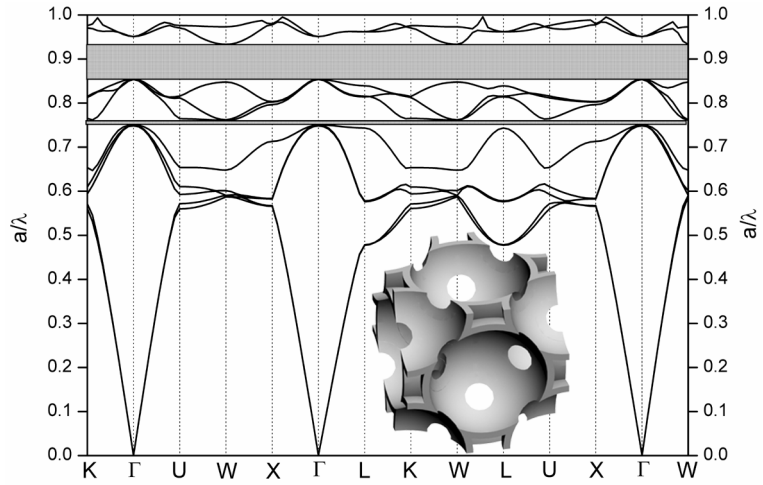

Fig. 5.14: Photonic band diagram of interpenetrating air spheres coated with amorphous Ge (n=4.1) in a fcc lattice. The radius of the air spheres is 0.3645a and the external radius of the semiconductor shell is 0.409a. Two gaps are developed: one between the 5th and 6th and another between the 8th and the 9th. The inset shows the corresponding real space structure.

Here the joint effects of air sphere interpenetration and incomplete semiconductor (Ge in this case) load are taken into account. This four-step process illustrates a particular case where the multilayer technique may be applied to tailor the photonic bands. First, an opal is loaded with Ge to a 25% of the available volume, followed by its oxidation. A further Ge load completes 86% of the initially available volume. Finally the oxides (GeO_2 and SiO_2) are removed with HF. The corresponding photonic band structure is shown in **Fig. 5.14**. Two cPBG open now: a larger one (12.6%) between the 8th and 9th bands and a narrower one (1.3%) between the 5th and the 6th bands. The latter is an interesting case that only very recently has been reported for fcc-based structures.[17] The method could be simplified if SiO_2 CVD was used instead of growing germanium and then oxidizing it.

5.5 Summary.

5.5.1 Conclusions.

- The optimization of the procedure to grow accurate amounts of silicon and germanium by CVD free of contamination in opals has been performed.
- The samples have been optically characterized and results agree with theoretical calculations of band structures.
- Multilayer systems of both semiconductors have been fabricated. Samples have been optically characterized and observed with a scanning electron microscope.
- Selective removal of germanium with *aqua regia* has proven to be possible.
- Theoretical calculations show that subtle variations of the topography may give rise to important effects (flat bands, pseudogaps openings, wide cPBGs…)
- A photonic band structure with a cPBG between the 5^{th} and 6^{th} band has been provided and the method to obtain it has been explained.

5.5.2 Future research.

It would be impossible to discuss all the possible structures that could be obtained from samples with different number of layers and materials forming them. However, there are many interesting possibilities that could be studied in a relatively straightforward manner.

- Study of the flat bands effect on light propagation.
- Study of the formation of high energy bands with the controlled infilling of silicon and germanium.
- Fabrication of a sample with a double cPBG as shown in section 5.4.3.
- A mapping of the cPBGs formation when air sphere interpenetration and semiconductor infilling ratios are varied.
- Including other materials grown by CVD to this technique.

5.6 References.

1 Kosaka, H. *et al.* Photonic crystals for micro lightwave circuits using wavelength-dependent angular beam steering. *Appl. Phys. Lett.* **74**, 1370 (1999).

2 Luo, C. Y., Johnson, S. G. & Joannopoulos, J. D. All-angle negative refraction in a three-dimensionally periodic photonic crystal. *Appl. Phys. Lett.* **81**, 2352 (2002).

3 Notomi, M. *et al.* Extremely large group-velocity dispersion of line-defect waveguides in photonic crystal slabs. *Phys. Rev. Lett.* **8725**, 253902 (2001).

4 Blanco, A. *et al.* Large-scale synthesis of a silicon photonic crystal with a complete three-dimensional bandgap near 1.5 micrometres. *Nature* **405**, 437 (2000).

5 Miguez, H. *et al.* Photonic bandgap engineering in germanium inverse opals by chemical vapor deposition. *Adv. Mater.* **13**, 1634 (2001).

6 Bertone, J. F., Jiang, P., Hwang, K. S., Mittleman, D. M. & Colvin, V. L. Thickness dependence of the optical properties of ordered silica-air and air-polymer photonic crystals. *Phys. Rev. Lett.* **83**, 300 (1999).

7 Hu, J. Q., Li, Q., Meng, X. M., Lee, C. S. & Lee, S. T. Synthesis and nanostructuring of patterned wires of alpha-GeO_2 by thermal oxidation. *Adv. Mater.* **14**, 1396 (2002).

8 Blanco, A. *et al.* Photonic band gap properties of CdS-in-opal systems. *Appl. Phys. Lett.* **78**, 3181 (2001).

9 The eigenstates are computed using a plane wave basis in an iterative implementation as described in Johnson, S. G. & Joannopoulos, J. D. Block-iterative frequency-domain methods for Maxwell's equations in a planewave basis. *Opt. Express* **8**, 173 (2001). MIT Photonic-Bands (MPB) package v-013.

10 Garcia-Santamaria, F., Miguez, H., Ibisate, M., Meseguer, F. & Lopez, C. Refractive index properties of calcined silica submicrometer spheres. *Langmuir* **18**, 1942 (2002).

11 Landolt-Börnstein: Numerical Data and Functional Relationships in Science and Technology, Vol. III/17 a (O. Madelung, Springer, Berlin 1982).

12 Chambreau, S. D. & Zhang, J. S. GeH_x (x=0-3) and Ge_nH_x (n=2-7) in flash pyrolysis of GeH_4. *Chem. Phys. Lett.* **351**, 171 (2002).

13 Miguez, H. *et al.* Mechanical stability enhancement by pore size and connectivity control in colloidal crystals by layer-by-layer growth of oxide. *Chem. Commun.*, 2736 (2002).

14 vanBlaaderen, A., Ruel, R. & Wiltzius, P. Template-directed colloidal crystallization. *Nature* **385**, 321 (1997).

15 Yin, Y., Li, Z. Y. & Xia, Y. Template-directed growth of (100)-oriented colloidal crystals. *Langmuir* **19**, 622 (2003).

16 Busch, K. & John, S. Photonic band gap formation in certain self-organizing systems. Phys. Rev. E 58, 3896 (1998).

17 Dong, W. T., Bongard, H., Tesche, B. & Marlow, F. Inverse opals with a skeleton structure: Photonic crystals with two complete bandgaps. *Adv. Mater.* **14**, 1457 (2002).

Chapter 6: Diamond lattice made of silica microspheres.

6.1 Introduction.

As explained in Chapter 1, inverse opals may present a cPBG between the 8th and 9th band when the refractive index contrast (*d*) is above 2.8 (see **Fig. 6.1 a**). However, optical features at high energies are strongly affected by the presence of defects and gaps are said to be "weak". Indeed, the cPBG present in fcc structures is very sensitive to the non-uniformity in crystals.[1] Defects such as diameter variations of the air spheres will significantly reduce the gap and may eventually close it. Summarizing, the high *d* value required to give rise to the cPBG and its fragility makes the fcc structure a non altogether ideal candidate.

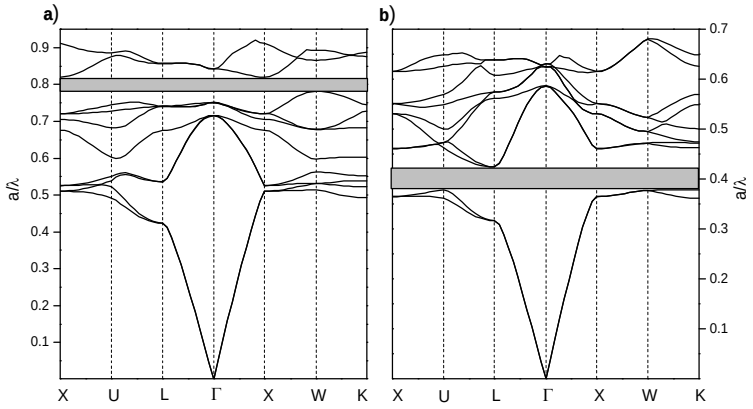

Fig. 6.1: Photonic band structures of a) close-packed fcc arrangement of touching air spheres (ff=74%) in silicon and b) diamond lattice of interpenetrated (ff=50%) air spheres in silicon.

A gap at lower bands would be desirable. However, the symmetry-induced degeneracy at the W point prevents the formation of a cPBG between the 2nd and 3rd bands for the fcc lattice. This degeneracy could disappear if the primitive cell symmetry was changed while keeping the same Brillouin zone. Soukoulis *et al*[2] showed that dielectric spheres arranged in the diamond lattice provides this symmetry change and shows the desired behavior since it possesses a cPBG between the 2nd and 3rd bands (see **Fig. 6.1 b**). Diamond structures of interpenetrated air spheres may show a wide and robust low energy cPBG. Furthermore, the required minimum *d* value is reduced to 2.0.

In terms of cPBG formation, diamond lattice present nothing but advantages over the fcc structure (**Table 6-1**). Unfortunately the construction of these structures has proven to be extremely difficult by self-assembly methods. Unlike fcc arrangements, this structure is not stable enough to self-assemble. For this reason, up to the publication of this work, only lithographic methods have succeeded to obtain 3D structures with this symmetry in the optical regime.[3,4]

In this chapter a method based on robot-aided micromanipulation[5,6] will be presented. It opens the possibility of building up 3D photonic crystals with

diamond structure (15 microns in size typically). Robot-aided manipulation of single microspheres on a template substrate allows assembling a body centered cubic (bcc) lattice, which in fact, is the combination of two diamond structures. The experimental results obtained after the application of these techniques will be presented as well.

	Diamond	fcc
Gap position	2^{nd}-3^{rd} bands	8^{th}-9^{th} bands
Required RI contrast	2.0	2.8
Other	Wide and robust cPBG	Narrow and weak cPBG

Table 6-1: Main differences in terms of cPBG formation for two lattice configurations: Diamond and fcc.

6.2 The idea.

To date, fabrication of a diamond structure made of micrometric spheres by self-assembly methods has not been possible, therefore, developing alternative routes is necessary. In this section the main features of the method that has been developed to obtain a diamond lattice in two different orientations will be described. The method takes advantage of concepts and disciplines such as colloids, robotics, epitaxial growth, plasma etching and photolithography.

6.2.1 Instability of the diamond lattice.

As fcc lattices of micrometric spheres are easily obtained it is natural to wonder which is the reason that makes it so difficult to fabricate a diamond arrangement. When the positions of the "atoms" are studied, it can be observed that, contrary to fcc, diamond structure positions are unstable.

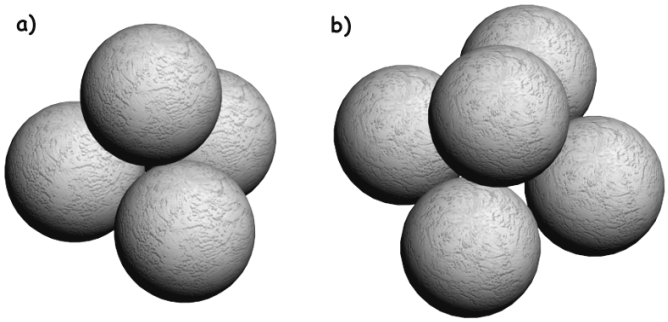

Fig. 6.2: Pictures showing the stable spheres disposition for an fcc structure in the a) (111) direction and the b) (001) direction.

As can be observed in **Fig. 6.2** spheres occupy stable positions (absolute minima energy locations) for fcc stuctures. In the case of {111} planes, each sphere is supported by three spheres of the layer underneath. For {001} planes the number

of supporting spheres is increased to four. Coversely, some spheres in the diamond structure are placed in very unstable locations. In the case of {111} planes (**Fig. 6.3 a**) the spheres of the second layer are supported by three spheres which is, again, stable. However, the next layer must be placed exactly on top of the second; obviously not a very stable position. The stability of {001} planes (**Fig. 6.3 a**) is not much better since spheres are supported just by two of the layer beneath (**Fig. 6.3 b**).

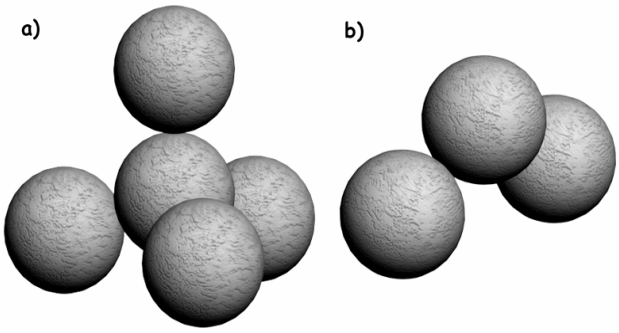

Fig. 6.3: Pictures showing the instable spheres disposition for an diamond structure in the a) (111) direction and the b) (001) direction.

Together with a low stability, diamond structures of touching spheres have a very reduced filling fraction. Indeed the amount of material is a 34% in contrast with 74% for fcc lattices. The diamond structure is therefore much less compact than the fcc as shown in **Fig. 6.4**.

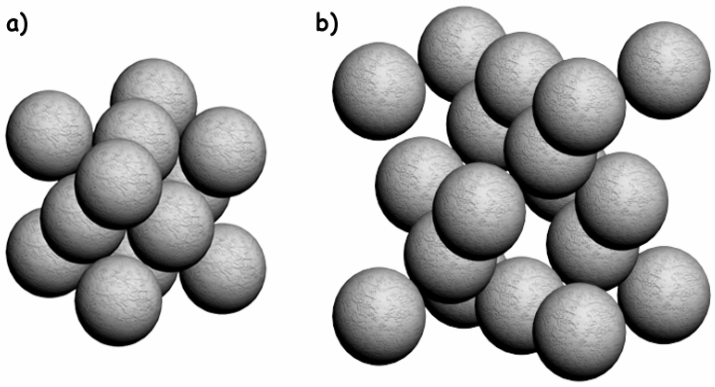

Fig. 6.4: Primitice cells of an a) fcc lattice and a b) diamond structure.

6.2.2 The mixed body centered cubic lattice.

Since self-assembly methods are not effective for diamond structures a technique in which the positions of the spheres can be selected must be used. In this sense a nanorobot (described in the experimental section) that allows to arrange the spheres one by one turns out to be a valid tool. However, even with a nanorobot, the direct construction of a diamond lattice is not possible because

positions of the microspheres must be at energy minima. Since this condition is not fulfilled by the diamond structure, the use of a sacrificial scaffold is needed.

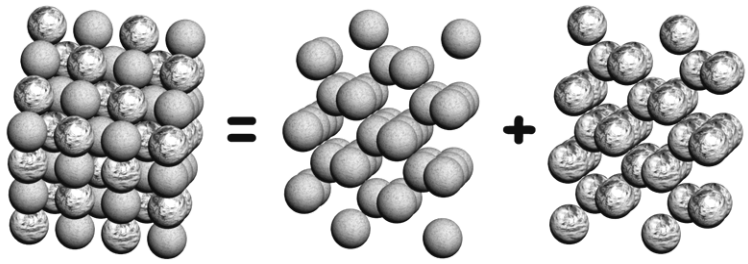

Fig. 6.5: A bcc lattice can be regarded as the sum of two diamond lattices. A bcc structure made of two kinds of spheres (e.g. organic and inorganic) each one forming diamond like arrangements is defined as a mixed bcc (mbcc).

It is well known that a body centered cubic (bcc) lattice can be regarded as the sum of two diamond lattices (see **Fig. 6.5**). The crucial point at this moment is designing a way in which the right atoms from the bcc structure can be removed in order that the remaining ones are arranged in the sought for diamond structure. A solution is provided if sacrificial atoms are of a class, in some sense (chemically), different from the other atoms thus providing a means for their dissolution. This can be done with inorganic vs. organic microspheres arranged in the points of a position of a bcc lattice. So the method starts with the construction, of a heterogeneous structure of mixed inorganic and organic (e.g. silica or silicon and latex) spheres in a bcc lattice. This structure, composed of two kinds of spheres, will be called, from now on, mixed body centered cubic (mbcc) although it must be realized that the actual lattice is an fcc with a two-atom basis. Subsequently, upon selective removal of the organic particles a diamond structure of the inorganic ones is obtained.

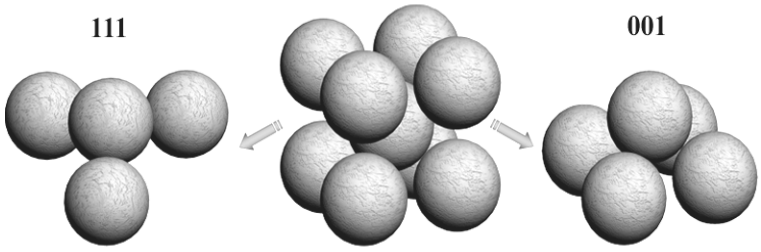

Fig. 6.6: The bcc lattice (center). The positions of spheres when growing in the (111) direction (left) or the (001) direction (right) are both stable.

The construction of an mbcc lattice as an intermediate step presents some advantages over direct diamond lattice assembly. The mbcc lattice allows stacking spheres along, at least, two orientations: (001) and (111). As **Fig. 6.6** shows, in both cases sphere positions are minimum energy locations once the first layer is in place. In either case the initial layer should be ordered on a template.

6.2.2.1 Algebraic description of the mbcc lattice.

In order to algebraically describe the lattices let summarize: a two interpenetrated diamond structures form a bcc that can be represented as an fcc with a four-atom basis. This choice is based on the fact that the most convenient description of a diamond structure is as an fcc with a two-vector basis. The mbcc will be presented too as an fcc with two two-atom bases made of different materials: e.g. inorganic (*i*) and organic (*o)*. The fcc primitive vectors are:

$$\mathbf{a_1}=a/2(1,1,0);\ \mathbf{a_2}=a/2(1,0,1);\ \mathbf{a_3}=a/2(0,1,1)$$

where *a* is the lattice parameter. The two-vector basis for material *i* is:

$$1/8(\mathbf{a_1}+\mathbf{a_2}+\mathbf{a_3});\ -1/8(\mathbf{a_1}+\mathbf{a_2}+\mathbf{a_3})$$

while for material *o* the basis is:

$$3/8(\mathbf{a_1}+\mathbf{a_2}+\mathbf{a_3});\ -3/8(\mathbf{a_1}+\mathbf{a_2}+\mathbf{a_3})$$

This particular basis selection will maintain inversion symmetry. The lattice parameter may be calculated in terms of sphere diameter (*d*, same for organic and inorganic spheres) imposing that neighboring spheres are in contact: $a=(4/\sqrt{3})\cdot d$.

6.2.2.2 Graphical description of the mbcc growth in two directions.

Growth in the (001) orientation relies on stacking layers of mixed *i-o* spheres with a square lattice configuration. Here nearest neighbors are of opposite character leading to diagonals of like character as a checkerboard. The cyclic arrangement of subsequent layers is explained in **Fig. 6.7 a**. Each layer is shifted with respect to the layer underneath by half the pitch. The pitch is $(2/\sqrt{3})\cdot d$ (where *d* stands for the sphere diameter) and the distance between successive layers results in $f_{001}=d/\sqrt{3}$.

The stacking procedure along (111) direction is shown in **Fig. 6.7 b**. Here each layer presents a triangular lattice configuration and, as opposed to the (001) case, layers are homogeneous in composition (completely organic or inorganic). The layering sequence reminds that of an fcc lattice (…ABC…) but, in this case, two layers of each material are laid successively. For example, $A_iB_oC_o$-$A_iB_iC_o$-$A_oB_iC_i$…, where sub-indices indicate inorganic (*i*) or organic (*o*) particles. The in-plane distance between neighbor spheres is $(\sqrt{8}/3)\cdot d$ and interlayer distance is $f_{111}=d/3$.

6.2.3 From the mbcc towards the cPBG.

Once the mbcc has been constructed along either (001) or (111) orientation, organic particles are selectively removed to leave a diamond structure of inorganic particles (**Fig. 6.8 b**). At this point two different routes can be pursued depending on the refractive index contrast of the structure. If the spheres used have a refractive index above 2.0, an opal with an omnidirectional gap results. Then, gap width may be fine tuned through a re-grown process by means of CVD similar to that reported in Chapter 5 (**Fig. 6.8 c**). A method recently proposed to produce monodisperse spheres from several oxides with high refractive indexes could serve this purpose.[7] Photonic band gap calculations predict full gaps width as large as

13% for a diamond lattice of high refractive index spheres e.g. silicon (e=12) in air background when filling fraction is 43% (sphere radius 0.236·a).

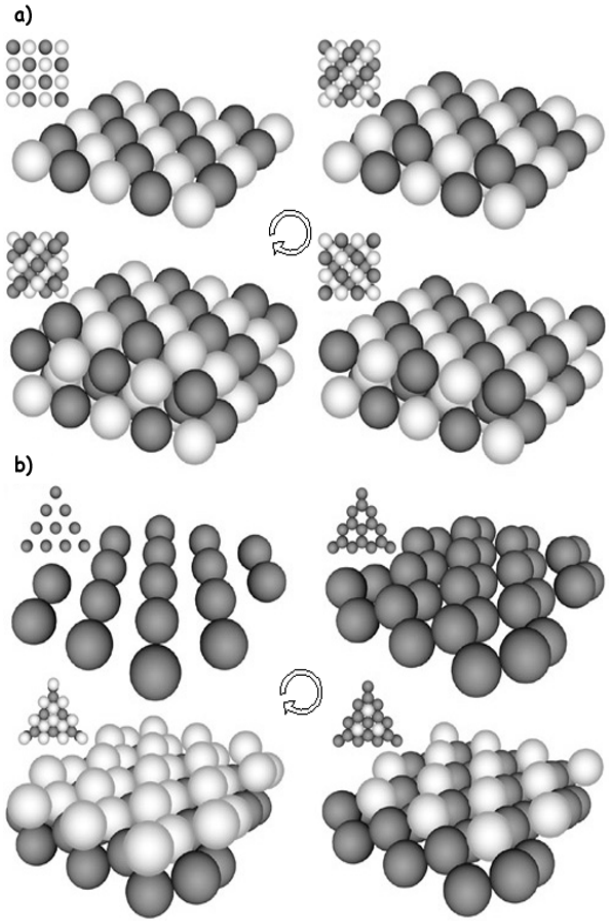

Fig. 6.7: Computer design showing the layout of the first four layers in a mixed body centered cubic lattice where dark and light gray spheres stand for organic and inorganic particles respectively. In a) the stacking is along the (001) direction; the fifth layer is exactly as the first one. In b) the stacking is along the (111) direction; the fifth layer lies exactly on top of the second layer. The insets represent a top view.

When the refractive index of inorganic particles is not above the threshold for full gap openings (>2.0) one should proceed with the inverse diamond structure depicted in **Fig. 6.8 d** and **e**. This may hold when silica is used as the inorganic material; for instance, in the case of silica-latex particles the following procedure would be performed: First, the mbcc structure should be arranged on a patterned substrate with the aid of micro-robot technique. Next, latex spheres are selectively removed by a calcination process. The remaining diamond crystal is then infiltrated with a high dielectric constant material like silicon or germanium, and finally, the removal of the silica spheres produces the inverse opal. Since our ultimate goal is to obtain an inverse structure with a cPBG, one should take into account that

touching air cavities (filling fraction ~34%) in a dielectric medium provide a very narrow gap unless air filling fraction is increased. Again a re-growing process, as depicted in **Fig. 6.8 c**, must be performed prior to the infiltration. This provides the necessary handle to design inverse structures with tailored full gap. **Fig. 6.9** shows the photonic band structure calculations for a silicon infiltrated diamond opal of silica spheres. The inverse structure resulting from silica etching was presented in **Fig. 6.1 b**. The filling fraction of the silica diamond opal is taken to be 50% (sphere radius 0.251·*a*) which determines the air filling fraction of the inverse silicon structure. Maximum values of the gap width are obtained for air spheres filling fractions of 81% (sphere radius 0.325·*a*) if desired.[2]

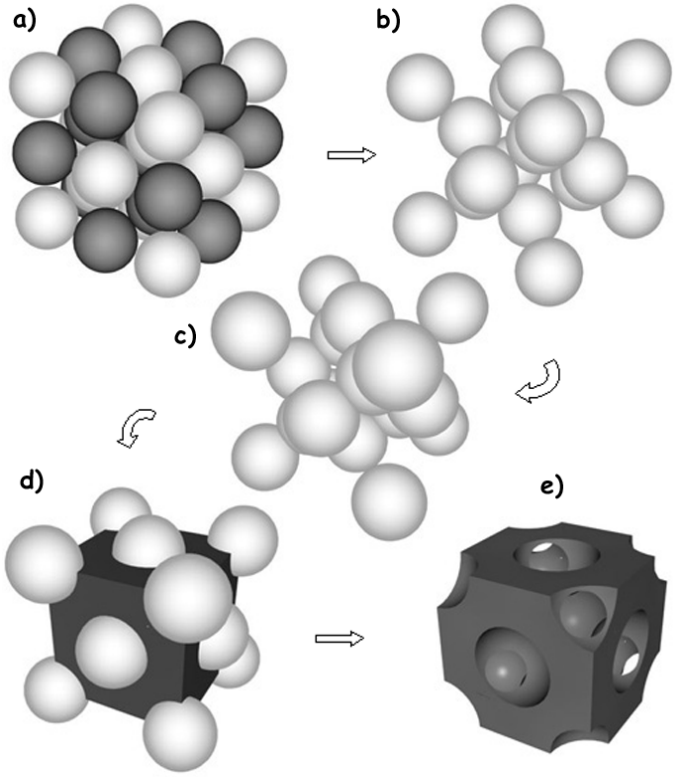

Fig. 6.8: Computer simulation showing, in five steps, the fabrication of an inverse diamond structure with a full photonic band gap. First a mixed body centred cubic lattice is assembled (a) after which, latex sublattice is removed (b); then the spheres are re-grown by CVD to an appropriate filling fraction (c); after that, silicon or germanium infiltration (d) takes place and, finally, silica is eliminated (e).

Other possibilities can be considered when device design is envisaged. Imperfections or uncontrolled defects in the structure are more critical in photonic crystals with larger refractive index contrast. Therefore, one should also consider diamond opals with smaller dielectric contrast (as silicon/silica composites) providing they have a full gap. **Table 6-2** shows the parameters involved in the fabrication of several silicon diamond lattices with different dielectric contrasts.

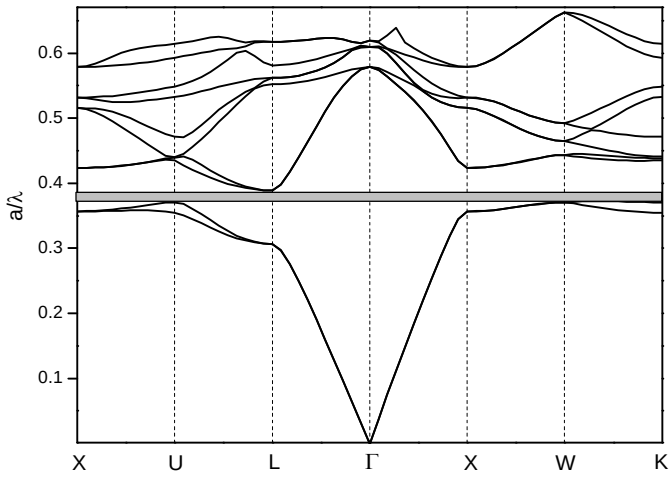

Fig. 6.9: Photonic band diagram of a composite diamond opal made of interpenetrated silica spheres in a silicon background. The filling fraction for silica is 50%.

Spheres	Background	e_1: e_2	ff	$\Delta w/w$	$wa/2\pi c$
Si	Air	11.9 : 1.0	43%	13%	0.45
Si	Silica	11.9 : 2.1	42%	5%	0.41
Air	Si	1.0 : 11.9	50%	12%	0.40
Air	Si	1.0 : 11.9	81%	28%	0.60
Silica	Si	2.1 : 11.9	50%	4%	0.38

Table 6-2: Values of relative gap width ($\Delta w/w$) and midgap position ($wa/2\pi c$), where a is the lattice parameter) for diamond structures made of spheres with different configurations in which materials and filling fraction (ff) percentages have been varied.*

6.3 The experimental development.

Here the experimental development of the ideas introduced in the previous section will be presented.

6.3.1 The nanorobot.

Trapping of micrometric spheres by radiation pressure[8,9] or manipulation of nanometer-size particles with an atomic force microscope[10] has attracted attention for the last decades. The utilization of a nanorobot attached to a Scanning Electron Microscope (SEM) is particularly suitable for building 3D structures from microscopic objects whose size is above 500 nanometers. A probe is controlled with high accuracy (a few nanometers) and used to pick and position the particles. In this scale of sizes, electrostatic and van der Waals forces dominate the dynamics of the micro-objects.[6] To date several measurements of forces (order of nN)

* Most of the values presented in the table were calculated by F. J. López-Tejeira.

involved in the process have been performed[11] together with the development of techniques that improve particles manipulation.[12] However, a satisfactory theoretical model explaining the behavior of micro-manipulated micro-objects is still to be developed.

Fig. 6.10 a shows a schematic drawing of Nanorobot II[13] (HMI Co., Ltd.). There are three different stages:

- A base stage in which movement is allowed in two dimensions (X-Y) normal to the e-beam. This stage is used to position the other two stages under the electron beam of the SEM.
- The specimen stage (left-hand hereafter) where the sample is attached. This stage is to be used for coarse movements (several microns per second) such as initial approximation to the sample substrate and spheres fetching from distances above 10 microns. The movement of this stage is provided by step-by-step motors.
- The probe stage (right-hand hereafter) where a thermally drawn glass pipette covered by a conductive gold layer is attached. This hand is to be used for fine movements such as sample approximation or spheres picking. The range of movement is limited to 15 microns and the accuracy is 10 nm. Motion is generated by a piezoelectric actuator.

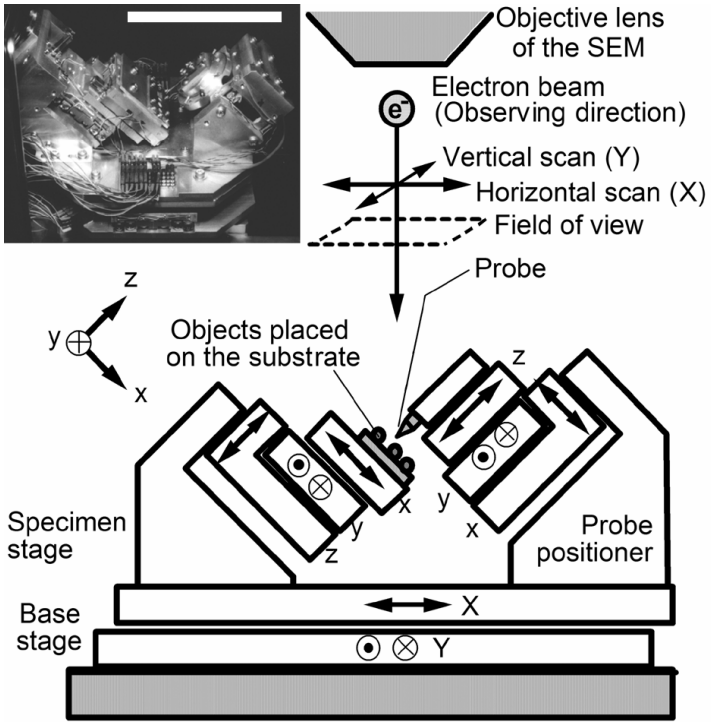

Fig. 6.10: Nanorobot II (HMI Co., Ltd.), schematic picture showing all the possible movements. The top-left inset is an actual picture of the nanorobot. Inset scale-bar is 20 cm. (This scheme has been adapted from an original design made by H. T. Miyazaki).

The manipulator is remotely operated through an interface where several joysticks and control switches were present.

Several factors limit the size of the particles to be manipulated. The tip thickness of the probe attached to the right-hand is usually around 200 nm. Due to the size of the nanorobot, the working distance (WD) between the objective lens of the SEM and the sample is 32 mm, which is not optimal. As a consequence the focusing of the electron beam is worse than in normal circumstances. It must be taken into consideration that, for real-time observation, the scanning velocity of the electron beam must be the as fast as possible, which entails a lower image quality. Finally, the electronics of the nanorobot components and the SEM may interfere. This causes a worsening in the image due to electrical noise. For all these reasons, sizes under 500 nm are not advisable for micromanipulation. In this work spheres diameters were always around one micron.

It is also important to notice that, owing to this configuration, although sample and probe are normal to each other, both tilted 45º with respect to the e-beam. As a result, the image on the SEM screen will be a 2D projection of our sample tilted 45º. **Fig. 6.11 a** shows a SEM image of a template in the observation chamber where the electron beam is normal to the sample surface. **Fig. 6.11 b** shows the same template once the nanorobot has been installed. The squared pattern shown in the screen appears rectangular due to the tilting. As can be observed, the image quality is considerably lower.

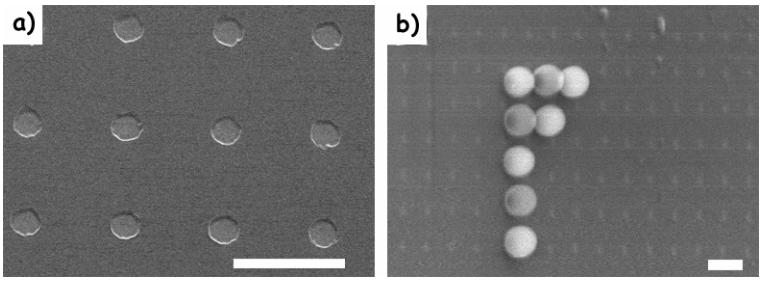

Fig. 6.11: SEM pictures of a template fabricated by electron beam lithography. a) shows the template in the observation chamber and b) shows the same template when the nanorobot has been installed and a few spheres have been deposited. Hole diameter is 300 nm and depth is 50 nm. Scale bars are 1.2 microns. (templates fabricated at IMM-CSIC by J. Anguita).

6.3.2 The templates.

In the near past, 3D fcc lattices made of spheres had been fabricated.[5] In that work, the use of templates was unnecessary since spheres were in contact and attractive van der Waals forces rendered the structure stable. In the case of bcc or diamond structures, the spheres present on each layer are not in contact. This entails two additional difficulties. On the one hand it becomes more difficult to know where each sphere must be stacked in the first layer (subsequent layers spheres will be positioned at well defined minimum energy locations). This could be solved using a graphical template superposed to the SEM screen. However,

since layers are not close-packed, the position of first layer spheres could be easily modified (accidentally) when stacking the next layer spheres. On the other hand, forces between spheres pose a new difficulty. At short distances spheres repel each other due to Coulomb repulsive forces. However, when distance is decreased to a critical value between spheres attractive van der Waals forces become stronger. The order of magnitude of these distances is not much larger than the lattice parameter of our structures and, therefore, the effect of these forces can be significant. As a consequence, a templated substrate is needed to firmly stack the spheres in predefined spatial positions.

There are two conditions that must be accomplished by the substrate where the samples are to be fabricated. First, the substrate must be conductive, otherwise, under the e-beam exposure both substrate and sample would get electrically charged what would eventually worsen the picture quality or even completely prevent the observation. Second, the substrate must be transparent in the IR region if transmission optical properties are to be measured. A good candidate that satisfies both conditions is a doped ($>10^{17}$ cm^{-3}) silicon wafer.

6.3.2.1 Template models.

The first trial template was a patterned substrate made by means of electron beam lithography (see **Fig. 6.11**).[*] In this template, holes had a diameter of 300 nm and a depth of 50 nm. Although these holes were clearly differentiated in the observation chamber of the SEM, they could be hardly distinguished when the nanorobot was installed; even for the lowest scanning velocities. As an additional problem, for unknown reasons, the holes got negatively charged and spheres were strongly repelled. This kind of templates was therefore discarded.

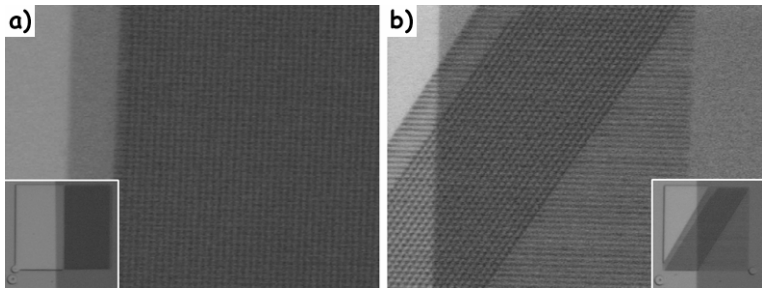

Fig. 6.12: Optical images of templates formed by crossings of parallel gold lines on a silicon wafer with a 300 nm layer of SiO_2 on the surface. a) cross-points of two sets of perpendicular lines of gold designate the positions of spheres for growth in the (001) direction. b) if the angle between both sets of lines is 60º, cross-points will designate locations for growing in the (111) direction. The insets show a low magnification view of the templates. (templates fabricated at IMM-CSIC by J. Anguita).

Another design was fabricated. This time the location for spheres was designated by the cross-points of two sets of parallel lines.[*] The template was

[*] These templates were fabricated at IMM-CSIC by J. Anguita.

fabricated on a silicon wafer with a 300 nm layer of SiO_2 on the surface. For growth in the (001) direction sets of lines were perpendicular (**Fig. 6.12 a**), for the (111) direction they formed 60º (**Fig. 6.12 b**). The advantage of gold is that it can be very easily distinguished when observing with a SEM. As SiO_2 is not conductive, gold lines were grounded so that a system of negative charged and zero potential (the gold cross-points) areas would be created. This way, spheres should be repelled by SiO_2 and the most stable positions would be the gold line crossings. However, electrostatic forces resulted to be too weak, and the template was not effective. Although the positions for a correct stacking could be clearly discerned, the spheres were not firmly attached becoming a bad anchorage for second layer spheres. Again, these templates were discarded.

In 2000 M. Holgado had shown that focus ion beam (FIB) etching could be used to fabricate 2D photonic Crystals.[14] The samples he fabricated consisted of arrays of holes that proved to work when used as templates for spheres stacking (see **Fig. 6.13**). Although lattice parameter was not optimal and hole sizes were irregular, this template showed that it was enough to keep first layer spheres firmly attached to the substrate.

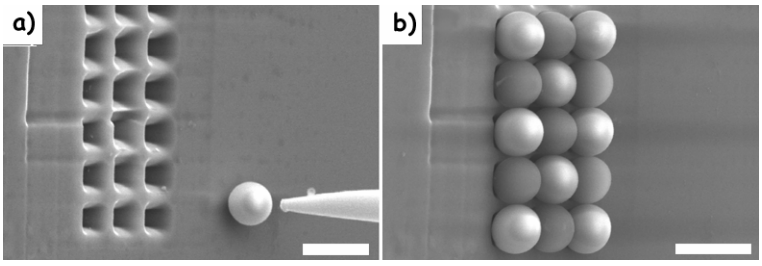

Fig. 6.13: SEM images of a) an array of holes performed with focused-ion-beam micromilling. In b) latex and silica spheres remain firmly attached to the holes where they were placed. Scale bars are 3 microns. (Template fabricated by M. Holgado at Lucent Technologies ME. SEM images and micromanipulation performed by H. T. Miyazaki).

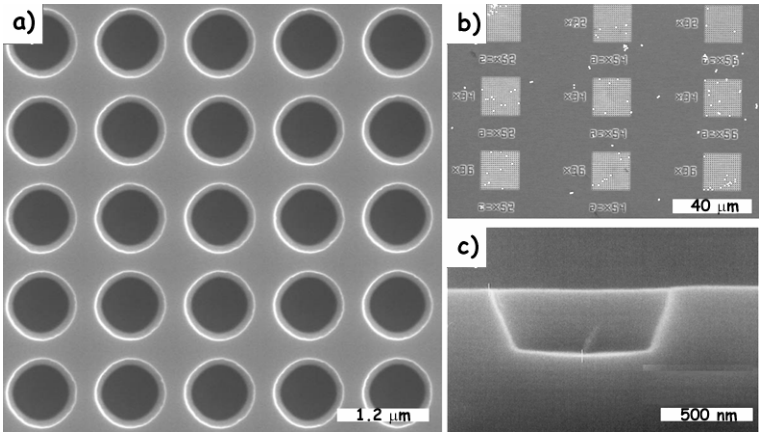

Fig. 6.14: Templates fabricated by photolithography. a) shows a SEM image of a lattice for the (001) direction growth. On b) several templates can be seen. c) Shows a cleaved profile of one of the holes. (Templates fabricated by Agere Systems Spain).

Since FIB was not an optimal tool to fabricate large a number of patterns, photolithography was the technique selected to obtain the definitive templates. This procedure is more expensive since previous fabrication of a mask is needed but, on the other hand, once the mask is fabricated the lithographic process can be repeated as many times as needed and the quality of the patterned substrates is excellent. The motives present in the mask are afterwards transferred to a photoresist. The resin is developed and the pattern is finally etched on the silicon substrate. A mask with many templates of different hole diameters and pitches was fabricated (see **Fig. 6.14**) and used for the photolithographic procedure.*

6.3.2.2 Hole depth and diameter.

The features of these holes will depend on the size of the spheres and the desired crystallographic orientation of the samples to be grown on the template. The spheres must be held in place by the rim of the holes and not touch the bottom to make sure that they will not move. To find an appropriate depth and diameter for the holes, two constraints must be taken into account. On the one hand, spheres must stick out enough to support those from the second layer that, otherwise, would lie on the substrate (and not have well defined positions as a consequence). On the other hand, holes must be deep enough to provide a good anchorage for the beads. If these conditions are fulfilled the spheres fixed in the holes are stable extremely difficult to remove from the template.

In the case of the (001) direction the distance between planes is $f_{001}=d/\sqrt{3}\approx 0.58\ d$, this means that spheres can be half buried without affecting the next layer positions. As we want the spheres to be held by the rim of the holes, the only constraint is hole diameter (D) smaller than the sphere diameter ($D<d$) and depth above sphere radius.

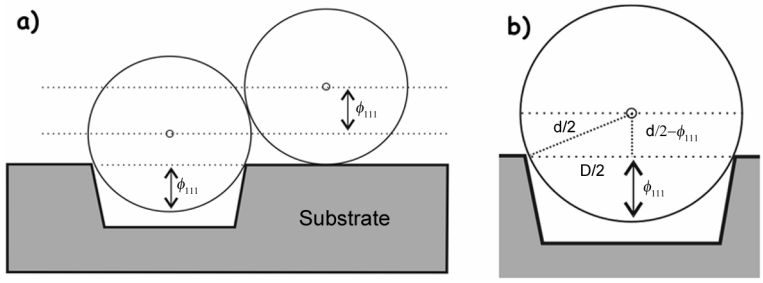

Fig. 6.15: Scheme showing some considerations about spheres and holes sizes. In a) it is shown that maximum depth for spheres must below the interlayer distance, otherwise second layer spheres would touch the substrate. b) shows the relationship between sphere size and hole diameter. D is hole diameter, d is sphere diameter and f_{111} is the interlayer distance.

For the (111) direction, some calculations must be done since interlayer distance is smaller $f_{111}=d/3\approx 0.33\ d$. This means that the maximum depth of the

* The mask design and photolithographic process were performed at Agere Systems Spain.

spheres of the first layer can not be over that value, otherwise the second layer spheres would be supported by the substrate and not by the first layer (see **Fig. 6.15 a**). If the spheres are to be held by the rim of the holes the value for the maximum diameter of the hole can be obtained as explained in **Fig. 6.15 b**:

$$D \leq \sqrt{d^2 - (d - 2f_{111})^2}$$

Where D is the hole diameter, d the sphere diameter and f_{111} the interlayer distance in the (111) direction. For 1 micron spheres, D should be below 0.94 microns. To avoid the sphere touching the bottom of the hole is enough with setting a depth above f_{111} (0.33 microns for 1 micron spheres).

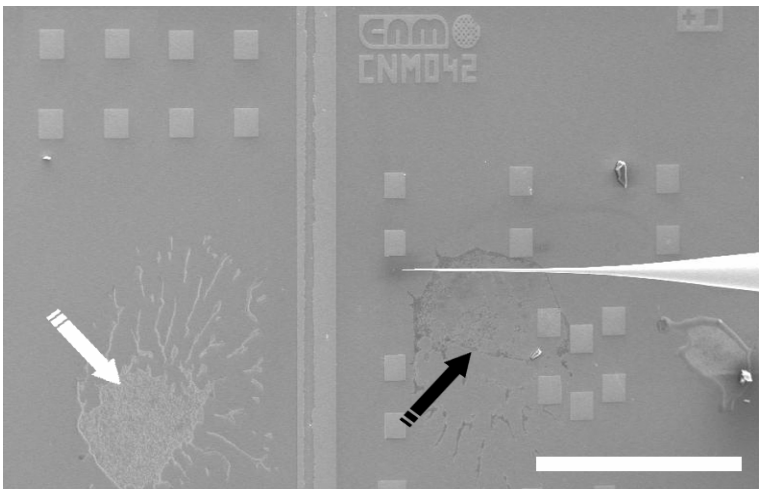

Fig. 6.16: SEM picture showing the silica (white arrow) and latex (black arrow) reservoirs. The end of the probe attached to the nanorobot is exactly over the area where the sample was fabricated. Scale bar is 600 microns.

6.3.3 Micro-manipulation and sample stacking.

Since each sphere deposited with the nanorobot is supported by those of the layer underneath (except first layer spheres), structures shown in this work have a pyramidal shape. However, vertical walls could be obtained using latex spheres as a lateral scaffold. This procedure would not involve any additional difficulty apart from a larger number of spheres to be manipulated, and therefore, a longer fabrication time.

The time needed to build up the structures will strongly depend on whether the sample is grown along the (001) or (111) direction. Due to our nanorobot configuration, one of the most time-consuming tasks was fetching spheres from a distant reservoir (several hundred microns away) to the template field. Whenever the probe must be carried so far, it is necessary to move it away from the substrate. The reason is that in case the probe and the substrate were not perfectly normal, the probe could collide and be damaged. This involves a great amount of time because the approximation of the probe to the substrate must be done very carefully; the

substrate itself can not be distinguished if there is not any motive on it. As the screen gives a 2D image, knowing the distance from the tip of the probe to the substrate is not trivial.

6.3.3.1 Growth in the (001) direction.

To grow a sample in the (001) direction, two reservoirs (one of latex and another of silica spheres) were set apart by the template field chosen (see **Fig. 6.16**). The beads were picked one by one and placed at the predefined sockets on the patterned substrate (first layer) or at the appropriate position in a stable location among four supporting spheres from the layer underneath (other layers). The average time needed for each sphere was about 7 minutes. **Fig. 6.17** shows the fabrication sequence. The final structure after setting 165 spheres of latex and 177 of silica (the sixth layer is composed only of silica spheres).

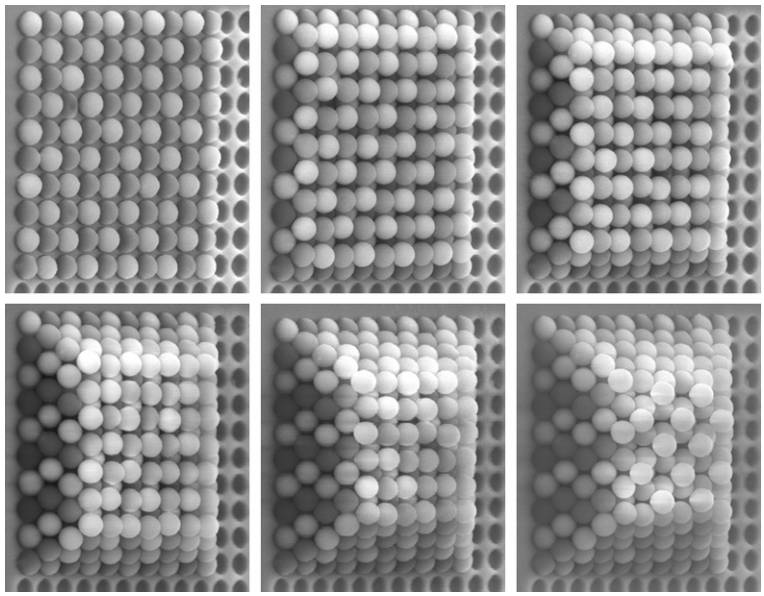

Fig. 6.17: Sequence of mbcc fabrication in the (001) direction. In each layer (but the last one) there are silica and latex spheres. In the sixth layer only silica spheres were stacked. The final structure is formed by 165 latex spheres and 177 of silica. The sphere diameter is 1.18 microns. The pitch of the silicon template is 1.35 μm. Holes depth and diameter is 450 nm and 1.08 μm respectively. Layer-to-layer distance is 680 nm.

6.3.3.2 Growth in the (111) direction.

Growing the mbcc lattice along the (111) direction presents an important advantage: unlike (001) oriented crystals, each layer is formed of a sole kind of spheres. This meant that the reservoir of silica could be placed right on the template itself. Under these circumstances, the average time was reduced to 2.5 minutes per silica sphere. **Fig. 6.18** shows the fabrication sequence of a six layers mbcc structure made of 133 spheres of latex and 274 of silica. The first two layers are made of silica spheres, the next two layers of latex and fifth and sixth of silica again.

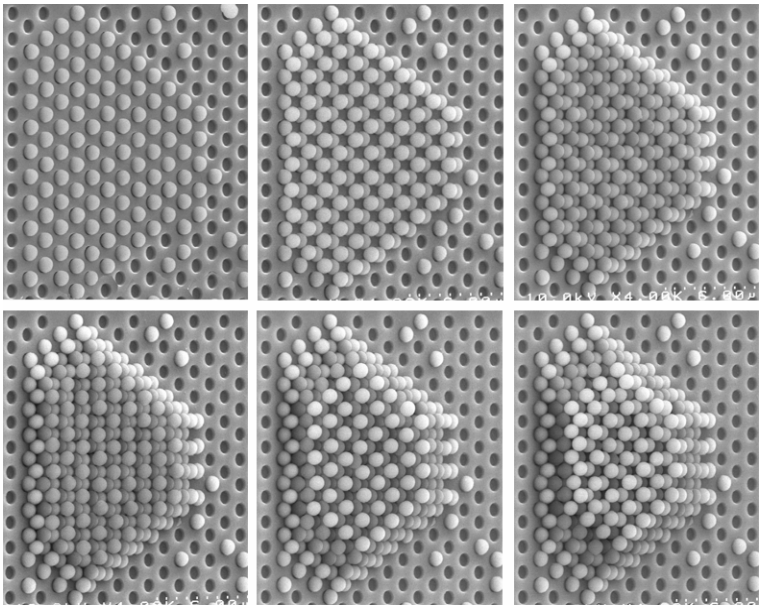

Fig. 6.18: Sequence of mbcc fabrication in the (111) direction. Only one kind of spheres is present in each layer. Layers number 1, 2, 5 and 6 comprise silica spheres. Layers 3 and 4 contain latex spheres only. The final structure is formed by 133 latex spheres and 274 of silica. Layer-to-layer distance is 300 nm. Spheres diameter is 0.9 μm. The pitch of the silicon template is 1.45 μm. Holes depth and diameter is 350 nm and 754 nm respectively.

6.3.4 Sacrificial scaffold removal.

After the fabrication of the mbcc lattice, it is necessary to etch the latex spheres away to achieve the diamond structure. The removal of latex by calcination is a well-known procedure to obtain inverse opals. Indeed, many research groups work with self-assembled opals made of latex spheres. Once they have loaded the opal interstices with an appropriate material, latex is burned at 450ºC.[15]

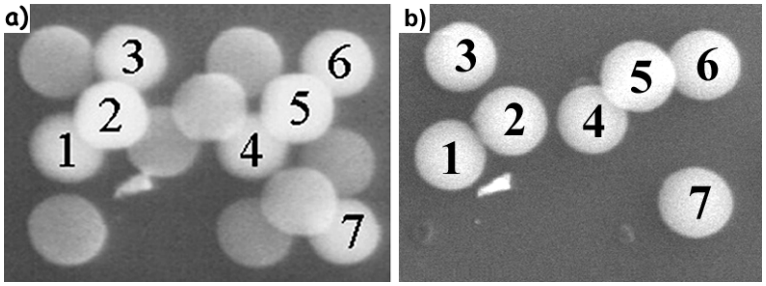

Fig. 6.19: a) A two layers mbcc lattice was fabricated to test the effects of latex calcination. ab) After burning the latex at 400ºC for 3 hours the positions of silica spheres (those labeled) have varied.

In our case, latex calcination was discarded since it entailed a liquid phase of latex. Due to surface tension silica beads were dragged and the structure collapsed. **Fig. 6.19 a** shows a two layers mbcc lattice grown in the (001) direction and used

to test the calcination effects. After placing the samples in a furnace at 400 ºC for 3 hours (**Fig. 6.19 b)** it can be seen how silica spheres were dragged away from their initial positions. Especially affected were those in close contact with latex spheres (namely, spheres labeled 2 to 5 and 7).

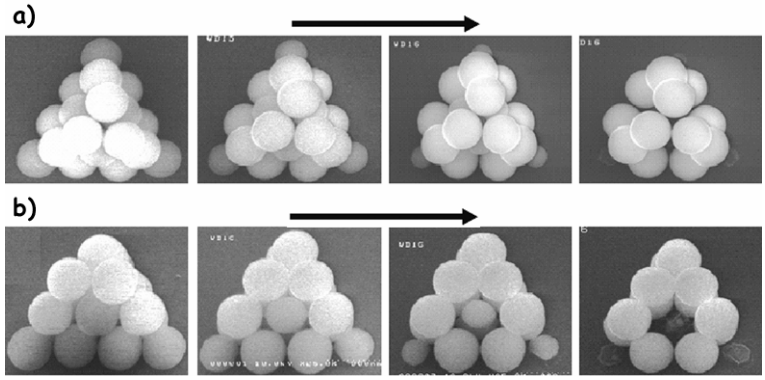

Fig. 6.20: A three layers sample made of silica and latex spheres to test the stability after latex removal by oxygen plasma etching. a) top view and b) tilted 45º. Arrows show the time evoulution in periods of 20 minutes.

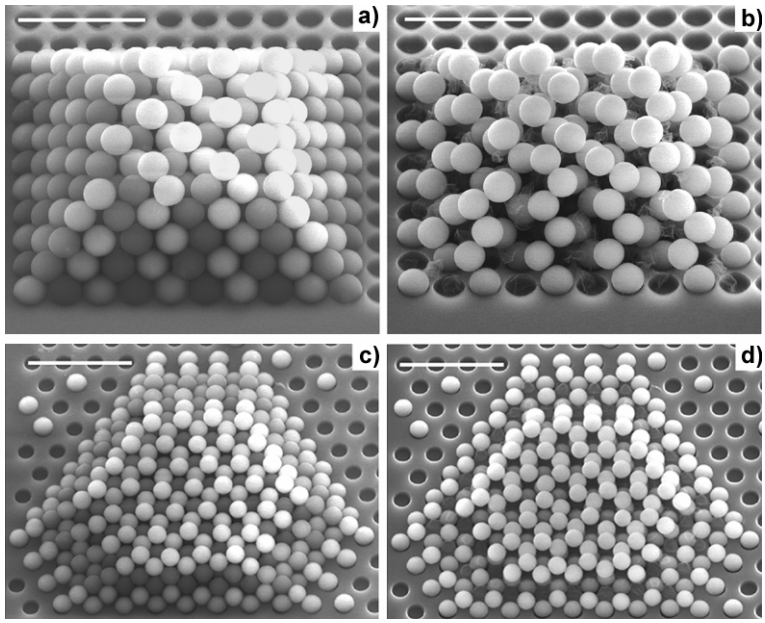

Fig. 6.21: a) and b) show the sample of **Fig. 6.17** before and after plasma etching. Pictures are tilted 45º to show {011} facets. c) and d) show the sample of **Fig. 6.18** before and after latex removal. Pictures are tilted 30º. In all pictures scale bars are 5 microns.

Oxygen plasma etching provided an alternative to calcination. For this purpose a mini-sputtering chamber* was used to create oxygen plasma between two

* Sputtering chamber modifications and experimental setup were done by H. T. Miyazaki.

electrodes at 65 mW/cm^2 and 30 Pa.[16] The plasma selectively removes latex and hardly affects the silicon wafer or silica in these working conditions. Since oxygen plasma may attack the electrodes and sputter aluminum on our sample, the substrates were placed in a glass cell with lateral openings. **Fig. 6.20** shows a structure (which is not a mbcc) made of silica and latex spheres designed to test the stability of the sample after the plasma etching. It can be observed how latex is gently removed without disturbing the positions of silica spheres despite of their unstable positions.

Plasma etching was applied to the mbcc structures obtaining the results shown in **Fig. 6.21**. It is interesting to highlight that, in **Fig. 6.21 d**, the 3rd diamond layer lies exactly on top of the second one, in other words each sphere has only one point of contact with the layer underneath. Nevertheless the structure is stable after the etching.

6.4 Direct stacking of the diamond structure.

So far, latex spheres have been used to scaffold a structure where minimum energy positions were available for next layer beads. However, latex would be unnecessary if silica spheres could be glued to each other while keeping the appropriate position.

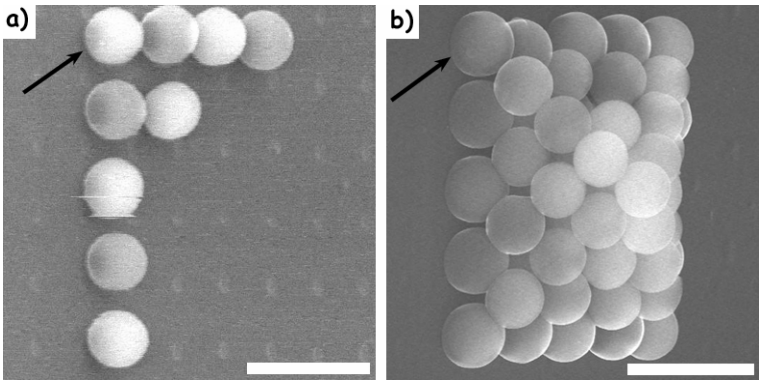

Fig. 6.22: SEM observation involves the deposition of contamination. Picture a) shows the beginning of a sample fabrication, the arrow points at a silica sphere. In b), the sample has been finished. The arrow points at the same sphere and it can be clearly observed that size of the sphere has increased due to a deposited layer of contamination. Scale bars are 2 microns.

6.4.1 SEM contamination.

It is well known by SEM microscopists that observation involves the formation of an amorphous carbon-rich contamination film.[17] The effects of this contamination can go unnoticed when observation takes place in short periods of time. However manipulation implies working for several hours in the area where the sample is grown. **Fig. 6.22 a** shows some spheres of the first layer of an mbcc being fabricated in the (001) direction. Once the sample has been finished (**Fig.**

6.22 b), the spheres of the first layer have increased their diameter. This is due to the layer of contamination that has affected, mainly, the objects observed for the longest times. Notice that the template marks have been covered by contamination as well.

The contamination can be grown on purpose by focusing the SEM electron beam on a specific area. This technique is known as electron-beam-induced deposition (EBID).[18] **Fig. 6.23 a** shows a layer of contamination that was deposited at the junction between a silica and a latex sphere using this method for one hour. Plasma etching can remove both latex and contamination as shown in **Fig. 6.23 b** and **c**.

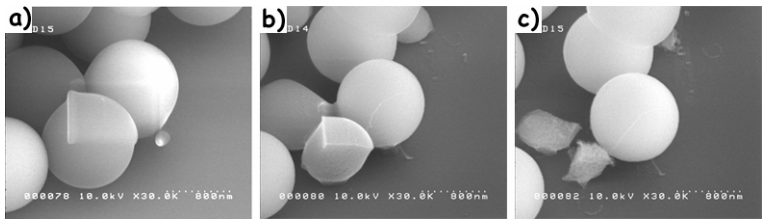

Fig. 6.23: In a) a rectangular shaped layer of contamination was accurately deposited by focusing the electron beam of the SEM for an hour. This contamination is mostly composed of organic material and [b) and c)] can be removed with oxigen plasma etching.

6.4.2 Direct growth in the (001) direction.

In previous sections, contamination was simply an unimportant inconvenience that could be eliminated when latex was etched away. However, as it can be grown very accurately, EBID may become a very useful tool when used to glue spheres. Silica spheres are firmly fixed if the electron beam is focused on their junction for just a few seconds. The contamination is deposited accurately in a small area around the contact point. This way, sacrificial scaffolds are no longer needed. The method will be eligible provided the junctions between spheres are accessible to the electron beam.

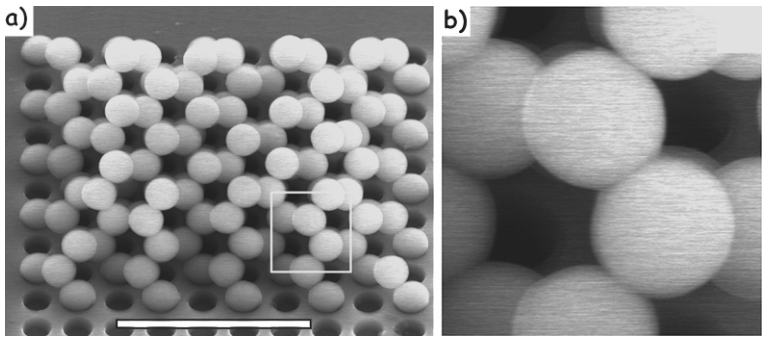

Fig. 6.24: Five layers diamond lattice directly grown in the (001) orientation. a) Structure made of 165 silica spheres of 0.9 microns of diameter. b) Detail of a contact point between two silica beads. Contamination was used to glue them. The pitch of the silicon template is 1.05 microns. Holes depth and diameter is 450 nm and 770 nm respectively. Layer-to-layer distance is 520 nm. Pictures are tilted 45º to show {011} facets. Scale bar is 5.0 microns.

Diamond lattices were grown in the (001) direction by means of this method (**Fig. 6.24 a**). In the standard working conditions, the sample is tilted 45º with respect to the electron beam while manipulation takes place. This tilting shows the {011} planes, and this orientation is optimal because contact points between spheres are clearly observable as shown in **Fig. 6.24 b**. By way of time gauge, it must be remarked that the sample shown in this figure was made of 165 silica spheres and was finished in 10.5 hours. **Fig. 6.25** shows a four layers sample grown using the EBID technique as well. It is made of 290 silica spheres. For this sample 12 hours of nanorobot manipulation were needed.

There are two obvious advantages of direct growth. Firstly, fabrication time is drastically reduced since stacking latex is not needed anymore, besides, the silica spheres reservoir can be placed close to the template. Secondly, the quality of the samples is improved as can be observed by comparing the SEM images presented in this section with those of the previous one.

The only disadvantage is that with the particular configuration of this experiment, the method is ineffective for the (111) growing direction because some spheres must be placed exactly on top of another. This would require a 90º and consequently their contact point cannot be scanned at 45º since it is not accessible to the electron beam.

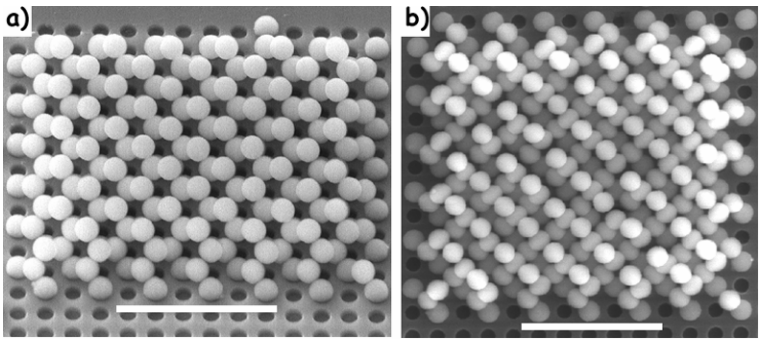

Fig. 6.25: Four layers diamond lattice directly grown in the (001) orientation. a) View tilted 45º and b) top view. The structure is made of 290 silica spheres of 0.9 microns of diameter. The pitch of the silicon template is 1.05 microns. Holes depth and diameter is 450 nm and 770 nm respectively. Layer-to-layer distance is 520 nm. Scale bars are 6.0 microns.

6.5 Summary.

6.5.1 Conclusions.

- A method to construct opal-like crystals with diamond symmetry by robot aided micromanipulation has been shown. It should lead to three-dimensional photonic crystal structures able to sustain robust full gaps. The position of the complete gap and its width may be controlled by varying the particles diameter and the filling fraction.

- Templates fulfilling all the necessary requirements to firmly attach the first layer were designed and fabricated.
- Oxygen plasma etching has proven to be an optimal technique to remove latex spheres without affecting the remaining structure made of silica.
- Diamond structures with micron size periodicity have been fabricated in two different orientations: (001) and (111).
- A technique in which a sacrificial scaffold is not needed was developed and applied to obtain diamond structures in the (001) orientation.
- Results demonstrate the viability of this method to prepare macroporous lattices, open the way to controllable formation of a wide variety of microstructures and provide a new route to the study of novel lattices with photonic properties.

6.5.2 Future research.

At this point diamond structures made of micrometric silica spheres have been fabricated. There is, however, some work that has not been done yet.

- Optical measurements. The dimensions of the samples fabricated in this work ranges from 10 to 14 microns of lateral size in their base and the number of layers rages from 4 to 6 layers. The substrate is made of silicon, with a high dielectric constant compared to that of silica. Under these circumstances, obtaining optical data is not a trivial issue. However, with appropriate equipments optical spectra of similar sized structures have been obtained.[19] The problem of low refractive index is expected to be solved after semiconductor infiltration.
- Filling fraction adjustment. The filling fraction of diamond structures presented in this chapter is 34%. This value is too low to obtain a cPBG even if the lattice is infiltrated with a high dielectric constant material and then inverted. To increase the filling fraction, sintering the sample must be discarded since it carries a decrease of silica spheres diameter and the structure is distorted. An alternative that would not affect the lattice parameter is the controlled growth of a Ge layer by CVD (as shown in previous chapter) and posterior oxidation. **Fig. 6.26** shows the relationship between sphere radius and filling fraction of a diamond structure obtained from Montecarlo calculation. This would lead to a mixed structure of interpenetrated spheres made of SiO_2 with a shell of GeO_2. These oxides could be easily etched away with HF in the inversion stage. Another possibility is growing silica by a CVD process.[20] The advantage of the former method is that accurate control of the deposited layer thickness has been already proved (Chapter 5).
- Semiconductor infiltration. Once an adequate filling fraction is achieved, infiltration of the sample with a high refractive material is the next step to take. Silicon and germanium are ideal candidates to be grown by CVD. At

this stage, crystals should present a cPBG provided the number of layers was enough.

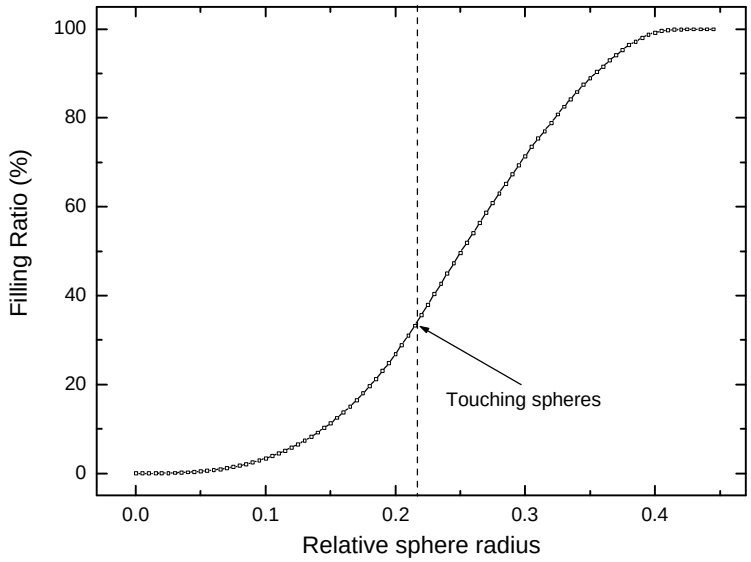

Fig. 6.26: Relationship between sphere radius (relative to lattice parameter) and filling fraction in a diamond structure. The arrow points at the value at which spheres are touching each other. Above that value spheres are interpenetrated.

- Structure inversion. To increase the refractive index contrast the samples could be inverted by etching the oxides with HF. The difference with the inversion of artificial opals is that, in our case, there would be no silica exposed to air and therefore it would be isolated form the acid (in the case of artificial opals they are usually cleaved for this purpose). A possible solution is applying reactive ion etching to expose one of the sample facets.[21]

The use of nanorobotic manipulation to fabricate photonic crystals as proposed in this dissertation is still far from being really practical for industrial purposes. Time needed to fabricate samples and working conditions lead to discard manual stacking of spheres at current date. However, many of the limitations could be solved with a nanorobot specially designed to fabricate photonic crystals. Custom sample-e-beam orientation, especial implementations for beads supply, and some improvements (to avoid equipment faults) are some of the ideas this work brought up. Research on robotics is still a novel field and many advances are made every day. Automatic identification and manipulation of particles by a computer-controlled nanorobot is already being developed.[22]

In terms of basic research, this is the first time that diamond lattices made of micrometric silica spheres have been fabricated. Besides, the procedure here proposed opens a wide range of possibilities for engineering new structures and, in particular allows, the control of structural defects (as point and line lattice defects)

for direct and inverse structures. Single inorganic spheres or rows of them can be replaced by their organic counterparts in the mbcc to produce point or line defects (air cavities and waveguides) after the etching. Nanorobotic manipulation has proven to be useful also to fabricate *woodpile* structures (**Fig. 6.27**).[23]

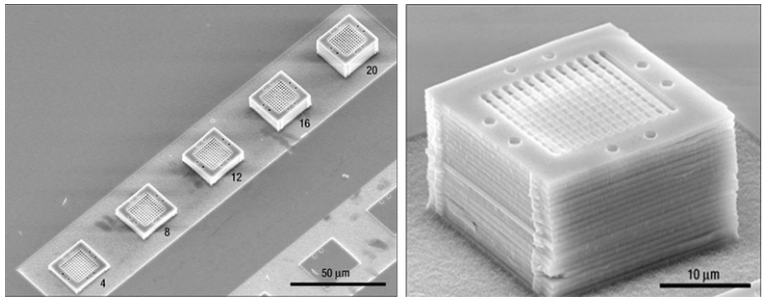

Fig. 6.27: Woodpile structures fabricated stacked with a nanorobot. SEM images were taken from ref. 23.

A very desirable achievement would be the fabrication of diamond lattices by self-assembly methods. In this sense, the method presented here may be useful as well. A work recently presented by Velikov *et al*,[24] has shown that obtaining non close packed structures by self assembly is possible. Samples are obtained by layer by layer growth of spheres of different diameters. This method could be developed to grow mbcc samples in the (111) orientation since for this direction each layer is homogeneous (made only of silica or latex spheres).

Hopefully this study will serve to foster the development of novel techniques that, with the advances in microscopy and robotics, can end up in very promising practical applications in different research fields such as photonics or biomaterials technology.[25]

6.6 References.

1 Li, Z. Y. & Zhang, Z. Q. Fragility of photonic band gaps in inverse-opal photonic crystals. *Phys. Rev. B* **62**, 1516 (2000).

2 Ho, K. M., Chan, C. T. & Soukoulis, C. M. Existence of a Photonic Gap in Periodic Dielectric Structures. *Phys. Rev. Lett.* **65**, 3152 (1990).

3 Lin, S. Y. *et al.* A three-dimensional photonic crystal operating at infrared wavelengths. *Nature* **394**, 251 (1998).

4 Noda, S., Tomoda, K., Yamamoto, N. & Chutinan, A. Full three-dimensional photonic bandgap crystals at near-infrared wavelengths. *Science* **289**, 604 (2000).

5 Miyazaki, H. & Sato, T. Mechanical assembly of three-dimensional microstructures from fine particles. *Adv. Robot.* **11**, 169 (1997).

6 Miyazaki, H. T., Miyazaki, H., Ohtaka, K. & Sato, T. Photonic band in two-dimensional lattices of micrometer-sized spheres mechanically arranged under a scanning electron microscope. *J. Appl. Phys.* **87**, 7152 (2000).

7 Jiang, P., Bertone, J. F. & Colvin, V. L. A lost-wax approach to monodisperse colloids and their crystals. *Science* **291**, 453 (2001).

8 Ashkin, A. Acceleration and Trapping of Particles by Radiation Pressure. *Phys. Rev. Lett.* **24**, 156 (1970).

9 Chu, S. The manipulation of neutral particles. *Rev. Mod. Phys.* **70**, 685 (1998).

10 Schaefer, D. M., Reifenberger, R., Patil, A. & Andres, R. P. Fabrication of 2-Dimensional Arrays of Nanometer-Size Clusters with the Atomic-Force Microscope. *Appl. Phys. Lett.* **66**, 1012 (1995).

11 Miyazaki, H. T., Tomizawa, Y., Saito, S., Sato, T. & Shinya, N. Adhesion of micrometer-sized polymer particles under a scanning electron microscope. *J. Appl. Phys.* **88**, 3330 (2000).

12 Saito, S., Miyazaki, H. T., Sato, T. & Takahashi, K. Kinematics of mechanical and adhesional micromanipulation under a scanning electron microscope. *J. Appl. Phys.* **92**, 5140 (2002).

13 Morishita, H. & Hatamura, Y. Development of Ultra Micromanipulator System under Stereo Sem Observation. *Iros 93: Proceedings of the 1993 Ieee/Rsj International Conference on Intelligent Robots and Systems, Vol 1-3*, 1717 (1993).

14 M. Holgado. Cristales de ondas. (PhD. thesis, Universidad Politécnica de Madrid, 2000).

15 Velev, O. D., Jede, T. A., Lobo, R. F. & Lenhoff, A. M. Porous silica via colloidal crystallization. *Nature* **389**, 447 (1997).

16 Haginoya, C., Ishibashi, M. & Koike, K. Nanostructure array fabrication with a size-controllable natural lithography. *Appl. Phys. Lett.* **71**, 2934 (1997).

17 L. Reimer, Scanning Electron Microscopy (Springer-Verlag, Berlin Heidelberg, ed. 2, 1985) pp. 132-134.

18 Koops, H. W. P. *et al.* Characterization and Application of Materials Grown by Electron-Beam-Induced Deposition. *Jpn. J. Appl. Phys. Part 1 - Regul. Pap. Short Notes Rev. Pap.* **33**, 7099 (1994).

19 Miguez, H., Yang, S. M., Tetreault, N. & Ozin, G. A. Oriented free-standing three-dimensional silicon inverted colloidal photonic crystal microribers. *Adv. Mater.* **14**, 1805 (2002).

20 Miguez, H. *et al.* Mechanical stability enhancement by pore size and connectivity control in colloidal crystals by layer-by-layer growth of oxide. *Chem. Commun.*, 2736 (2002).

21 Vlasov, Y. A., Bo, X. Z., Sturm, J. C. & Norris, D. J. On-chip natural assembly of silicon photonic bandgap crystals. *Nature* **414**, 289 (2001).

22 Kasaya, T., Miyazaki, H., Saito, S. & Sato, T. Micro object handling under SEM by vision-based automatic control. *Icra '99: Ieee International Conference on Robotics and Automation, Vols 1-4, Proceedings*, 2189 (1999).

23 Aoki, K. *et al.* Microassembly of semiconductor three-dimensional photonic crystals. *Nat. Mater.* **2**, 117 (2003).

24 Velikov, K. P., Christova, C. G., Dullens, R. P. A. & van Blaaderen, A. Layer-by-layer growth of binary colloidal crystals. *Science* **296**, 106 (2002).

25 Zhang, H. *et al.* Robotic micro-assembly of scaffold/cell constructs with a shape memory alloy gripper. *2002 Ieee International Conference on Robotics and Automation, Vols I- Iv, Proceedings*, 1483 (2002).

Appendix I: Reciprocal lattice vectors and high symmetry points.

I.1 Simple cubic lattice.

A symmetric set of primitive vectors for the simple cubic (sc) lattice is:

$$\vec{a}_1 = a(1 \quad 0 \quad 0); \qquad \vec{a}_2 = a(0 \quad 1 \quad 0); \qquad \vec{a}_3 = a(0 \quad 0 \quad 1)$$

where a is the lattice parameter. The reciprocal lattice vectors generate another sc lattice with atom coordinates given by:

$$\vec{b}_1 = \frac{2p}{a}(1 \quad 0 \quad 0); \qquad \vec{b}_2 = \frac{2p}{a}(0 \quad 1 \quad 0); \qquad \vec{b}_3 = \frac{2p}{a}(0 \quad 0 \quad 1)$$

The Brillouin zone (BZ) for a sc lattice is a cube as shown in. Fig. I.1. High symmetry points are also represented and labeled as Γ (center of the BZ), X, M and R.

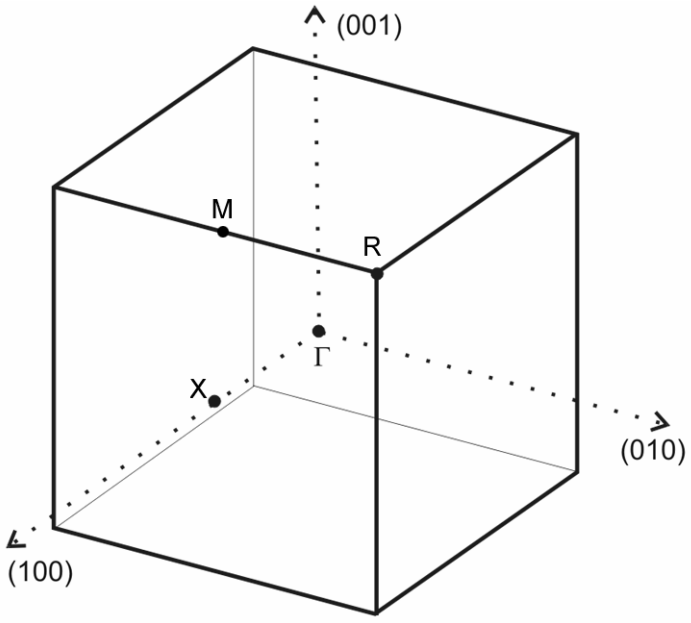

Fig. I.1: sc Brillouin zone and most important symmetry points.

The symmetry points coordinates in the reciprocal lattice for the particular choice of Fig. I.1 are:

$$X=\left(\frac{1}{2}\quad 0\quad 0\right)\cdot\begin{pmatrix}\vec{b}_1\\ \vec{b}_2\\ \vec{b}_3\end{pmatrix}=\frac{2p}{a}\left(\frac{1}{2}\quad 0\quad 0\right)\qquad M=\left(\frac{1}{2}\quad 0\quad \frac{1}{2}\right)\cdot\begin{pmatrix}\vec{b}_1\\ \vec{b}_2\\ \vec{b}_3\end{pmatrix}=\frac{2p}{a}\left(\frac{1}{2}\quad 0\quad \frac{1}{2}\right)$$

$$R=\left(\frac{1}{2}\quad \frac{1}{2}\quad \frac{1}{2}\right)\cdot\begin{pmatrix}\vec{b}_1\\ \vec{b}_2\\ \vec{b}_3\end{pmatrix}=\frac{2p}{a}\left(\frac{1}{2}\quad \frac{1}{2}\quad \frac{1}{2}\right)$$

I.2 Body centered cubic lattice.

A symmetric set of primitive vectors for the body centered cubic (bcc) lattice is:

$$\vec{a}_1=\frac{a}{2}(-1\quad 1\quad 1);\qquad \vec{a}_2=\frac{a}{2}(1\quad -1\quad 1);\qquad \vec{a}_3=\frac{a}{2}(1\quad 1\quad -1)$$

The reciprocal lattice vectors generate a face centered cubic (fcc) lattice with atom coordinates given by:

$$\vec{b}_1=\frac{2p}{a}(0\quad 1\quad 1);\qquad \vec{b}_2=\frac{2p}{a}(1\quad 0\quad 1);\qquad \vec{b}_3=\frac{2p}{a}(1\quad 1\quad 0)$$

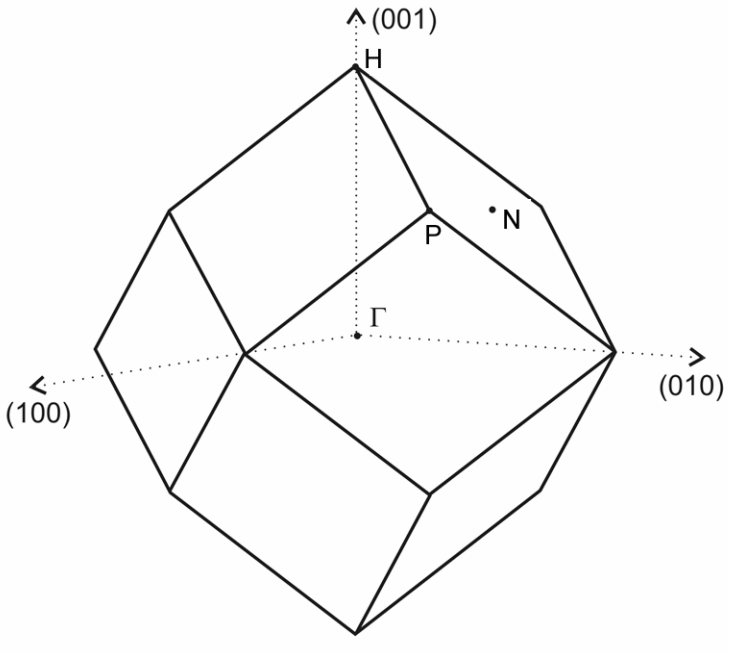

Fig. I.2: bcc Brillouin zone and most important symmetry points.

The BZ for a bcc lattice is a rhombic dodecahedron as shown in. **Fig. I.2**. High symmetry points are also represented and labeled as Γ (center of the BZ), P, H and N.

The symmetry points coordinates in the reciprocal lattice for the particular choice of **Fig. I.2** are:

$$H=\left(\frac{1}{2}\quad\frac{1}{2}\quad-\frac{1}{2}\right)\cdot\begin{pmatrix}\vec{b}_1\\ \vec{b}_2\\ \vec{b}_3\end{pmatrix}=\frac{2p}{a}(0\quad 0\quad 1);\qquad N=\left(\frac{1}{2}\quad 0\quad 0\right)\cdot\begin{pmatrix}\vec{b}_1\\ \vec{b}_2\\ \vec{b}_3\end{pmatrix}=\frac{2p}{a}\left(0\quad\frac{1}{2}\quad\frac{1}{2}\right);$$

$$P=\left(\frac{1}{4}\quad\frac{1}{4}\quad\frac{1}{4}\right)\cdot\begin{pmatrix}\vec{b}_1\\ \vec{b}_2\\ \vec{b}_3\end{pmatrix}=\frac{2p}{a}\left(\frac{1}{2}\quad\frac{1}{2}\quad\frac{1}{2}\right)$$

I.3 Face centered cubic lattice.

A symmetric set of primitive vectors for the fcc lattice is:

$$\bar{a}_1=\frac{a}{2}(0\quad 1\quad 1);\qquad \bar{a}_2=\frac{a}{2}(1\quad 0\quad 1);\qquad \bar{a}_3=\frac{a}{2}(1\quad 1\quad 0)$$

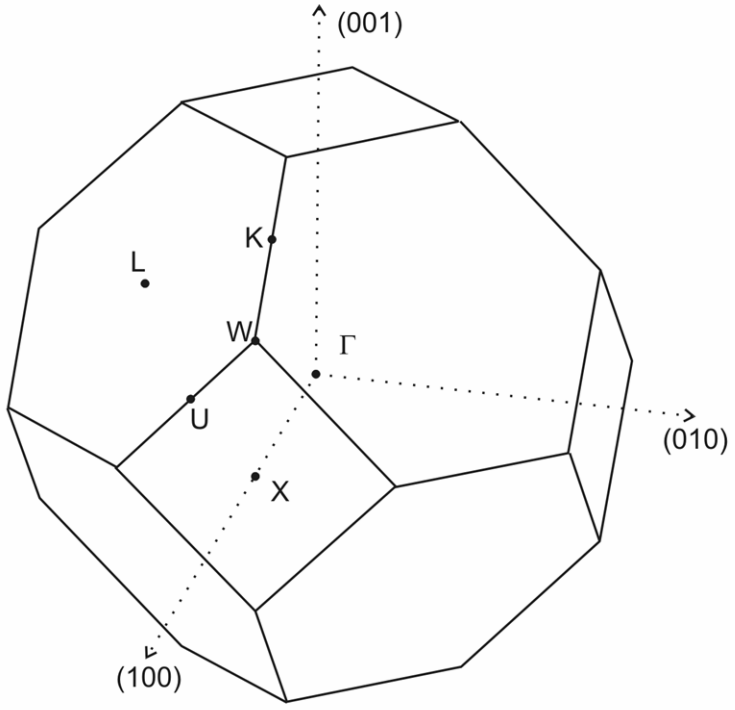

Fig. I.3: fcc Brillouin zone and most important symmetry points.

The reciprocal lattice vectors generate a bcc lattice with atom coordinates given by:

$$\vec{b}_1 = \frac{2p}{a}(-1 \quad 1 \quad 1); \qquad \vec{b}_2 = \frac{2p}{a}(1 \quad -1 \quad 1); \qquad \vec{b}_3 = \frac{2p}{a}(1 \quad 1 \quad -1)$$

The BZ for an fcc lattice is a truncated octahedron as shown in. **Fig. I.3**. High symmetry points are also represented and labeled as Γ (center of the BZ), X, L, U, K, and W.

The symmetry points coordinates in the reciprocal lattice for the particular choice of **Fig. I.3** are:

$$X = \begin{pmatrix} 0 & \frac{1}{2} & \frac{1}{2} \end{pmatrix} \cdot \begin{pmatrix} \vec{b}_1 \\ \vec{b}_2 \\ \vec{b}_3 \end{pmatrix} = \frac{2p}{a}(1 \quad 0 \quad 0); \qquad U = \begin{pmatrix} 0 & \frac{5}{8} & \frac{3}{8} \end{pmatrix} \cdot \begin{pmatrix} \vec{b}_1 \\ \vec{b}_2 \\ \vec{b}_3 \end{pmatrix} = \frac{2p}{a}\begin{pmatrix} 1 & -\frac{1}{4} & \frac{1}{4} \end{pmatrix}$$

$$L = \begin{pmatrix} 0 & \frac{1}{2} & 0 \end{pmatrix} \cdot \begin{pmatrix} \vec{b}_1 \\ \vec{b}_2 \\ \vec{b}_3 \end{pmatrix} = \frac{2p}{a}\begin{pmatrix} \frac{1}{2} & -\frac{1}{2} & \frac{1}{2} \end{pmatrix} \qquad W = \begin{pmatrix} \frac{1}{4} & \frac{3}{4} & \frac{1}{2} \end{pmatrix} \cdot \begin{pmatrix} \vec{b}_1 \\ \vec{b}_2 \\ \vec{b}_3 \end{pmatrix} = \frac{2p}{a}\begin{pmatrix} 1 & 0 & \frac{1}{2} \end{pmatrix}$$

$$K = \begin{pmatrix} \frac{3}{8} & \frac{3}{4} & \frac{3}{8} \end{pmatrix} \cdot \begin{pmatrix} \vec{b}_1 \\ \vec{b}_2 \\ \vec{b}_3 \end{pmatrix} = \frac{2p}{a}\begin{pmatrix} \frac{3}{4} & 0 & \frac{3}{4} \end{pmatrix}$$

Appendix II: Geometrical and analytical description of some important fcc planes.

In this appendix, computer generated images of different planes present in fcc lattices will be provided. For each direction a set of primitive vectors will be chosen so that the first layer lies on the X-Y plane. The first two vectors will generate the first layer and the third vector will give us information about how next layer is shifted along the Z axis.

In all cases the condition for touching spheres is $a=\sqrt{2}\cdot d$, where a is the lattice parameter and d is the sphere diameter.

II.1 {001} planes. Γ-X direction.

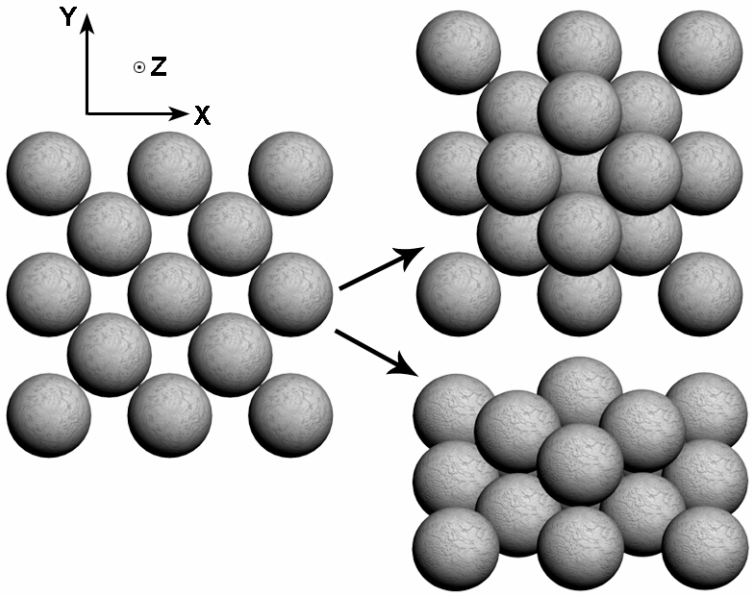

Fig. II.1: Top view of the first layer of a {001} plane in an fcc lattice (left). Two layers top (right-top) and perspective view (right bottom).

The vectors that will generate these planes are:

$$\vec{a}_1^{\{001\}} = a(1 \quad 0 \quad 0); \qquad \vec{a}_2^{\{001\}} = a\left(\frac{1}{2} \quad \frac{1}{2} \quad 0\right); \qquad \vec{a}_3^{\{001\}} = a\left(\frac{1}{2} \quad 0 \quad \frac{1}{2}\right)$$

From these vectors it can be deduced that interlayer distance is $a/2$. The structure is repeated every two layers in the (001) direction. This means that spheres in the 3rd layer are exactly above those of the 1st layer.

II.2 {111} planes. Γ-L direction.

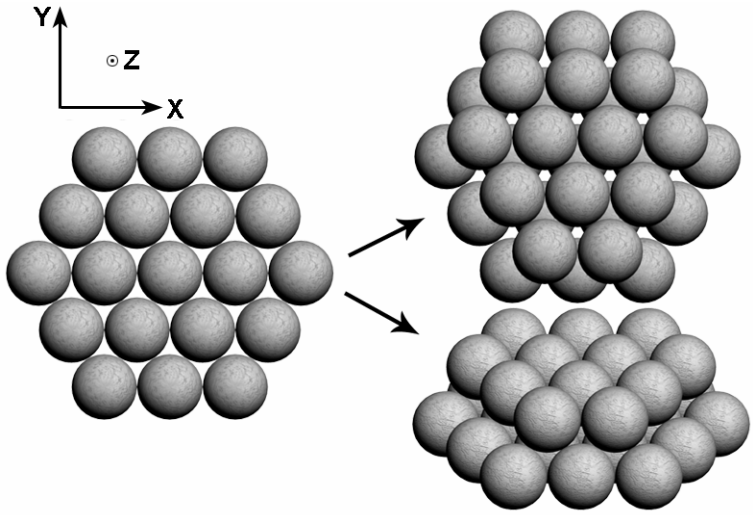

Fig. II.2: Top view of the first layer of a {111} plane in an fcc lattice (left). Two layers top (right-top) and perspective view (right bottom).

The vectors that will generate these planes are:

$$\vec{a}_1^{\{111\}} = a\left(\frac{1}{\sqrt{2}} \quad 0 \quad 0\right); \qquad \vec{a}_2^{\{111\}} = a\left(\frac{1}{2\sqrt{2}} \quad \frac{\sqrt{3}}{2\sqrt{2}} \quad 0\right)$$

$$\vec{a}_3^{\{111\}} = a\left(\frac{1}{2\sqrt{2}} \quad \frac{1}{2\sqrt{6}} \quad \frac{1}{\sqrt{3}}\right)$$

From these vectors it can be deduced that interlayer distance is $a/\sqrt{3}$. The structure is repeated every three layers in the (111) direction. This means that spheres in the 4th layer are exactly above those of the 1st layer.

II.3 {011} planes. Γ-K direction.

The vectors that will generate these planes are:

$$\vec{a}_1^{\{011\}} = a\left(\frac{1}{\sqrt{2}} \quad 0 \quad 0\right); \qquad \vec{a}_2^{\{011\}} = a(0 \quad 1 \quad 0); \qquad \vec{a}_3^{\{011\}} = a\left(\frac{1}{2\sqrt{2}} \quad \frac{1}{2} \quad \frac{1}{2\sqrt{2}}\right)$$

From these vectors it can be deduced that interlayer distance is $a/\sqrt{8}$. The structure is repeated every two layers in the (011) direction. This means that spheres in the 3rd layer are exactly above those of the 1st layer.

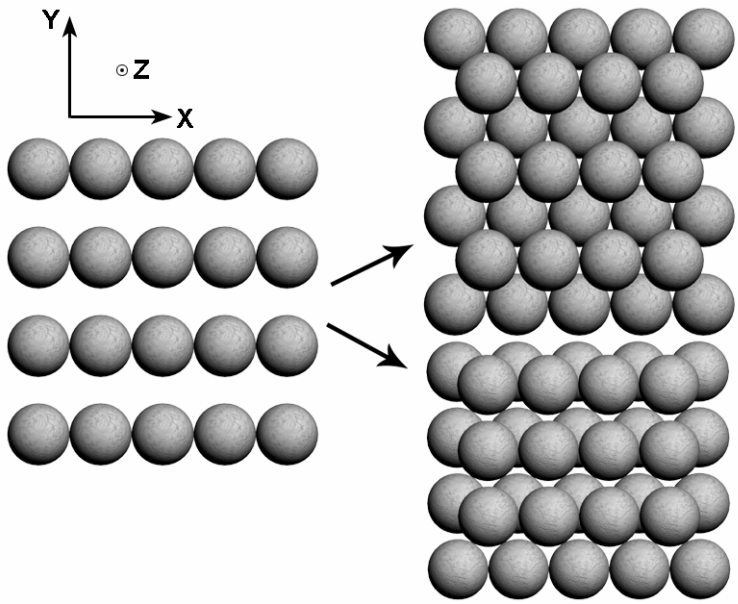

Fig. II.3: Top view of the first layer of a {011} plane in an fcc lattice (left). Two layers top (right-top) and perspective view (right bottom).

II.4 {201} planes. G-W direction.

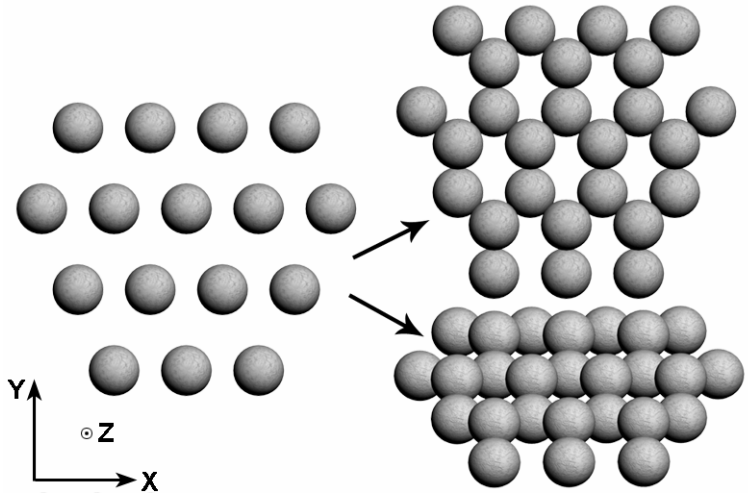

Fig. II.4: Top view of the first layer of a {201} plane in an fcc lattice (left). Two layers top (right-top) and perspective view (right bottom).

The vectors that will generate these planes are:

$$a_1^{\{201\}} = a(1 \quad 0 \quad 0); \qquad a_2^{\{201\}} = a\left(\frac{1}{2} \quad \frac{\sqrt{5}}{2} \quad 0\right); \quad a_3^{\{201\}} = a\left(\frac{1}{2} \quad \frac{-1}{\sqrt{5}} \quad \frac{1}{2\sqrt{5}}\right)$$

From these vectors it can be deduced that interlayer distance is $a/\sqrt{20}$. The structure is repeated every ten layers in the (201) direction. This means that spheres in the 11th layer are exactly above those of the 1st layer.

II.5 {411} planes. G-U direction.

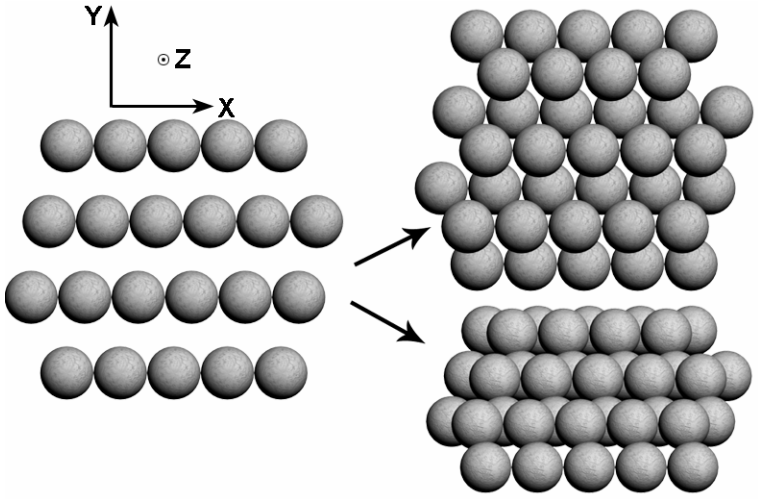

Fig. II.5: Top view of the first layer of a {411} plane in an fcc lattice (left). Two layers top (right-top) and perspective view (right bottom).

The vectors that will generate these planes are:

$$\vec{a}_1^{\{411\}} = a\left(\frac{1}{\sqrt{2}} \quad 0 \quad 0\right) \qquad \vec{a}_2^{\{411\}} = a\left(\frac{1}{3\sqrt{2}} \quad 1 \quad 0\right) \qquad \vec{a}_3^{\{411\}} = a\left(\frac{5}{6\sqrt{2}} \quad \frac{1}{2} \quad \frac{1}{2\sqrt{2}}\right)$$

From these vectors it can be deduced that interlayer distance is $a/\sqrt{8}$. The structure is repeated every six layers in the (411) direction. This means that spheres in the 7th layer are exactly above those of the 1st layer.

Appendix III: Fourier coefficients of the dielectric function for spherical atoms.

As explained in Chapter 1, thanks to its periodicity, the dielectric function $e(\mathbf{r})$ can be expanded as a discrete summation where wave vectors are positions of the reciprocal lattice ($\mathbf{G}$):

$$e(\boldsymbol{r}) = \sum_{\boldsymbol{G}} e(\boldsymbol{G}) e^{i\boldsymbol{G}\boldsymbol{r}} ;$$

$$e(\boldsymbol{G}) = \frac{1}{V_{WS-cell}} \int_{V_{WS-cell}} e(\boldsymbol{r}) e^{-i\boldsymbol{G}\boldsymbol{r}} d\boldsymbol{r} ;$$

The integral to obtain the Fourier coefficients is evaluated in the Wigner-Seitz (WS) cell in the real space. The dielectric function Fourier coefficients are complicated to calculate since these cells can take arbitrary forms depending on the kind of lattice. However, some cases allow obtaining an exact analytical result and photonic band calculations based on plane wave methods can be computed much faster. In this appendix some useful examples are presented.

III.1 One homogeneous spherical atom.

In the cases in which the WS cell contains just one spherical atom, the dielectric function can be expressed as follows:

$$e(\boldsymbol{r}) = \begin{Bmatrix} e_m \Leftrightarrow r > R \\ e_s \Leftrightarrow r < R \end{Bmatrix};$$

where R is the sphere radius and e_s and e_m are the sphere and surrounding medium dielectric constants respectively. If the sphere is completely contained within the integration volume, the following expression is also valid:

$$e(\boldsymbol{r}) = e_m + \begin{Bmatrix} 0 \Leftrightarrow r > R \\ e_s - e_m \Leftrightarrow r < R \end{Bmatrix};$$

If this equation is used to calculate the Fourier coefficients we have:

$$e(\boldsymbol{G}) = \frac{e_m}{V_{WS-cell}} \int_{V_{WS-cell}} e^{-i\boldsymbol{G}\boldsymbol{r}} d\boldsymbol{r} + \frac{e_s - e_m}{V_{WS-cell}} \int_{V_{sphere}} e^{-i\boldsymbol{G}\boldsymbol{r}} d\boldsymbol{r} ;$$

The first integral is evaluated in the WS cell, however the second integral can be constrained to the sphere volume since it is null in the rest of the space and the whole sphere is contained in the WS cell. The advantage is that integration is much easier now.

Regarding the first integral, it is known that:

$$\int_{V_{WS-cell}} e^{-i\boldsymbol{G}\boldsymbol{r}} d\boldsymbol{r} = \begin{Bmatrix} V_{WS-cell} \Leftrightarrow \boldsymbol{G} = \vec{0} \\ 0 \Leftrightarrow \boldsymbol{G} \neq \vec{0} \end{Bmatrix};$$

Therefore first integral only contributes to the dielectric function Fourier coefficient where **G**=0. In general this coefficient is nothing but the average dielectric constant of the crystal. This is a general result that does not depend on the kind of lattice or the shape or number of atoms within the WS cell.

$$e(\boldsymbol{G} = \vec{0}) = \frac{1}{V_{WS-cell}} \int_{V_{WS-cell}} e(\boldsymbol{r}) d\boldsymbol{r} = \langle e \rangle;$$

For the rest of coefficients where **G**≠0:

$$e(\boldsymbol{G} \neq \vec{0}) = \frac{(e_s - e_m)}{V_{WS-cell}} \int_{V_{sphere}} e^{-i\boldsymbol{G}\boldsymbol{r}} d\boldsymbol{r} \ ;$$

Solving the integral in spherical coordinates:

$$e(\boldsymbol{G} \neq \vec{0}) = \frac{(e_s - e_m)}{V_{WS-cell}} \int_0^R r^2 dr \int_0^p e^{-iGr\cos(q)} \sin(q) dq \int_0^{2p} dj \ ;$$

$$e(\boldsymbol{G} \neq \vec{0}) = \frac{2p(e_s - e_m)}{V_{WS-cell}} \int_0^R r^2 dr \int_0^p e^{-iGr\cos(q)} \sin(q) dq \ ;$$

$$e(\boldsymbol{G} \neq \vec{0}) = \frac{4p(e_s - e_m)}{GV_{WS-cell}} \int_0^R r \sin(Gr)\, dr \ ;$$

And finally we obtain:

$$e(\boldsymbol{G} \neq \vec{0}) = \frac{4p(e_s - e_m)}{G^3 V_{WS-cell}} [\sin(GR) - GR\cos(GR)];$$

Taking into account that:

$$V_{sphere} = \frac{4}{3} pR^3; \ \ f = \frac{V_{sphere}}{V_{WS-cell}} \ ;$$

where *f* is the filling fraction. The final expression for Fourier coefficients is:

$$e(\boldsymbol{G} \neq \vec{0}) = 3f(e_s - e_m) \frac{\sin(GR) - GR\cos(GR)}{(GR)^3} \ ;$$

It is important to notice that this expression is valid for all kind of lattices with one spherical atom per WS cell. The only condition is that spheres must not overlap between them.

III.2 More than one homogeneous spherical atom.

This is the case of Bravais lattices with a multiple vector basis. We still have that for **G**=0 the Fourier coefficient is equal to the average dielectric constant of the lattice. For other coefficients the integral must be performed for all the spheres present in the WS cell each made of a dielectric e_n. The atoms positions are given by $\mathbf{r}_n$. Coordinates transformation can be applied to simplify calculations:

$$\boldsymbol{r} = \boldsymbol{r'} + \boldsymbol{r}_n; \quad d\boldsymbol{r} = d(\boldsymbol{r'} + \boldsymbol{r}_n) = d\boldsymbol{r'};$$

where **r**' is a vector that gives coordinates relative to each of the atoms. Operating as done in the previous section, the following equation is obtained:

$$e(\boldsymbol{G} \neq \vec{0}) = \sum_n \frac{(e_n - e_m)}{V_{WS-cell}} e^{-i\boldsymbol{G}\boldsymbol{r}_n} \int_{V_{sphere}^{(n)}} e^{-i\boldsymbol{G}\boldsymbol{r'}} d\boldsymbol{r'};$$

In this case there is a summation to all the atoms in the WS cell, and each term is multiplied by $e^{-i\mathbf{G}\mathbf{r}_n}$. Although these equations are easy to solve, this introduces an imaginary term that can be difficult to handle and interpret. However, having inversion symmetry in the WS cell implies that for every $\mathbf{r}_n$ there is an identical atom at $-\mathbf{r}_n$. Therefore in the summation we will find $e^{-i\mathbf{G}\mathbf{r}_n} + e^{i\mathbf{G}\mathbf{r}_n} = 2\cos(\mathbf{G}\mathbf{r}_n)$. Consequently, for lattices presenting inversion symmetry the Fourier coefficients are:

$$e(\boldsymbol{G} \neq \vec{0}) = \sum_n 3 f_n (e_n - e_m) \frac{\sin(GR_n) - GR_n \cos(GR_n)}{(GR_n)^3} \cos(\boldsymbol{G}\boldsymbol{r}_n);$$

where f_n corresponds to the filling fraction of each of the basis atoms.

An example of a two-atom basis with inversion symmetry is the diamond lattice for which basis vectors can be chosen to be: $\mathbf{r}_1 = a/8(111)$ and $\mathbf{r}_2 = -a/8(111)$.

$$e(\boldsymbol{G} \neq \vec{0}) = 3 f (e_s - e_m) \frac{\sin(GR) - GR\cos(GR)}{(GR)^3} \cos(\boldsymbol{G}\boldsymbol{r}_0); \quad \boldsymbol{r}_0 = \frac{a}{8}(1 \quad 1 \quad 1);$$

Another example is the mixed bcc lattice with a four-atom basis and inversion symmetry. Using the vectors given in section 6.2.2.1 we obtain:

$$e(\boldsymbol{G} \neq \vec{0}) = \frac{3f}{2} \frac{\sin(GR) - GR\cos(GR)}{(GR)^3} [(e_{silica} - e_m)\cos(\boldsymbol{G}\boldsymbol{r}_1) + (e_{latex} - e_m)\cos(\boldsymbol{G}\boldsymbol{r}_2)];$$

$$\boldsymbol{r}_1 = \frac{a}{8}(1 \quad 1 \quad 1); \quad \boldsymbol{r}_2 = \frac{3a}{8}(1 \quad 1 \quad 1);$$

In both cases one can be observe that no imaginary terms exist when the lattice presents inversion symmetry. The expression of the previous section can be recovered if $\mathbf{r}_n$=0 and all atoms are made of the same dielectric.

III.3 Sphere with a dielectric core.

Another singular case is that of spheres made of a dielectric core (with e_1 and R_1) in a dielectric shell (with e_2 and R_2). The dielectric function is:

$$e(\boldsymbol{r}) = \left\{ \begin{array}{c} e_m \Leftrightarrow r > R_2 \\ e_2 \Leftrightarrow R_1 < r < R_2 \\ e_1 \Leftrightarrow r < R_1 \end{array} \right\} = e_m + \left\{ \begin{array}{c} 0 \Leftrightarrow r > R_2 \\ e_2 - e_m \Leftrightarrow R_1 < r < R_2 \\ e_1 - e_m \Leftrightarrow r < R_1 \end{array} \right\};$$

Again $e(\mathbf{G}=0)=\langle e \rangle$. Repeating calculations as shown for homogeneous spheres but taking into account the former expression for the dielectric function leads to the following equation:

$$e(\boldsymbol{G} \neq \vec{0}) = \frac{3f'}{(GR_2)^3}\{(e_1 - e_2)[\sin(GR_1) - GR_1\cos(GR_1)] + (e_2 - e_m)[\sin(GR_2) - GR_2\cos(GR_2)]\};$$

where:

$$f' = \frac{\frac{4}{3}pR_2^3}{V_{WS-cell}};$$

Unfortunately this equation is not useful for artificial opals where semiconductor shells have been grown such as those presented in Chapter 5. This is a consequence of the overlapping of the spherical shells between neighbors.

Appendix IV: Other methods to fabricate artificial opals.

Apart from the methods to grow artificial opals explained in Chapter 3, there has been an extensive research to improve their quality and develop novel techniques. In this appendix three of the most effective are briefly described. As an important difference to the previous methods, these techniques or their modifications have allowed the fabrication of fcc structures showing {100} planes large enough to provide good optical measurements.

IV.1 Epitaxial growth.

This method was introduced in 1997 by van Blaaderen *et al.*[1] to obtain colloidal crystals forming an fcc array grown in the (001) direction. Before his work, all known self-assembly methods resulted in crystals showing the {111} planes.

In the (111) growth direction, once first layer spheres are settled (layer A), the next layer spheres may occupy two different stable dispositions (B or C) relative to the first layer. An fcc crystal would follow an ABCABCABC… or ACBACBACB… sequence while for an hcp array it would be: ABABAB… or ACACAC… However, if the sample was grown in the (001) direction, second layer spheres would have a single stable possibility and no twinning directions. Therefore, the first layer will determine the positions of the spheres for the subsequent layers. This is called epitaxial growth.

As it has been explained in Chapter 3 spheres tend to crystallize in a close-packed disposition. To force the first layer to be a (001) plane, a template of holes was made with electron-beam lithography. The spheres were dispersed in an index-matching and high ionic strength medium where van der Waals and Coulomb forces could be neglected. The size of the spheres chosen was 1.05 μm so that Peclet number was ≈0.2, that is, too high to allow crystallization in close-packed arrangements. Since silica spheres used in that experiment had a fluorescent core, the position of the spheres could be observed in-situ by means of confocal microscopy.

This method presented, however, a drawback: the samples fabricated could not be dried to obtain a solid crystal. Four years later Braun *et al.*[2] developed a modification of the procedure using a new solvent system based on hydrazine hydrate that allowed its removal at the completion of the process.

The concept of epitaxial growth will have a capital importance in Chapter 6 to fabricate a diamond structure.

IV.2 Capillary growth.

Kim *et al.*[3] presented in 1996 a novel method to self-assemble colloidal microspheres in micro channels. They made use of a technique to fabricate polymeric microstructures of organic material.[4] Channels were formed by the conformal contact of the patterned elastomeric master and a substrate. The ends of the channels were cut to allow the colloidal suspension to enter and air to escape. When a suspension reservoir was placed at one of the ends, the fluid filled the channels network due to capillary forces. At the other end of the channels, evaporation happened causing the aggregation and therefore crystallization of spheres in a similar way to the vertical deposition method explained in Chapter 3.

In the following years, the method was improved by Yang and collaborators. They fabricated V-shaped grooves with 70.6º apex angles beneath the surface of silicon wafers by means of soft lithography and anisotropic etching.[5] The geometry of this channels forces the crystal to grow in the (001) direction. With this method opal chips of up to 10 layers were reported. In other paper they modified the Kim *et al.* work to obtain opal microchannels with very good optical quality made of silica spheres as large as 850 nm.[6]

IV.3 Micro-cell confinement.

This technique was presented by Park *et al.*[7] to obtain thin opals not much before the vertical deposition method was published.[8] Their experimental setup consisted in constructing a cell from two glass substrates and a square frame of photoresist tightened with binder clips. Microchannels that could retain the spheres were photo-lithographed on one of the sides of the frame. The colloidal suspension was then injected through a hole in the top glass substrate. Capillary forces and pressure due to a nitrogen flow causes the aggregation of the spheres at the side of the frame where the microchannels are present.

The method, although not as simple as that of vertical deposition, has proven to be valid to fabricate thin opals of silica spheres of up to 600-700 nm of diameter or even larger (1.26 μm) if ethylene-glycol is used.[9] The sample layer number can be controlled by simply varying the thickness of the cell. In a less sophisticated version of this method the photoresist is substituted by an easily available Mylar film spacer.[10]

As happened with the capillary growth method, this technique could also take advantage of epitaxial growth to obtain solid opals showing large {100} planes.[11] In this case a regular array of square pyramidal pits is etched on silicon wafers. The procedure is the same as for V-shaped grooves but in this case the photo-lithographed motive is a square that becomes a pyramidal pit after the etching process. This templated surface is used as the bottom substrate for micro-cell confinement. The distance between apexes of neighboring pyramids is an integer multiple of the sphere diameter. In each pyramid the crystal grows in the (001) direction so that the array of pyramids works as a template designating the

positions of the first layers spheres. Epitaxial growth does the rest to obtain thin film opals showing {100} planes.

1 van Blaaderen, A., Ruel, R. & Wiltzius, P. Template-directed colloidal crystallization. *Nature* **385**, 321 (1997).

2 Braun, P. V. *et al.* Epitaxial growth of high dielectric contrast three-dimensional photonic crystals. *Adv. Mater.* **13**, 721 (2001).

3 Kim, E., Xia, Y. N. & Whitesides, G. M. Two- and three-dimensional crystallization of polymeric microspheres by micromolding in capillaries. *Adv. Mater.* **8**, 245 (1996).

4 Kim, E., Xia, Y. N. & Whitesides, G. M. Polymer Microstructures Formed by Molding in Capillaries. *Nature* **376**, 581 (1995).

5 Yang, S. M. & Ozin, G. A. Opal chips: vectorial growth of colloidal crystal patterns inside silicon wafers. *Chem. Commun.*, 2507 (2000).

6 Yang, S. M., Míguez, H. & Ozin, G. A. Opal Circuits of Light – Planarized Microphotonic Cristal Chips. *Adv. Func. Mater.*, **12**, 425 (2002).

7 Park, S. H., Qin, D. & Xia, Y. Crystallization of mesoscale particles over large areas. *Adv. Mater.* **10**, 1028 (1998).

8 Jiang, P., Bertone, J. F., Hwang, K. S. & Colvin, V. L. Single-crystal colloidal multilayers of controlled thickness. *Chem. Mat.* **11**, 2132 (1999).

9 Ibisate M. Cristales fotónicos basados en ópalos. (PhD. thesis, Universidad Autónoma de Madrid, 2003).

10 Lu, Y., Yin, Y. D., Gates, B. & Xia, Y. N. Growth of large crystals of monodispersed spherical colloids in fluidic cells fabricated using non-photolithographic methods. *Langmuir* **17**, 6344 (2001).

11 Yin, Y. D. & Xia, Y. N. Growth of large colloidal crystals with their (100) planes orientated parallel to the surfaces of supporting substrates. *Adv. Mater.* **14**, 605 (2002).

CONCLUSIONES GENERALES

Capítulo 2:

- El valor apropiado del índice de refracción (IR) para esferas de sílice sintetizadas es 1.425±0.005.
- Tratamientos a una temperatura inferior a 600 ºC apenas afectan al IR de las esferas de sílice. Para temperaturas superiores el IR muestra importantes variaciones a tener en cuenta.
- El comportamiento del IR de las esferas de sílice frente a la temperatura de calcinación no parece ser dependiente del tamaño de la esfera o del hecho de haber sido recrecida.
- La porosidad del las esferas sintetizadas es cercano al 25%. Las moléculas de agua pueden acceder a ellos.
- Para temperaturas superiores a 750 ºC los poros colapsan y el diámetro de la esfera disminuye significativamente.

Capítulo 3:

- Las suspensiones de esferas de sílice en agua tienden a formar sedimentos cristalinos con concentraciones cercanas al 55%. Por el contrario, los sedimentos obtenidos con esferas duras tienen concentraciones significativamente superiores.
- La calidad cristalina del sedimento obtenido en suspensiones coloidales disminuye al aumentar el diámetro de las esferas de sílice.
- La sedimentación asistida por electroforesis ha demostrado ser una buena técnica para obtener sedimentos opalinos de esferas de sílice de 870 nm de diámetro. En estos experimentos la velocidad de sedimentación es reducida sin afectar los parámetros que afectan a los coeficientes de difusión.
- La velocidad de sedimentación puede ser también aumentada para acelerar la fabricación de ópalos hechos con esferas de sílice pequeñas (de 200 a 300 nm).
- Se ha presentado un método para obtener ópalos en lámina delgada con esferas de un diámetro cercano a los 660 nm.

Capítulo 4:

- La posición espectral y el ancho de los picos de difracción Bragg por los planos {111} en los ópalos dan información sobre el parámetro de red, el factor de llenado, la constante dieléctrica efectiva y la calidad cristalina.

- La ley de Bragg es una buena aproximación para un primer estudio del comportamiento de la primera pseudobrecha (de gap en inglés) en un ópalo alrededor de la dirección ΓL cuando los índices de refracción y sus contrastes no son demasiado altos.
- Tanto el promedio de constantes dieléctricas como la ecuación de Maxwell-Garnett dan un valor preciso para la constante dieléctrica efectiva cuando los materiales que forman el ópalo tienen un bajo IR (<2.0). Para mayores IRs la constante dieléctrica efectiva debe ser calculada por otros métodos como el de expansión en ondas planas (PWE en inglés).
- El número de capas en un ópalo crecido como lámina delgada puede ser calculado estudiando las oscilaciones de Fabry-Perot.
- Los ópalos crecidos como láminas delgadas permiten el estudio de fenómenos que no pueden ser observados en ópalos crecidos por otros métodos (evolución de las propiedades ópticas con el número de capas, el patrón de difracción, oscilaciones de Fabry-Perot…).
- Las propiedades ópticas de los ópalos hechos con esferas de sílice con un núcleo de oro quedan determinadas tanto por la difracción Bragg inherente a la estructura ordenada como por la absorción del plasmón superficial debida a los núcleos metálicos.
- La absorción de la banda del plasmón puede ser observada mediante medidas de transmisión mientras que las de reflexión sólo muestran los picos de difracción Bragg.
- La posición espectral de la banda del plasmón está corrida al rojo en el ópalo seco cuando se compara con la de esferas aisladas u ópalos infiltrados. La explicación parece estar relacionada con un acoplamiento con el esparcimiento incoherente de luz.

Capítulo 5:

- Se ha optimizado el proceso para crecer cantidades muy precisas de silicio y germanio con muy baja contaminación por medio de deposición química en fase vapor.
- Las muestras fueron se sometieron a caracterización óptica y los resultados obtenidos muestran acuerdo con los cálculos teóricos de las estructuras de bandas.
- Sistemas multicapa de ambos semiconductores (Si y Ge) han sido desarrollados. Las muestras se han observado con un microscopio electrónico de barrido y caracterizado su óptica.
- La eliminación selectiva de germanio con agua regia se ha demostrado como técnica efectiva para crear cámaras de aire entre dos materiales.

- Cálculos teóricos muestran que ligeras variaciones en la topografía del cristal pueden dar lugar a importantes efectos (bandas planas, apertura de pseudobrechas…).
- Se ha mostrado una estructura de bandas con una brecha completa entre la 5ª y la 6ª banda y el método para fabricar el susodicho cristal.

Capítulo 6:

- Se ha mostrado un método para construir ópalos con simetría tipo diamante por medio de micro-manipulación robótica. La posición espectral de la brecha completa y su anchura puede ser controlada variando el tamaño de las esferas y su factor de llenado.
- Plantillas de agujeros que satisfacen todos los requerimientos para fijar firmemente las esferas de la primera capa han sido diseñadas y fabricadas.
- El ataque por plasma de oxígeno se ha mostrado como una técnica óptima para eliminar las esferas de látex sin dañar al resto de la estructura.
- Estructuras tipo diamante con una periodicidad del orden de la micra se han fabricado en las direcciones (001) y (111).
- Una técnica que no precisa de un soporte de esferas de látex se ha desarrollado para crecer estructuras tipo diamante en la dirección (001).
- Los resultados muestran la viabilidad de este método para preparar estructuras macroporosas. También abren el camino para la construcción de forma controlada de nuevas estructuras de interés fotónico y su estudio.

PUBLICATIONS

Papers in international journals.

- García-Santamaría, F., Ibisate, M., Rodríguez, I., Meseguer, F. & López, C. "Photonic Band Engineering in Opals by growth of Si/Ge multilayer shells.", *Adv. Mater.* **15**, 788 (2003).

- García-Santamaría, F., Miyazaki, H. T., Urquía, A., Ibisate, M., Belmonte, M., Shinya, N., Meseguer, F. & López, C. "Nanorobotic manipulation of microspheres for on-chip diamond architectures." *Adv. Mater.* **14**, 1144 (2002).

- Rodríguez-Gonzalez, B., Salgueiriño-Maceira, V., García-Santamaría, F. & Liz-Marzán, L. M. "Fully accessible gold nanoparticles within ordered macroporous solids." *Nano Lett.* **2**, 471 (2002).

- García-Santamaría, F., Salgueiriño-Maceira, V., López, C. & Liz-Marzán, L. M. "Synthetic opals based on silica-coated gold nanoparticles." *Langmuir* **18**, 4519 (2002).

- García-Santamaría, F., Míguez, H., Ibisate, M., Meseguer, F. & López, C. "Refractive index properties of calcined silica submicrometer spheres." *Langmuir* **18**, 1942 (2002).

- Meseguer, F., Blanco, A., Míguez, H., García-Santamaría, F., Ibisate, M. & López, C. "Synthesis of inverse opals." *Colloid Surf. A-Physicochem. Eng. Asp.* **202**, 281 (2002).

- García-Santamaría, F., López, C., Meseguer, F., López-Tejeira, F., Sánchez-Dehesa, J. & Miyazaki, H. T. "Opal-like photonic crystal with diamond lattice." *Appl. Phys. Lett.* **79**, 2309 (2001).

- Míguez, H., Chomski, E., García-Santamaría, F., Ibisate, M., John, S., López, C., Meseguer, F., Mondia, J. P., Ozin, G. A., Toader, O. & van Driel, H. M. "Photonic bandgap engineering in germanium inverse opals by chemical vapor deposition." *Adv. Mater.* **13**, 1634 (2001).

- Holgado, M., García-Santamaría, F., Blanco, A., Ibisate, M., Cintas, A., Míguez, H., Serna, C. J., Molpeceres, C., Requena, J., Mifsud, A., Meseguer, F. & López, C. "Electrophoretic deposition to control artificial opal growth." *Langmuir* **15**, 4701 (1999).

Book chapter.

- Míguez, H., Blanco, A., García-Santamaría, F., Ibisate, M., López, C., Meseguer, F., López-Tejeira, F. & Sanchez-Dehesa, J. "Inverse Opals Fabrication." NATO Science Series C, Mathematical and Physical Sciences, KLUWER ACADEMIC PUBLISHERS, **563**, pp. 219-228 (2001).

Especial mentions.

- Cover of the year 2002 award in Advanced Materials.
- Cover picture in Advanced Materials 15 (10), 2003.
- Cover picture in Advanced Materials 14 (16), 2002.